



HAL
open science

Spin dynamics and topological effects in physics of indirect excitons and microcavity polaritons

Anton Nalitov

► **To cite this version:**

Anton Nalitov. Spin dynamics and topological effects in physics of indirect excitons and microcavity polaritons. Other [cond-mat.other]. Université Blaise Pascal - Clermont-Ferrand II, 2015. English. NNT : 2015CLF22569 . tel-01294992

HAL Id: tel-01294992

<https://theses.hal.science/tel-01294992>

Submitted on 30 Mar 2016

HAL is a multi-disciplinary open access archive for the deposit and dissemination of scientific research documents, whether they are published or not. The documents may come from teaching and research institutions in France or abroad, or from public or private research centers.

L'archive ouverte pluridisciplinaire **HAL**, est destinée au dépôt et à la diffusion de documents scientifiques de niveau recherche, publiés ou non, émanant des établissements d'enseignement et de recherche français ou étrangers, des laboratoires publics ou privés.

N. D'ORDRE : D.U. 2569

UNIVERSITÉ BLAISE PASCAL
U.F.R. Sciences et Technologies
ECOLE DOCTORALE DES SCIENCES FONDAMENTALES
N° 822

THÈSE DE DOCTORAT

Défendue par

Anton NALITOV

**Dynamique de Spin et Effets Topologiques
en Physique des Excitons Indirects
et des Polaritons**

**(Spin Dynamics and Topological Effects
in Physics of Indirect Excitons
and Microcavity Polaritons)**

Soutenue publiquement le 06/05/2015, devant la commission d'examen:

CARUSOTTO Iacopo	rapporteur
GLAZOV Mikhail	rapporteur
AMO Alberto	examineur
GIPPIUS Nikolay	examineur
KAVOKIN Alexey	examineur
MALPUECH Guillaume	responsable
SOLNYSHKOV Dmitry	responsable

Contents

1	General properties of indirect excitons and microcavity polaritons	8
1.1	Semiconductor heterostructures	8
1.1.1	Zinc-blende crystal band structure	9
1.1.2	Excitons	9
1.1.3	Quantum Wells	11
1.1.4	Distributed Bragg Reflectors	13
1.1.5	Planar Microcavities	14
1.2	Indirect excitons in coupled quantum wells	16
1.2.1	Coupled oscillators model	17
1.2.2	Spin-orbit coupling	18
1.2.3	Bose-Einstein Condensation	20
1.2.4	Gross-Pitaevskii equation	23
1.3	Microcavity polaritons	24
1.3.1	Rabi model	24
1.3.2	Optical Spin Hall effect	25
1.3.3	Optical Parametric Oscillator	26
1.3.4	Boltzmann kinetic equations	27
1.3.5	Dipolaritons	28
2	Spin dynamics and topological effects in physics of indirect excitons	31
2.1	Nonlinear optical spectroscopy of indirect excitons	32
2.1.1	Photoinduced reflectivity and Kerr rotation	33
2.1.2	Exciton spin-anisotropic exchange interactions	36
2.1.3	Phase-space filling	43
2.1.4	Homogeneous line broadening	44
2.2	Relaxational spin dynamics of indirect excitons	45
2.2.1	Exciton gas spin relaxation	45
2.2.2	Spin density matrix model	46
2.2.3	Pump-probe experiment model	47
2.3	Coherent spin dynamics of indirect excitons	53
2.3.1	Bispinor evolution equation	54
2.3.2	The minimum of the energy dispersion	55
2.3.3	Topologically nontrivial spin configurations	57
2.4	Conclusion	58

3	Spin dynamics of the polariton optical parametric oscillator	63
3.1	Optical parametric oscillator in one-dimensional trap potential	63
3.1.1	Semiclassical Boltzmann kinetic equations model	65
3.1.2	Polarization inversion	67
3.1.3	One-dimensional trap potential effect	68
3.1.4	Gross-Pitaevskii model	70
3.2	Dipolariton optical parametric oscillator	71
3.2.1	Dipolariton parametric scattering	73
3.2.2	Dipolariton scattering: Born approximation	74
3.2.3	Dipolariton scattering: Second order correction	77
3.2.4	Polarization inversion switching	80
3.3	Conclusion	82
4	Spin dynamics and topological effects in microcavity pillar structures	83
4.1	Effective spin-orbit interaction	83
4.1.1	Polariton molecules	84
4.1.2	Polariton benzene	86
4.1.3	Polariton graphene	90
4.1.4	Trigonal warping and band topological transition	93
4.1.5	Optical spin Hall effect in polariton graphene	95
4.2	Polariton topological insulator	99
4.2.1	Energy polariton bandgap in external magnetic field	100
4.2.2	Topological invariant analysis	101
4.2.3	Topologically protected edge states	102
4.2.4	Edge propagation simulation	104
4.3	Conclusion	106

Acknowledgements

The last three years for me felt like dipping into the ocean of new physics, exciting ideas and brilliant scientists. During this time I was guided through this ocean, and without people surrounding me this adventure would't be possible.

I am greatly indebted to my colleagues, who spent most of this time with me and were always near, ready to help. Despite having so different views on physics, they all shared their passion for it with me. Nikolay Gippius invested a lot of his time and effort to educate me not only with particular theoretical techniques, but with much broader concepts and philosophical approach to science. Dmitry Solnyshkov never stopped surprising me with his imagination and clear view on our area of physics at the same time. Many times his calm and persistent approach to any problem helped me to move on and succeed in the end. I also should thank him for noticing mistakes in my calculations there, where I was sure everything was right. Guillaume Malpuech not only led all our activity and pushed me forward all this time, but was always open and ready to share his experience with me. I also want to thank all the brilliant PhD students and postdocs, with whom I could work together and who were a live motivation for me. I really could not dream of a better scientific team to be a part of!

I would like to thank our colleagues from the experimental field, from the University of Montpellier 2, LPN, Marcoussis and the University of Madrid, especially Masha Vladimirova and Alberto Amo. As the ones who are actually facing physical reality in all its complexity, they were asking us the right questions and opened the roads to our new activities.

I also thank the theorists who shared their knowledge with us and with me personally, especially Alexey Kavokin and Mikhail Glazov. I was always welcome in the University of Southampton and Ioffe Institute in Saint-Petersburg any time of the year. We had many deep and fruitful discussions, it is impossible to overestimate their impact on our progress. I should thank Iacopo Carusotto as well, as his ideas on spin-orbit interaction for light differed from our initial guesses, and in the end led to our most recent success in understanding of polariton topological insulators.

Finally, I want to thank my family on which I could always count. I cannot imagine how much were my parents worried about my survival abroad. To them I am in debt for being at this point of my life, they made me proud of myself. But most of all I want to thank Jenya, my wife, for inspiring me every single day with the very fact of her existence.

Introduction

The world we live in is made of matter, but the way we learn about it is mostly related to the light. For evolutionary reasons most of the information we get from the outside comes with light, emitted, reflected or refracted. For centuries humanity was building conception of physics basing on observations with naked eye. Naturally the light became an object of research and its instrument at the same time. The discoveries of light quantization and the speed of light constancy lay at the origin of two modern physical paradigms, quantum theory and the theory of relativity.

Understanding the interaction between the light and matter is crucial in solid state physics. It is used for both optical creation and study of electronic subsystems excitations. Among others, Wannier excitons, composite bosonic quasi-particles consisting of a semiconductor electron and hole, present a special interest. The light-matter interaction gives rise to a strong coupling between the exciton and the photon, and a new state of light-matter. Fascinating experiments on Bose-Einstein condensation of the microcavity polaritons, quanta of the light-matter, brought this fully quantum effect, previously observed in cold atoms, closer to macroscopic scales and room temperatures. Recently it has been demonstrated that the excitons themselves may be condensed provided that the electron and the hole are separated in space by an electric field. In the latter case we speak about spatially indirect excitons.

Both types of quasiparticles provide a platform where all sorts of physical phenomena may be simulated and visualized directly due to light-matter interaction. Despite reduced dimensionality and other properties specific to indirect excitons and cavity polaritons, they provide a sandbox where complicated topological, relativistic and spin-related phenomena may be modeled for deeper understanding. The present thesis manuscript contains a description of several interrelated works and is devoted to demonstration of this statement. I tried to make it as self-sufficient as possible, starting with the very basics of semiconductor physics and deriving more complicated phenomena later on. General properties of both quasiparticle types, which are used as a base for further findings, are introduced in Chapter 1. Chapter 2 is focused on indirect exciton spin dynamics in various conditions. In particular, a novel nonlinear optical spectroscopy technique is proposed for its experimental study. Models for indirect exciton spin dynamics in coherent and non-coherent regimes are introduced. Emergence of skyrmions, nontrivial topological configurations, is predicted in a coherently expanding indirect exciton system. The rest of the manuscript concerns cavity polariton physics and is divided in two parts. Spin kinetics of the optical parametric oscillator (OPO), a nonlinear device working on polaritons, is discussed in Chapter 3. A novel idea of polarization inversion voltage control is predicted in an OPO working on dipolaritons, a hybrid between the cavity polariton and the indirect exciton.

Finally, Chapter 4 focuses on study of pillar microcavity superstructures. The effect of the spin-orbit interaction for polaritons, arising from longitudinal-transverse splitting, in this type of system is studied profoundly. Its interesting and promising implication, the \mathbb{Z} topological insulator behaviour of polariton graphene in an external magnetic field, is discussed in the final section.

Chapter 1

General properties of indirect excitons and microcavity polaritons

The present chapter gives an introduction to excitonic quasi-particles, indirect excitons (IXs) and microcavity polaritons (or *polaritons* for simplicity), and their general properties. These two particular types of crystal electron subsystem excitations, taking place in coupled quantum wells (CQWs) and microcavities respectively, have different and peculiar properties, which draw interest from both fundamental and device application points of view. One of the most fascinating effects that can be realized with both of these composite quasi-bosons, is the Bose-Einstein condensation (BEC), when a many-body system demonstrates quantum behaviour on macroscopic scales. Having different spin structures, they provide rich possibilities of studying quantum spin systems and spin-related phenomena.

This chapter is organized as follows. The technological base and physical realizations of semiconductor structures, which allow one to generate and observe IXs and polaritons, are described in Section 1. Sections 2 and 3 are devoted to IXs and polaritons respectively, giving their description and derivation of some of their properties.

1.1 Semiconductor heterostructures

Technological progress in the area of semiconductor devices during the second half of the 20th century allowed to create almost arbitrary potentials for electrons and holes in semiconductors. The first semiconductor devices based on *p-n* transition realized a simple case of potential barrier and were manufactured via junction of separate semiconductor crystals. Emergence of semiconductor crystal growth techniques allowed to combine materials with different properties, such as energy gap value and band structures in general, within one crystal-quality sample.

The most suitable materials for such *heterostructures* were found to be the zinc-blend symmetry crystals, such as GaAs-Al_xGa_{1-x}As, discussed in the Subsection 1.

High quality crystals allow to observe *excitonic* effects. The excitons are hydrogen-like bosonic quasiparticles consisting of a conduction band electron and a hole in the valence band [1]. Their most general properties are discussed in the Subsection 2.

Semiconductor heterostructures with transitions of the type I (where two interfacing

materials have energy gaps, one of which is inside the other) allow to create confinement potentials for electrons and holes simultaneously. In the most simple case of sandwich-like structures, electron, hole, and therefore exciton motion is confined in one dimension, while remaining free in the other two, so that exciton becomes quasi-two-dimensional. The effect of *quantum well* potentials on quasiparticle general properties is discussed in Subsection 3.

Superlattices of layers with different refraction indices have properties of wavelength-selective mirrors, or *distributed Bragg reflectors*, described in Subsection 4.

Finally, a *microcavity*, consisting of QWs positioned between two Bragg reflectors, and coupling confined photon mode with 2D exciton in QWs, is introduced in Subsection 5.

1.1.1 Zinc-blende crystal band structure

Although many of the effects described in the present thesis may be realized with different materials, we will concentrate below on structures based on zinc-blende symmetry semiconductors, schematically sketched in Fig 1.1(a). They have cubic T_d point group symmetry and an energy gap between conduction band c , formed by s -type electron orbitals, and valence band v , emerging from p -type orbitals [2]. In effective mass approximation the conduction band energy dispersion is parabolic close to the gap and is characterized by an effective mass m_c . Valence band close to the gap is described with Luttinger Hamiltonian [3]:

$$H = \frac{\hbar^2}{2m_0} \left[\left(\gamma_1 + \frac{5}{2}\gamma_2 \right) \Delta - 2\gamma_3 (\nabla \mathbf{J})^2 + 2(\gamma_3 - \gamma_2) \left(J_x^2 \frac{\partial^2}{\partial x^2} + J_y^2 \frac{\partial^2}{\partial y^2} + J_z^2 \frac{\partial^2}{\partial z^2} \right) \right], \quad (1.1)$$

where γ_i is the set of independent Luttinger parameters varying for different materials, and \mathbf{J} is the total electron angular momentum vector operator, $J = 3/2$.

Its diagonalization results in two parabolic branches of energy dispersion, corresponding to heavy and light holes, quasi-particles with spins $\pm 3/2$ and $\pm 1/2$ and different effective masses m_{hh} and m_{lh} respectively. Neglecting spin-orbit interaction, conduction and light hole valence bands are twice degenerate in spin.

The band structure close to the Fermi level is shown in Fig. 1.1(b)

The energy gap between conduction and valence bands is *direct* in reciprocal space, which means that energy dispersion extrema positions in the Brillouin zone coincide. This fact makes possible the radiative recombination of electron-hole pairs close to the energy dispersion extrema. In this process a conduction band electron fills an empty valence band state (a hole) and emits a photon. On the contrary, electron-hole pairs with energies close to minimum may be generated in this types of semiconductors with light. In this case photons absorbed in a crystal lift electrons from valence to conduction band.

1.1.2 Excitons

Exciton is a composite bosonic quasi-particle consisting of a conduction band electron and a valence band hole. It may be understood as an excitation quantum of semiconductor (or insulator) electron subsystem. Two models of the exciton, corresponding to its characteristic size, are known as Frenkel and Wannier-Mott excitons. The first model

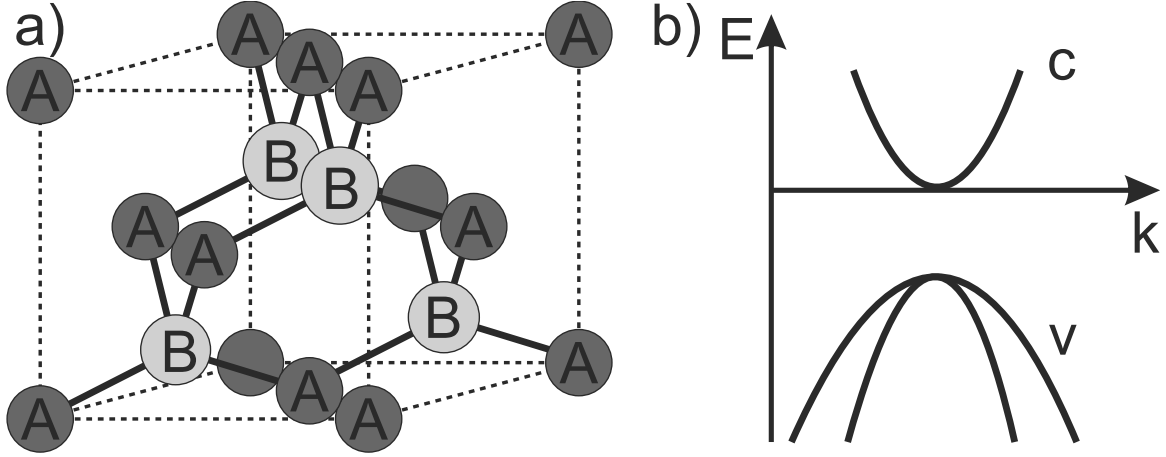


Figure 1.1: Left: Zincblende lattice schematic representation. Two cubic-symmetry sublattices A and B, formed by different types of atoms, are inserted into each other. Right panel: Zincblende bulk band structure, having a direct energy gap in the Γ of the Brillouin zone. Valence band energy dispersion is six times degenerate in the Γ point and splits into twice degenerate light hole, and four times degenerate heavy hole branches.

describes the situation where the average electron-hole distance is of the order of the lattice parameter, mostly relevant to molecule crystals [4]. The second one corresponds to the opposite limit, where the distance between the electron and the hole by far exceeds the size of a unit cell [1]. In this case they are treated as single quasi-particles in the effective mass approximation, and the Coulombic attraction between them is considered taking into account the effective dielectric permittivity of the crystal. The Hamiltonian is therefore analogous to that of the Hydrogen atom:

$$H = -\frac{\hbar}{2m_c} \nabla_e^2 - \frac{\hbar}{2m_v} \nabla_h^2 + \frac{e^2}{\varepsilon |\mathbf{r}_e + \mathbf{r}_h|}. \quad (1.2)$$

Here the first two terms of the right-hand part describe the kinetic energies of the conduction band electron with effective mass m_c and the hole with effective mass m_v respectively. The third term is the Coulombic interaction screened by the crystal effective permittivity ε . Note that the dielectric permittivity is only applicable on scales larger than the lattice parameter. Variables separation via transition to $\boldsymbol{\rho} = \mathbf{r}_e - \mathbf{r}_h$ and $\mathbf{R} = (m_e \mathbf{r}_e + m_h \mathbf{r}_h) / (m_e + m_h)$ results in the analytical hydrogen-like solution of the Shroedinger equation with the Hamiltonian (1.2):

$$\Psi_n^{\mathbf{Q},S}(\mathbf{r}_e, \mathbf{r}_h) = \Psi^{\mathbf{Q}}(\mathbf{R}) \Psi_{n,l,m}(\boldsymbol{\rho}) \chi^S(s_e, j_h). \quad (1.3)$$

Here, the translational motion of the exciton as whole is decoupled from the internal electron-hole motion and the spin part.

Size quantization of the excitons in confined systems, such as quantum wells or dots, removes the degeneracy between the heavy and light holes at the valence band extremum. That makes the heavy hole exciton the lowest energy state of an electron-hole pair. It is characterized by a unique spin structure consisting of four possible total momentum projections -2 , -1 , $+1$ and $+2$. It originates from electron spin projections $\pm 1/2$ and

heavy hole total momentum projections $\pm 3/2$. The *bright* states with total momentum projections ± 1 are optically active and may decay with photon emission. The emission frequency is defined by the exciton transition energy $E_X = E_g + E_e + E_h - E_B$, where E_g is the band gap energy, $E_{e(h)}$ is the electron(hole) size quantization energy and E_B is the exciton binding energy.

The ground excitonic state is analogous to a hydrogen atom with $1s$ -orbital electron. The wavefunction describing its internal electron-hole motion in the bulk semiconductor has the following form:

$$\Psi_{1,0,0}(\boldsymbol{\rho}) = A \exp\left(-\frac{\rho^2}{2a_B^2}\right), \quad (1.4)$$

where A is the normalization constant and $a_B = \varepsilon \hbar^2 (m_e + m_h) / m_e m_h e^2$ is the excitonic Bohr radius equal to the average electron-hole distance. The ground state binding energy $E_B = \hbar^2 (m_e + m_h) / 2m_e m_h a_B^2$ has the meaning of excitonic Rydberg constant setting the energy scale for excitons.

1.1.3 Quantum Wells

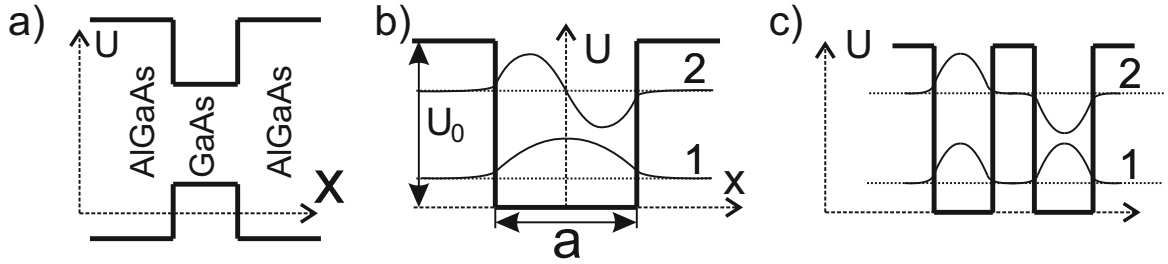


Figure 1.2: (a) GaAs- $\text{Al}_x\text{Ga}_{1-x}\text{As}$ quantum well energy diagram, showing the edges of valence and conduction bands through the growth direction. (b) and (c) Sketches for the one-dimensional potential QW and CQWs problems respectively.

The interface between two different semiconductors with energy gaps folded one into the other is called type-I heterointerface. Realistically, the most suitable candidates for physical realization of such an interface in a grown crystal were $\text{Al}_x\text{Ga}_{1-x}\text{As}/\text{GaAs}$ semiconductors of the type III-V, as seen from Fig. 1.3. Small difference in lattice parameters allows one to grow these heterostructures with atomic layer accuracy and low strain. At the same time, relatively large difference in energy gap values results in deep potential confinement.

Two parallel plane heterointerfaces of the type I placed close to each other form a confining potential in the direction normal to the interface planes - *quantum well* (QW) (Fig 1.2(a)). Both electron and hole motion in this direction is therefore finite and size quantized should the energy of the quasiparticles lie in the wider of the two gaps.

One-dimensional stationary Schroedinger equation with QW potential, sketched in Fig. 1.2(b), reads:

$$\left[-\frac{\hbar^2}{2m} \nabla^2 + U(x) \right] \Psi = E\Psi \quad (1.5)$$

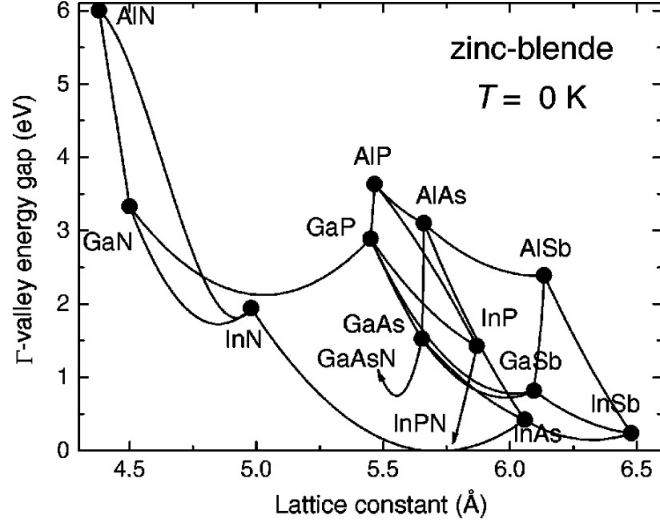


Figure 1.3: Energy gaps versus lattice constant measured for different zinc-blende symmetry materials at low temperatures. GaAs and AlAs have significant difference in gaps and low lattice parameter mismatch. From Vurgaftman, et al. (2001) [5]

$$U(x) = \begin{cases} 0, & |x| \leq a/2, \\ U_0, & |x| > a/2. \end{cases}$$

It yields transcendental equations for symmetric and antisymmetric state eigenenergies:

$$\sqrt{\frac{U_0 - E_s}{E_s}} = \tan\left(d\sqrt{\frac{mE_s}{2}}\right); \quad \sqrt{\frac{U_0 - E_a}{E_a}} = -\cot\left(d\sqrt{\frac{mE_a}{2}}\right), \quad (1.6)$$

where U and d are the QW depth and width and m is the quasiparticle mass. Here that the mass mismatch is neglected for the well and barrier materials.

The ground symmetric confined solution exists for any U and d , although its energy cannot be found analytically. All stationary solutions produce two-dimensional conduction and valence subbands due to electron and hole in-plane motion (Fig.1.2(b)).

Quasi-2D coupled electron-hole pairs in turn may form 2D excitons, described by the stationary Shroedinger equation of reduced dimensionality with the Hamiltonian of having the same form (1.2). The ground excitonic state wavefunction has the same form (1.3) with internal motion part (1.4), where \mathbf{R} and $\boldsymbol{\rho}$ have the meaning of in-plane center-of-mass position and electron-hole distance respectively, and Bohr radius is replaced by its 2D analogue $a_B^{2D} = a_B/2$. Consequently the binding energy of such an exciton is $E_B^{2D} = 4E_B$.

Two parallel QWs placed nearby form a *coupled quantum wells* (CQWs) pair (Fig. 1.2(c)). Single particle eigenstate problem in this case is also solved by joining wavefunction solutions in three regions. In absence of external electric field the eigenstates are symmetric and anti-symmetric due to the symmetry of the potential. The probability density is spread equally between the two QWs. However, once electric field projection on the QW growth axis is nonzero, band structure is distorted, single electron and hole wavefunctions are mostly confined in different QWs and are therefore separated spatially.

Exciton wavefunction calculation in this case is not trivial and is considered briefly in Section 2 of the present chapter.

1.1.4 Distributed Bragg Reflectors

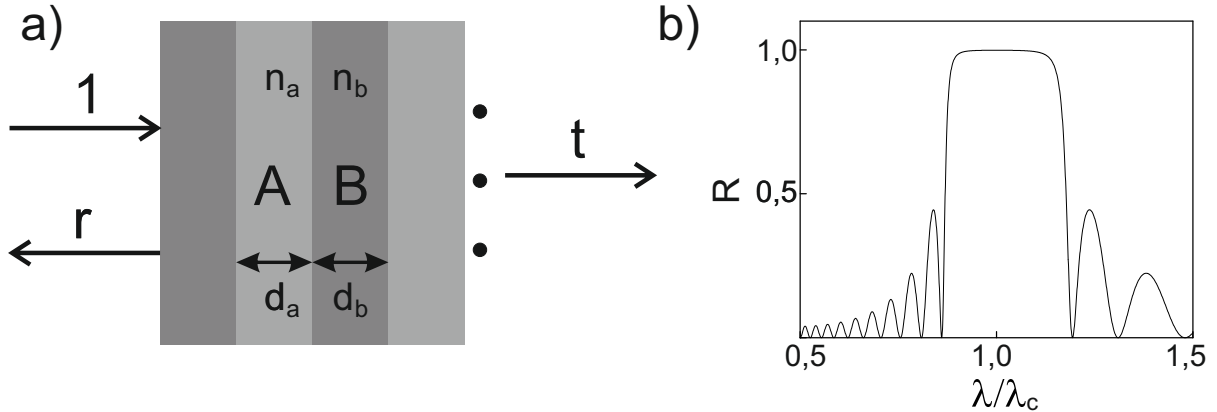


Figure 1.4: (a) A sketch of the DBR (b) A typical dependence of the intensity reflection coefficient on the wavelength for a DBR consisting of 10 periods of layers with refraction indices $n_a = 2$ and $n_b = 3$.

Distributed Bragg reflector (DBR) is a periodic structure composed of two types of dielectric layers A and B with different refraction indices n_a and n_b , and widths $d_a = \lambda_c/4n_a$ and $d_b = \lambda_c/4n_b$, alternating throughout one dimension. It is characterized by a reflectivity coefficient close to unity for normally incident light with wavelength in the vicinity of λ_c given $n_a a = n_b b = \lambda/4$. Such a good reflecting property of a dielectric structure is due to the positive interference of waves, reflected from all interfaces between layers. Structures of this type are fabricated layer by layer using standard semiconductor growth technologies.

DBRs may be modeled using the transfer matrix approach, considering a plane wave propagation through the structure growth direction z and reflection on the interfaces [6]. The electric field is represented as $E(x) = E_{\rightarrow}(x) \exp(ikn(x)x - i\omega t) + E_{\leftarrow}(x) \exp(-ikn(x)x - i\omega t)$, where ω and $k = \omega/c$ are the wave frequency and wave vector in the vacuum, and $E_{\rightarrow(\leftarrow)}$ has the meaning of the electric field envelope amplitude of the wave, propagating along (opposite to) growth direction x . Introducing a 2x1 vector $V(x) = [E_{\rightarrow}(x); E_{\leftarrow}(x)]^T$, the layers are described by 2x2 transfer matrices T_a and T_b , which relate the vectors V_t and V_b on the top and bottom sides of a corresponding layer, so that $V_b = T_{a(b)}V_t$. Due to linearity of this relation the transfer matrix of a complex structure is obtained as the product of all transfer matrices of composing it layers.

For an incident plane wave with the wave vector value $k = 2\pi/\lambda$ each individual homogeneous layer transfer matrix is defined by the phase $\varphi_{a(b)} = kn_{a(b)}da(b) = \pi/2$ that is gained during propagation and simply reads

$$T_{a(b)} = \begin{pmatrix} \exp(i\varphi_{a(b)}) & 0 \\ 0 & \exp(-i\varphi_{a(b)}) \end{pmatrix} = \begin{pmatrix} i & 0 \\ 0 & -i \end{pmatrix}. \quad (1.7)$$

The transfer matrix for the interface between the two media is given by

$$T_{ab} = \begin{pmatrix} 1 & \tilde{n} \\ \tilde{n} & 1 \end{pmatrix}, \quad \tilde{n} = \frac{n_a - n_b}{n_a + n_b} \quad (1.8)$$

therefore the transfer matrix of the structure period $T = T_a T_{ab} T_b T_{ba}$ reads:

$$T = - \begin{pmatrix} 1 + \tilde{n}^2 & -2\tilde{n} \\ -2\tilde{n} & 1 + \tilde{n}^2 \end{pmatrix}, \quad (1.9)$$

For a semi-infinite structure the reflectivity coefficient is obtained by equating the eigenvector of the period transfer matrix to the vector $[1, r]^T$ describing dimensionless electric field amplitudes of the incident and reflected waves. This gives the amplitude reflectivity coefficient $r = 1$ for the perfectly tuned wavelength $\lambda = \lambda_c$. For light frequency ω in the vicinity of $\omega_c = 2\pi c/\lambda_c$ it reads:

$$r = \exp[i\alpha(\omega - \omega_c)], \quad \alpha = \frac{L_{\text{DBR}}}{n_0 c}, \quad L_{\text{DBR}} = \frac{n_a n_b \lambda_c}{2(n_a - n_b)} \quad (1.10)$$

where n_0 is the refractive index of the medium outside of the DBR.

For finite DBRs one may simply calculate the whole structure transfer matrix T^N , where N is the number of AB periods in the structure and extract the complex amplitude reflectivity coefficient $r = -T_{21}/T_{22}$ and the intensity reflectivity $R = |r|^2$. A typical wavelength dependence of it is shown on Fig. 1.4(b).

1.1.5 Planar Microcavities

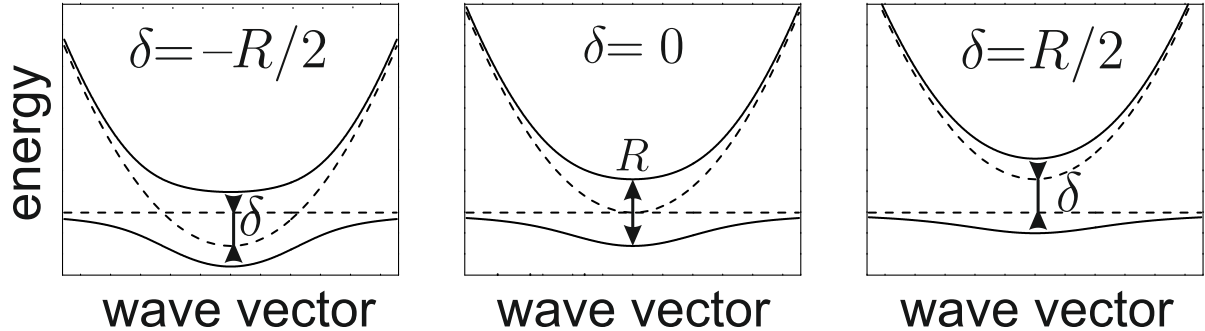


Figure 1.5: A sketch of planar microcavity eigenmodes dispersion for different detunings: negative (left), zero (center) and positive (right). Uncoupled exciton and cavity photon modes are plotted for comparison with dashed lines.

QWs and DBRs can be grown within one crystal-quality structure. Two DBRs separated by a layer, differing from the layers composing DBRs, form a Fabry-Pérot-type resonator for light in its stop band frequency region. A QW, or several QWs, placed in antidotes of the photonic mode, confined in the cavity between two DBRs, can realize strong coupling of excitonic and photonic modes, resulting in mixed *exciton-polariton* modes. Structures of this type are known as microcavities.

The realizations of the microcavity scheme may vary. DBRs may be replaced with metallic layers, which have good reflecting properties, but absorb light energy into heat, contrary to the dielectric DBRs. Planar geometry may be substituted with a spherical one, where one of the reflectors, or both, are curved. The photonic mode in this case is confined in three dimensions. It is also confined if a planar microcavity has a finite in-plane size, comparable to the light wavelength. Such structures with axial in-plane symmetry are known as pillar microcavities. Finally, QWs may be removed if the light coupling to the cavity bulk exciton is strong enough. However, the most common realization, which will be referred to by default, is a planar microcavity with DBRs and QWs.

Microcavity is characterized by its quality-factor Q - a measure of rate at which optical energy stored within the cavity dissipates. Two equivalent definitions of Q express it as the relation between the stored energy and energy loss during each oscillation cycle and as a relation between the photon mode frequency ω_c and its linewidth $\delta\omega_c$.

One important consequence of optical mode confinement is low-threshold lasing from microcavities. Size quantization reduces the density of optical states and therefore the number of optical modes coupled to an emitter. In some structures the threshold is absent as one photon emission is enough to start lasing.

As DBRs, microcavities may be modelled with transfer matrix method. In the simplest case microcavity consists of two homogeneous layers and one QW in the center between them, and the cavity transfer matrix is calculated as a product of three corresponding matrices. The reflectivity coefficient of DBRs r is obtained in the previous subsection and its absolute value is close to unity. Reflectivity and transmittivity coefficients from a QW close to an optically active exciton transition are given by [7]:

$$r_{\text{QW}} = \frac{i\Gamma_0}{\omega_0 - \omega - i(\Gamma + \Gamma_0)}, \quad t_{\text{QW}} = 1 - r_{\text{QW}}, \quad (1.11)$$

where ω_0 is renormalized exciton transition frequency, Γ_0 and Γ are the exciton radiational and nonradiational broadenings. The transfer matrix, corresponding to a layer with known reflectivity and transmittivity, is obtained solving matrix equations for light, incident from both sides of the QW:

$$T_{\text{QW}} = \frac{1}{t_{\text{QW}}} \begin{pmatrix} t_{\text{QW}}^2 - r_{\text{QW}}^2 & r_{\text{QW}} \\ -r_{\text{QW}} & 1 \end{pmatrix}. \quad (1.12)$$

Using expressions for homogeneous transfer matrices (1.7), one gets the cavity transfer matrix:

$$T_c = \begin{pmatrix} \exp(ikd/2) & 0 \\ 0 & \exp(-ikd/2) \end{pmatrix} T_{\text{QW}} \begin{pmatrix} \exp(ikd/2) & 0 \\ 0 & \exp(-ikd/2) \end{pmatrix}, \quad (1.13)$$

where d is the distance between the reflectors.

The eigenmodes are obtained as nontrivial solutions in absence of light outside the microcavity:

$$T_c \begin{pmatrix} r \\ 1 \end{pmatrix} = A \begin{pmatrix} 1 \\ r \end{pmatrix}, \quad (1.14)$$

from where the dispersion relation is derived:

$$(\omega_0 - \omega - i\Gamma)(\omega_c - \omega - i\Gamma_c) = R^2, \quad (1.15)$$

where Γ_c is inverted lifetime of a cavity photonic mode, squared Rabi splitting

$$R^2 = \frac{2\Gamma_0 c}{n_c(L_{\text{DBR}} + d)},$$

and n_c is the refractive index of the media inside the cavity.

In the general case of oblique incidence, photon cavity and QW exciton energies read:

$$\omega_c = \frac{\hbar k_{\parallel}^2}{2m_c}, \quad \omega_0 = \frac{\hbar k_{\parallel}^2}{2m_X} + \delta, \quad (1.16)$$

where m_c and m_X are the effective in-plane masses of cavity photon and exciton, k_{\parallel} is the in-plane wave vector related to the incidence angle φ as $k_{\parallel} = \omega/c \sin \varphi$ and δ is detuning between exciton transition and confined photon frequencies.

The strong coupling regime is realized when $R > \Gamma, \Gamma_c$. The energy dispersion law in this case is schematically represented in Fig. 1.5 for different values and signs of the detuning δ . Anti-crossing of photonic and excitonic branches gives rise to two mixed *polaritonic* branches.

Accounting for the difference in reflectivity coefficients from DBRs for TE and TM linearly polarized modes, which only takes place in the oblique incidence case, one obtains quadratic in k_{\parallel} splitting, known as TE-TM splitting. This effect is particularly interesting when studying the lower polaritonic branch.

1.2 Indirect excitons in coupled quantum wells

Electron and hole composing a Wannier-Mott exciton are in some cases separated in either direct or reciprocal space. The last case is met in semiconductors where conduction band energy minimum and valence band maximum are in different points of the Brillouin zone. The most common example of such a semiconductor is Silicon. Both single electron and hole in this case live in corresponding separated valleys of energy dispersion. If the Coulomb interaction energy is lower than the valley depths, it acts as a perturbation of the single particle dispersion, and electron-hole pair composing an exciton stays in the corresponding valleys.

The subject of the present thesis, however, is the spatially indirect exciton (IX), consisting of a 2D QW electron and heavy hole confined in a pair of adjacent CQWs. The electron and hole are separated by the potential barrier between the CQWs and an applied potential bias in direction, normal to the QWs plane. Electron and hole ground states in this case are confined in different QWs.

Spin structure of this type of excitons is similar to that of bulk Wannier-Mott excitons or QW confined heavy hole excitons. Total angular momentum projection on the CQWs growth axis, being the sum of electron spin $s_e = \pm 1/2$ and heavy hole angular momentum $j_h \pm 3/2$ projections, may have one of the four possible values ± 1 and ± 2 . *Bright* excitons with total spin projection $S = \pm 1$ are light-emitting, although photon emission is hindered by electron-hole separation. For the *dark* states with spin $S = \pm 2$ emission of a photon is forbidden by the selection rules.

Propagating exciton with nonzero spatial momentum is subject to effective fields, rotating electron and hole spins due to spin-orbit interaction, described in subsection 1.2.2.

Exciton lifetime is defined by the probability of electron-hole recombination, proportional to the overlap of electron and hole wavefunctions, or rather, in terms of the 2D internal motion wavefunction, to $|\Psi(\boldsymbol{\rho} = 0)|^2$. It is thus voltage controlled and may be increased up to several microseconds, being several orders of magnitude longer than that of conventional, or direct, excitons. Extremely long lifetime of the IXs is the main reason for considering them as potential information carriers for completely new type of electronics. Experimentally obtained characteristic transport lengths of IXs are of the order of hundreds of micrometers [8].

Another major property of IXs is strong interexciton repulsion due to the dipole moment, oriented normally to the CQWs plane [9]. Dipole-dipole repulsion force scales as $1/r^3$ with interexciton distance r and is linear in the dipole moment value, therefore in the separation distance between the CQWs d . The strong IX-IX repulsion [10] prevents excitonic gas from phase transition to electron-hole plasma at high densities. Combined with the long exciton lifetime τ , it allows one to generate IXs in extremely high densities $n = G\tau$, where G is the generation rate provided by either optical or electric excitation.

Exceeding the temperature-dependent critical exciton density results in excitonic condensation to a single quantum state. This effect is analogous to the atomic Bose-Einstein condensation. Subsection 1.2.3 is dedicated to this phenomenon, and subsection 1.2.4 introduces the spinor Gross-Pitaevskii equation describing the evolution of the condensates.

1.2.1 Coupled oscillators model

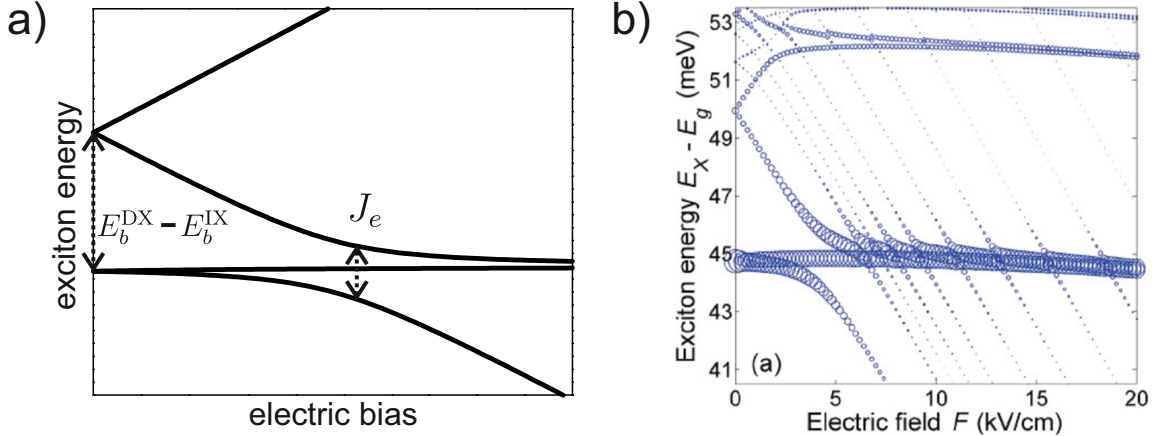


Figure 1.6: (a) A schematic representation of excitonic eigenstates in coupled quantum wells, obtained with diagonalization of the Hamiltonian (1.17). Spatially direct and indirect exciton states are coupled via electron tunneling through the barrier. (b) Results of the numerical calculation of excitonic eigenstates within the perturbation theory formalism. Excitonic state oscillator strengths are given with circle areas. From Sivalertporn et al. (2012) [11]

Coupled oscillators approximation may be used to obtain a simple model of CQWs under applied electric bias. Two types of exciton transitions are considered: direct exciton (DX), composed of an electron and a hole in one QW, and two indirect ones, coupled states

of an electron and a hole in different QWs. IX binding energy E_b^{IX} is lower than that of DX (E_b^{DX}) simply due to the spatial electron-hole separation. Exciton transition energy, however, may be calculated as the sum of the binding energy and noninteracting electron-hole pair energy. In the approximation of thin QWs, the latter reads $E_0 = E_g + E_e + E_h$ for DX transitions and $E_g + E_e + E_h \pm edE$ for IX transitions. Here e is the electron charge, d is the separation distance between the CQWs, E_g is the energy bandgap, E_e and E_h are electron and hole size quantization energies and E is the applied electric field. The coupling between the levels is mostly due to the electron tunneling between the CQWs, as the electron mass in the normal to the QW plane direction is smaller than that of a heavy hole. In the simplest model, the diagonal elements of the Hamiltonian matrix form are obtained taking into account the Coulomb electron-hole interaction and thus the binding energy, while nondiagonal ones are estimated treating excitons as noninteracting electron-hole pairs. The Hamiltonian then reads:

$$H = \begin{pmatrix} E_0 + E_b^{DX} & 0 & -J_e & 0 \\ 0 & E_0 + E_b^{DX} & 0 & -J_e \\ -J_e & 0 & E_0 + E_b^{DX} - edE & 0 \\ 0 & -J_e & 0 & E_0 + E_b^{DX} + edE \end{pmatrix}. \quad (1.17)$$

Diagonalization of the Hamiltonian (1.17) gives the superposed excitonic modes arising from the coupling between DXs and IXs. The anti-crossing between DX and IX modes is sketched in Fig. 1.6(a). In addition, one may deduce the oscillator strength of coupled modes from the direct exciton part c_{DX} of the linear superposition $c_{DX}|DX\rangle + c_{IX}|IX\rangle$:

$$f = f_{DX}|c_{DX}|^2 \quad (1.18)$$

However, in the range of applied voltages where $edE \gg J_e$, this coupling does not play any essential role, and IX and DX can be treated independently.

A more accurate model includes Coulombic electron-hole attraction as a perturbation over size-quantized single electron and hole states to numerically calculate the full exciton wavefunctions [11]. The latter allow to calculate the oscillator strengths, and therefore the radiative decay rates of the corresponding excitonic states, which are evanescently small for IXs, compared to that of DXs or mixed IX-DX states.

1.2.2 Spin-orbit coupling

Just as quasi-2D QW excitons, IXs are subject to the effect of spin-orbit coupling (SOC) acting on electron and hole simultaneously. It may be included into the effective Hamiltonian via the splittings of electron and hole propagating states with different spins, which are degenerate in the absence of SOC. Such splittings are possible due to broken symmetries of the system, which may originate from the microscopic structure of the relevant semiconductor material (bulk inversion asymmetry, or BIA), or from the given heterostructure properties, such as asymmetric QW or QW under an external electric field (structure inversion asymmetry, or SIA).

The first type of SOC terms, taking place in zinc-blende materials with BIA, were suggested by Dresselhaus [12] and have third order in wave-vector value k in bulk materials:

$$H_D = \beta [\sigma_x k_x (k_y^2 - k_z^2) + \sigma_y k_y (k_z^2 - k_x^2) + \sigma_z k_z (k_x^2 - k_y^2)]. \quad (1.19)$$

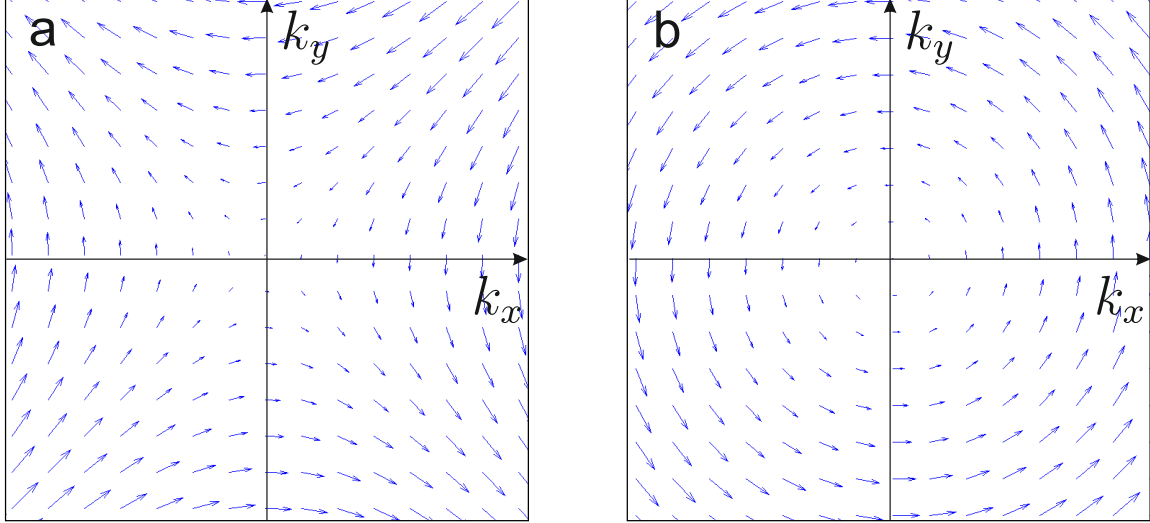


Figure 1.7: Effective spin-orbit interaction field texture map for Dresselhaus (a) and Rashba (b) terms.

Here cubic axes, parallel to $[100]$, $[010]$ and $[001]$ crystal directions, are used $\boldsymbol{\sigma}$ is the Pauli vector, resulting in 2x2 Hamiltonian term (1.19) acting on 2-component electron spinor in the basis of states $(+1/2, -1/2)$. To obtain the Dresselhaus term for quasi-2D conduction band electron in a QW one should average the bulk term (1.19) over momentum projection on normal to QW plane axis k_z , which is no longer a good quantum number for a QW-confined electron:

$$H_D^{\text{QW}} = \beta \langle k_z \rangle^2 [\sigma_y k_y - \sigma_x k_x]. \quad (1.20)$$

An term of the same form as (1.20) appears in QWs due to interface-induced asymmetry (IIA).

The terms of the second type, present in systems with SIA lacking the symmetry with respect to reflection off a plane, were introduced by Rashba [13] and are linear in electron momentum even in bulk materials:

$$H_R = \alpha [\boldsymbol{\sigma} \times \mathbf{k}] \cdot \mathbf{n}, \quad (1.21)$$

where \mathbf{n} is a dimensionless vector of absolute value 1 orthogonal to the lacking symmetry plane, and α is the Rashba constant depending on the structure. For asymmetric QWs or QWs under applied external electric field the direction of the vector \mathbf{n} is orthogonal to the QW plane, therefore the term (1.21) takes the form:

$$H_R^{\text{QW}} = \alpha [\sigma_x k_y - \sigma_y k_x] \quad (1.22)$$

The analogous SOC terms for QW-confined 2D heavy holes were considered to have the third order in the wave-vector, according to ref. [14], and in the spin basis $(3/2, -3/2)$ read:

$$\begin{aligned} H_D^{hh} &= \beta (\sigma_+ k_- k_+ k_- + \sigma_- k_+ k_- k_+), \\ H_R^{hh} &= i\alpha (\sigma_+ k_-^3 + \sigma_- k_+^3). \end{aligned} \quad (1.23)$$

Exciton-bound holes, however, differ from the free ones, being a superposition of plane wave states with wave vectors $k < a_B^{-1}$, where a_B is the exciton characteristic in-plane radius, or the average electron-hole distance. To obtain the SOC terms for exciton-bound electron and hole, one should average corresponding terms for single electrons and holes (1.22,1.20,1.23) over the exciton internal motion wavefunction in the momentum representation $\Psi_{\text{rel}}(q)$, where q is the relative electron-hole momentum defined from the relation between the electron, hole and exciton wavevectors:

$$k^e = \frac{m_e}{m_e + m_h} k^X + q/2, \quad k^h = \frac{m_h}{m_e + m_h} k^X - q/2.$$

The averaging of these terms

$$\tilde{H}_{D(R)}^{e(h)}(k^X) = \int |\Psi_{\text{rel}}(q)|^2 H_{D(R)}(m_{e(h)} k^X / (m_e + m_h) \pm q/2) dq \quad (1.24)$$

renormalizes both Rashba and Dresselhaus SOC constants for electron and Rashba constant for heavy holes, and also changes the form of the Dresselhaus term for holes. This introduces a linear-in-momentum Dresselhaus term analogous to that of electrons (1.20):

$$\tilde{H}_D^{hh} = \tilde{\beta}_{hh} [\sigma_y k_y^X - \sigma_x k_x^X]. \quad (1.25)$$

However, analogous linear-in-k SOC terms of the same order may be as well obtained for single holes in QWs in $k \cdot p$ formalism from IIA and heavy-light-hole mixing [15, 16]. Moreover, the reference [14] is now considered erroneous by the community. I thank M. Glazov for this valuable comment. Luckily, the conclusions of Section 2.3, which is based on excitonic SOC Hamiltonian, does not depend on the exact microscopic origin of SOC terms for exciton-bound electron and hole as long as their absolute values are comparable.

Neglecting the cubic terms for small momenta and keeping the highest order linear SOC terms, we can finally construct the exciton SOC Hamiltonian in the basis of exciton spin states $|+2\rangle, |+1\rangle, |-1\rangle, |-2\rangle$:

$$H(k^X) = \begin{pmatrix} E_{+2}(k^X) & \nu_e(\beta_e k_+^X + \alpha_e k_-^X) & \nu_h(\beta_h k_-^X) & 0 \\ \nu_e(\beta_e k_-^X - \alpha_e k_+^X) & E_{+1}(k^X) & 0 & \nu_h(\beta_h k_-^X) \\ \nu_h(\beta_h k_+^X) & 0 & E_{-1}(k^X) & \nu_e(\beta_e k_+^X + \alpha_e k_-^X) \\ 0 & \nu_h(\beta_h k_+^X) & \nu_e(\beta_e k_-^X - \alpha_e k_+^X) & E_{-2}(k^X) \end{pmatrix}, \quad (1.26)$$

where $\nu_{e(h)} = m_{e(h)}/(m_e + m_h)$, and $E_s(k^X)$ is the exciton kinetic energy.

1.2.3 Bose-Einstein Condensation

Excitons confined in QW structures, both direct and indirect, are composite bosons from the statistical point of view. Although these quasi-particles have finite lifetime τ contrary to atoms, a macroscopic number of them still can be condensed to a single quantum state at some circumstances, in analogy with Bose-Einstein condensation. Given a constant generation rate of excitons G due to either electrical or optical pumping, their total number also remains constant: $n = G\tau$. In this sense, long-living IXs in CQWs under electric bias are preferential candidates for condensation, which occurs in dense bosonic systems at low temperatures.

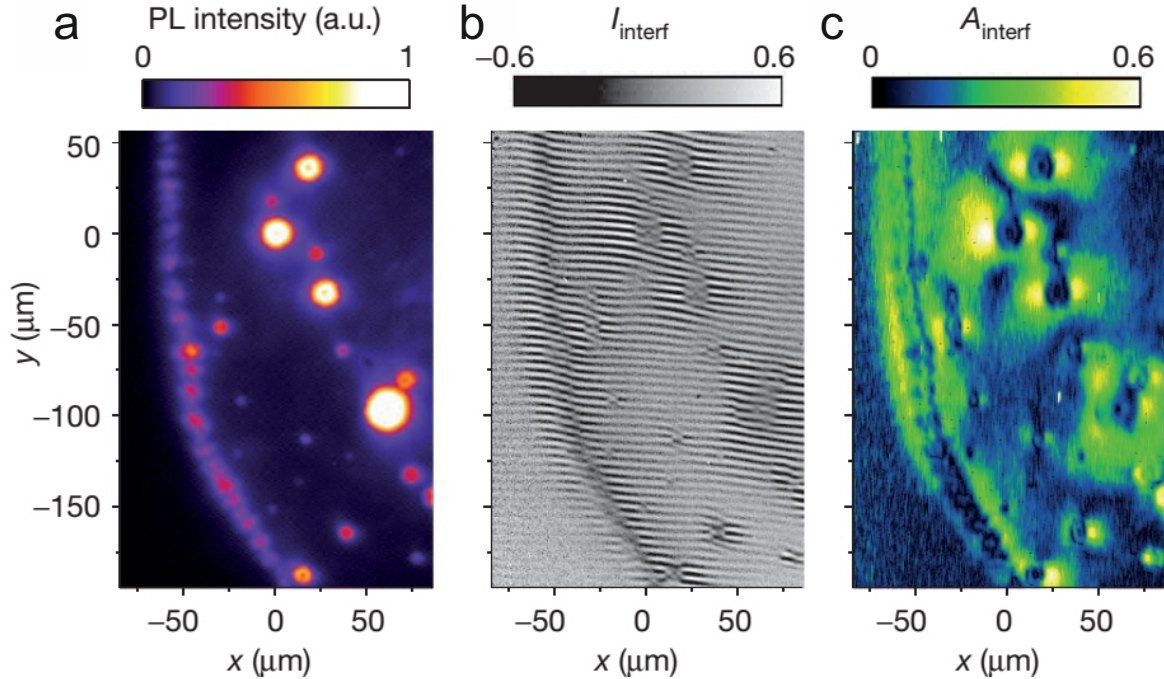


Figure 1.8: Formation of an indirect exciton condensate. (a) Photoluminescence intensity map, featuring bright regions on the ring and in localized bright spots, pinned to the sample. (b) Interference pattern obtained by superposing two spatially shifted images of the area. (c) Local map of first order coherence function. From High et al. (2012) [17]

In a simplified qualitative description, condensation of particles occurs when the thermal de Broglie wavelength is comparable with the interparticle distance. In 2D case this condition reads:

$$\lambda_{\text{dB}} = \left(\frac{2\pi\hbar^2}{mk_B T} \right)^{\frac{1}{2}} \approx n^{-\frac{1}{2}}, \quad (1.27)$$

from where at a given bosonic density n critical temperature may be estimated as

$$T_c \approx \frac{2\pi\hbar^2 n}{mk_B}. \quad (1.28)$$

Strictly speaking, BEC is not possible in neither 2D nor 1D infinite systems [18]. However, it occurs for trapped particles of any dimensionality due to size quantization. Assuming a constant number n of 2D quasi-particles, the average occupation number n_i of a state of a discrete spectrum with energy E_i obeys the Bose-Einstein statistics:

$$n_i = \frac{1}{\exp[\beta(E_i - \mu)] - 1}, \quad (1.29)$$

where $\beta = 1/k_B T$, T is the bosonic system temperature and μ is the chemical potential. The total number of quasi-particles is then expressed using (1.29) as a sum of all average occupation numbers:

$$n = \sum_{i=0}^{\infty} n_i. \quad (1.30)$$

At sufficiently high temperatures $\mu < E_0$ is defined by T . However, once the chemical potential reaches the ground state energy level at critical temperature T_c , the occupation becomes infinite, so that a macroscopic number of quasi-particles occupies the lowest possible energy state, which will be referred to as the condensate.

Condensation of this type also may occur in the absence of spatial confinement for quasi-particles with finite lifetime, provided the generation is inhomogeneous. This is the case for optical pumping of CQWs with a focused laser spot, when electrons and holes are generated under the excitation spot and diffuse outside. Due to the difference in diffusion coefficients, the maximum of the exciton generation term $G(\rho) \sim n_e(\rho)n_h(\rho)$, where ρ is the in-plane distance from the laser spot center, n_e and n_h are the electron and hole local densities, respectively, is situated on a ring outside the excitation spot [19, 11, 17]. Moreover, bosonic stimulation results in a fragmentation of the ring, producing numerous spots where IXs are generated from electrons and holes in adjacent CQWs [19].

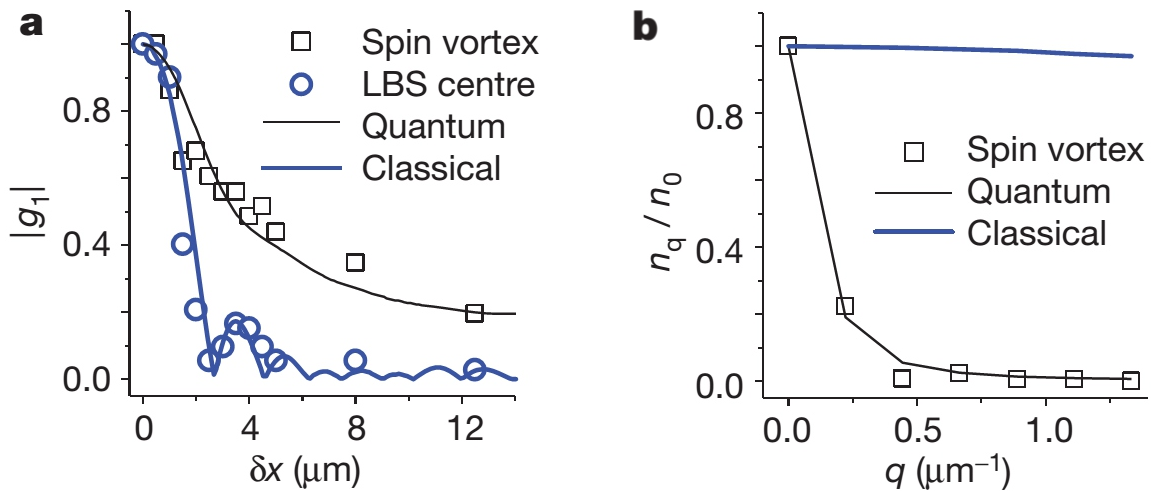


Figure 1.9: Experimental evidence for spontaneous coherence in an IX gas. (a) Two-point first order coherence function measured at the center of a bright spot (blue circles) and in the periphery (black squares). The deduced coherence decay length in the latter case is of the order of the bright spot size. (b) In-plane wave vector distribution of the IX emission corresponds to a strictly quantum statistics rather than classical. From High et al. (2012) [17]

Bosonic condensates are characterized by quantum properties which can be observed on a macroscopic scale. Experimentally measurable criteria of bosonic condensation include the emergence of off-diagonal long-range order [20], equivalent to Penrose-Onsager criterion in absence of confinement potential [21]. It manifests itself in spatial coherence of the excitonic light emission, measured via the interference of photons emitted from different points of the sample. First order coherence function is obtained from the intensities on the interference fringes:

$$g^{(1)} = \frac{I_{\max} - I_{\min}}{I_{\max} + I_{\min}}. \quad (1.31)$$

Coherence decay length equals de Broglie wave length in the case of a bosonic gas at tem-

peratures above the critical points and scales as $T^{-1/2}$. However, below the condensation temperature, when de Broglie wave length is comparable to the interparticle separation distance $n^{-1/2}$, the coherence length passes a threshold and increases up to the confinement size. For infinite systems of higher dimensions, this is followed by the appearance of a long-range order, satisfying the condition on nondiagonal elements of the density matrix in coordinate representation $\rho(\mathbf{r}_1, \mathbf{r}_2) = \langle \Psi^\dagger(\mathbf{r}_2)\Psi(\mathbf{r}_1) \rangle$:

$$\lim_{|\mathbf{r}_1 - \mathbf{r}_2| \rightarrow \infty} \rho(\mathbf{r}_1, \mathbf{r}_2) > 0. \quad (1.32)$$

Temperature-dependent interferometry measurements of the light emission from the bright spots on the external ring, as well as localized bright spots inside the ring, but outside the laser excitation spot, evidenced that the coherence length of the IX gas becomes longer than the de Broglie wavelength at low temperatures [22]. Measurements of the first order coherence function in the vicinity of a bright spot also suggests the a coherence decay length is of the order of a bright spot size [17], see Fig. 1.9. One should note that the optical interferometry measurements impose limitations on the coherence decay length accuracy below the diffraction limit. Observed coherence function is in reality convoluted with a function, decaying on the optical wavelength scale, which is of the order of a micrometer. However, coherent IX states established over whole bright spots are strongly evidencing in favour of IX condensation.

1.2.4 Gross-Pitaevskii equation

The condensates introduced in the previous subsection present a macroscopically populated quantum state and therefore have specific quantum properties. The behaviour of a condensate is described in mean-field approximation by quantum equation derived from Schroedinger equation for the state wavefunction with interparticle interaction taken into account:

$$i\hbar \frac{\partial}{\partial t} \Psi(\mathbf{r}, t) = \left[-\frac{\hbar^2 \nabla^2}{2m} + \int \Psi^\dagger(\mathbf{r}', t) V(\mathbf{r} - \mathbf{r}') \Psi(\mathbf{r}', t) d\mathbf{r}' + V^{\text{ext}}(\mathbf{r}, t) \right] \Psi(\mathbf{r}, t), \quad (1.33)$$

where m is the quasi-particle mass and $V(\rho)$ is the interaction potential between two bosons separated by a distance ρ and V^{ext} is the external potential imposed by the structure.

Assuming that the characteristic variation scale of the wavefunction exceeds that of the effective interaction potential, for spinless quasi-particles equation (1.33) transforms to Gross-Pitaevskii equation [23, 24]:

$$i\hbar \frac{\partial}{\partial t} \Psi(\mathbf{r}, t) = \left[-\frac{\hbar^2 \nabla^2}{2m} + \alpha |\Psi(\mathbf{r}, t)|^2 + V^{\text{ext}}(\mathbf{r}, t) \right] \Psi(\mathbf{r}, t), \quad (1.34)$$

where $\alpha = \int V(\rho) d\rho$ has a meaning of integrated interparticle interaction energy. Excitonic condensate state possesses the spin degree of freedom and therefore is described by a bispinor $[\Psi_{+2} \Psi_{+1} \Psi_{-1} \Psi_{-2}]^T$. The equation (1.34) is in this case transformed to a set of equations for each spin component, or the bispinor Gross-Pitaevskii equation:

$$i\hbar \frac{\partial}{\partial t} \Psi_i(\mathbf{r}, t) = \left[-\frac{\hbar^2 \nabla^2}{2m} + \alpha_{ijk} \Psi_j \Psi_k^* + V_i^{\text{ext}}(\mathbf{r}, t) \right] \Psi_i(\mathbf{r}, t). \quad (1.35)$$

Here i and j and k indices span over the spin components $+2, +1, -1, -2$. The interaction coefficient α in (1.34) is replaced by a matrix $\alpha_{i,j,k}$.

1.3 Microcavity polaritons

Microcavity energy dispersion derived in the Subsection 1.1.5 may be interpreted as an energy dispersion of *exciton-polaritons*, quasi-particles arising from the coupling between a photonic mode confined between two mirrors and an excitonic mode.

Lower energy dispersion branch is characterized by an extremely small mass, of the order of the confined photon effective mass m_c , derived from the photon energy dependence on the in-plane wave vector:

$$E_c(k_{\parallel}) = \hbar c \sqrt{k_0^2 + k_{\parallel}^2} \approx \hbar c k_0 + \frac{\hbar c k^2}{2k_0}, \quad (1.36)$$

where $k_0 = n\pi/L_c$, where n is the integer number of the photonic confined mode and L_c is the distance between the cavity reflectors.

In the simplified semiclassical picture, described in Subsection 1, the confined photon is periodically absorbed in the QWs as an exciton and reemitted back into the cavity.

Spin structure of microcavity polaritons differs from that of excitons. Indeed, the photonic mode is only coupled to bright excitons with spin ± 1 due to selection rules. The dark exciton states ± 2 are thus uncoupled from the cavity photonic mode and are split off the polaritonic dispersion branches. Microcavity polaritons therefore may have two possible spin projections ± 1 on the direction normal to the cavity plane. As a two-level system, polariton state may be defined by a *pseudospin* 3D vector of the unitary length on the Bloch sphere. The difference in longitudinally and transversely linearly polarized propagating polariton energies is interpreted as an effective in-plane momentum dependent magnetic field, around which the polariton pseudospin precesses. As a consequence, a linearly polarized excitation after its evolution in the presence of this effective field, is reemitted from different areas of the cavity with clockwise and anti-clockwise circular polarizations. This effect is known as the optical spin Hall effect and is described in Subsection 2.

Noncoherent dynamics of a polariton gas above the critical temperature is described by the Boltzmann kinetic equations formalism, introduced in Subsection 3.

The bosonic stimulation of polariton-polariton scattering due to the Coulomb dipole-dipole interaction between the excitonic parts of polaritons is used for nonlinear frequency conversion of light. A device working on this principle, the *optical parametric oscillator*, is described in Subsection 4.

Finally, the *dipolaritons*, quasi-particles emerging in microcavities with CQWs from the coupling between direct and indirect exciton modes, and a photonic confined mode, are introduced in Subsection 5.

1.3.1 Rabi model

Exciton-polariton in a microcavity may be studied in a semiclassical approach as a two-level electronic system driven by an oscillating electromagnetic wave. The state of the

electronic system is expressed as a superposition of the ground state $|g\rangle$ and the excited state $|e\rangle$:

$$|\Psi(t)\rangle = c_g(t)|g\rangle + c_e(t)|e\rangle. \quad (1.37)$$

The Hamiltonian of the system, accounting for interaction with alternating electric field $E(t)$ reads:

$$H = E_g|g\rangle\langle g| + E_e|e\rangle\langle e| - E(t) [P_{ge}|g\rangle\langle e| + P_{ge}^*|e\rangle\langle g|], \quad (1.38)$$

and is rewritten for an electromagnetic wave $E(t) = E_0 \cos(\omega_0 t)$ as a pair of coupled equations for complex coefficients c_g and c_e :

$$\begin{aligned} i \frac{\partial c_e}{\partial t} &= \omega_e c_e - \Omega_R \cos(\omega_0 t) c_g, \\ i \frac{\partial c_g}{\partial t} &= \omega_g c_g - \Omega_R^* \cos(\omega_0 t) c_e, \end{aligned} \quad (1.39)$$

where $\omega_{e(g)} = E_{e(g)}/\hbar$ and the Rabi frequency is introduced as $\Omega_R = V_{eg}/\hbar$.

The solution of (1.39) yields the probability of finding the electronic system in the excited state:

$$|c_e|^2 = \frac{\Omega_R^2}{\sqrt{\Omega_R^2 + (\omega_0 - \omega_e + \omega_g)^2}} \sin^2 \left(\frac{\sqrt{\Omega_R^2 + (\omega_0 - \omega_e + \omega_g)^2}}{2} t \right). \quad (1.40)$$

which contains the sine term responsible for the Rabi oscillations.

In the described situation photonic field is kept constant, which corresponds to external constant-wave pumping of cavity mode. In absence of external driving force oscillations between exciton and photon occur at the same Rabi frequency Ω_R , as it defines the coupling between excitonic and photonic oscillating modes.

The full quantum description of polaritons implies quantization of the electric field via introducing photon and exciton creation operators a^\dagger and b^\dagger and constructing the fully quantum Hamiltonian:

$$\hbar\omega_c a^\dagger a + \hbar(\omega_e - \omega_g) b^\dagger b + \hbar\Omega_R (ab^\dagger + a^\dagger b), \quad (1.41)$$

where ω_c is the cavity photon frequency, which is expressed for in-plane propagating states from (1.36). Diagonalization of the Hamiltonian (1.41) gives two branches energy dispersion law of in-plane propagating eigenstates, quantum superpositions of photons and excitons.

1.3.2 Optical Spin Hall effect

The energy splitting of TE and TM photonic modes confined in microcavities lifts the double degeneracy of polaritonic branches, related to polarisation degree of freedom. The TE-TM energy splitting of polaritonic energy dispersion is quadratic in in-plane momentum with a coefficient dependent on MC parameters. As for any two-level system, it acts as an effective magnetic field $\mathbf{\Omega}_{\text{TE-TM}}$, around which polariton pseudospin rotates, obeying the precession equation:

$$\frac{\partial \mathbf{S}}{\partial t} = -\mathbf{S} \times \mathbf{\Omega}_{\text{TE-TM}}. \quad (1.42)$$

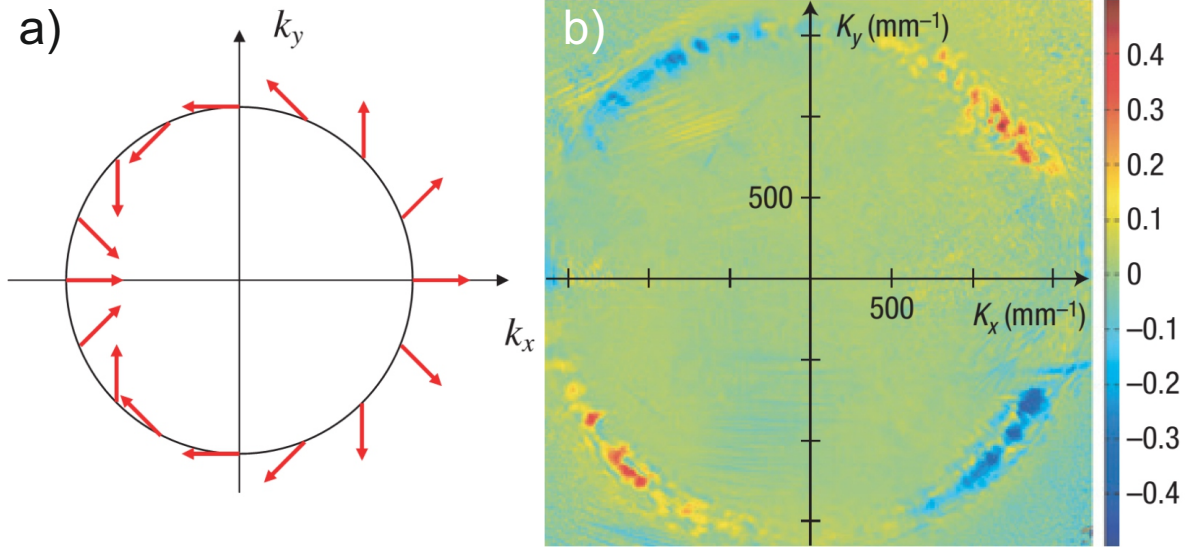


Figure 1.10: Optical spin Hall effect (OSHE). (a) TE-TM effective field map in reciprocal space. From Kavokin et al. (2005) [25]. (b) Experimental demonstration of OSHE. Circular polarization of light emission from a microcavity is mapped with colour in reciprocal space. Red and blue correspond to right and left circular polarizations. From Leyder et al. (2007) [26]

The effective momentum-dependent Hamiltonian term due to TE-TM splitting, acting on the spinor $[\Psi^+, \Psi^-]^T$, composed of polariton wavefunctions in two spin components +1 and -1, reads:

$$H_{\text{TE-TM}} = C_{\text{TE-TM}} k^2 \begin{pmatrix} 0 & e^{-2i\phi_k} \\ e^{-2i\phi_k} & 0 \end{pmatrix} \quad (1.43)$$

where ϕ_k is the angle between \mathbf{k} vector and x-axis. Both $H_{\text{TE-TM}}$ and $\mathbf{\Omega}_{\text{TE-TM}}$ satisfy the symmetry with respect to rotation by π ($\phi_k \rightarrow \phi_k + \pi$). The direction of the effective field $\mathbf{\Omega}_{\text{TE-TM}}$ makes two complete circumrotations while \mathbf{k} makes one, as seen from Fig. 1.9a, showing the field texture.

As consequence of pseudospin precession, light absorbed in microcavity is re-emitted through the reflectors with different polarization. This phenomenon is known as the Optical Spin Hall Effect (OSHE)[25]: an oblique angle incident focused linearly polarized light beam generates polariton gas or condensate propagating in all directions isotropically. The re-emitted light polarization texture in real space inherits the rotational symmetry of the TE-TM field as seen from Fig. 1.10b.

1.3.3 Optical Parametric Oscillator

Polaritons scatter on each other due to Coulomb interaction of their excitonic parts. Elastic scattering of excitons is only allowed by energy-momentum conservation law when they keep initial momentum absolute values. This is due to parabolicity of free exciton energy dispersion. Lower polariton branch, however, has an inflection point where the effective

mass changes sign, so the branch itself has a S-like shape. This implies that elastic scattering processes, where polaritons actually interchange kinetic energy, are allowed. Such processes are known as parametric polariton scattering. As an example, two polaritons on LPB may scatter so that one goes to the ground state with $k = 0$ and the other is lifted up in energy. This unique state is characterised by "magic" angle θ of optical pumping excitation. Resonant excitation of polaritons at this angle (see Fig 1.10) results in non-linear frequency-shifted reemission due to parametric polariton scattering. Experiment

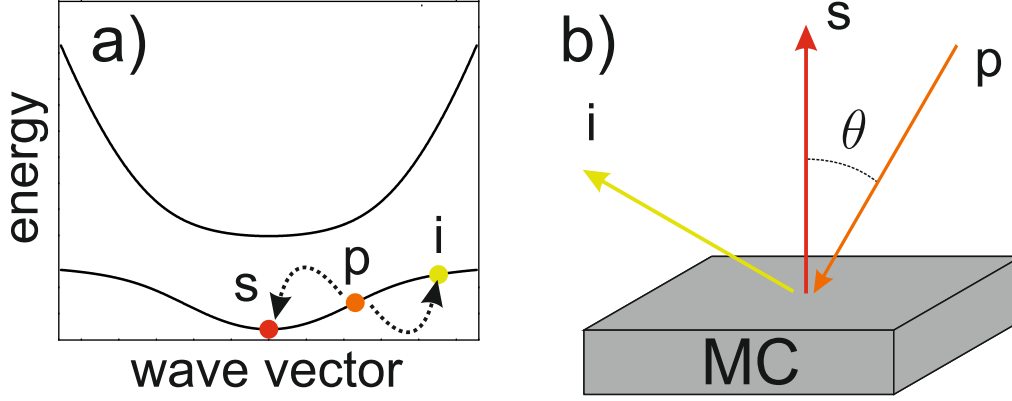


Figure 1.11: Polariton optical parametric oscillator. (a) Signal, pump and idler states participating in parametric scattering on the lower polariton branch of the energy dispersion. (b) Optical excitation scheme: pump states polaritons are resonantly injected with light beam incident at magic angle θ to the plane. Signal state polaritons emit light normally to the cavity plane.

on parametric stimulation [27], where parametric scattering was stimulated by a short normally incident pulse populating the ground polariton state, has demonstrated both existence of the effect and bosonic nature of polaritons. The nonlinear optical scheme, where polaritons are pumped at magic angle to the "pump" state (p) parametrically scatter into "signal" and "idler" states (s and i) and re-emit from these states, is known as polariton optical parametric oscillator.

1.3.4 Boltzmann kinetic equations

Classical Boltzmann equations, describing dynamics of occupation numbers of a space of states spanned by a generalized index k , read:

$$\frac{dn_k}{dt} = P_k - \Gamma_k n_k + \sum_{k'} W_{k' \rightarrow k} n_{k'} - \sum_{k'} W_{k \rightarrow k'} n_k. \quad (1.44)$$

Here P_k is the source term, $\Gamma_k = \tau_k^{-1}$ is the state specific decay rate, and $W_{i \rightarrow f}$ is the rate of transition $i \rightarrow f$.

The semiclassical Boltzmann equations account for the quantum statistical properties of the particles through modified rates of transitions. In case of bosons they are increased

linearly in the final state occupation:

$$\frac{dn_k}{dt} = P_k - \Gamma_k n_k + \sum_{k'} W_{k' \rightarrow k} n_{k'} (n_k + 1) - \sum_{k'} W_{k \rightarrow k'} n_k (n_{k'} + 1) \quad (1.45)$$

In the case of continuous spectra of states the system may be hard to solve analytically and usually is simulated numerically.

In the particular case of polaritonic OPO, however, one may only trace populations of the main states s , p , i and restrict the space of possible states. The system of semiclassical kinetic equations for this case reads:

$$\begin{aligned} \frac{dn_s}{dt} &= -\Gamma_s n_s + \frac{V}{2} n_p^2 (n_s + 1) (n_i + 1) - \frac{V}{2} n_s n_i (n_p + 1)^2, \\ \frac{dn_p}{dt} &= -\Gamma_p n_p + V n_s n_i (n_p + 1)^2 - V n_p^2 (n_s + 1) (n_i + 1), \\ \frac{dn_i}{dt} &= -\Gamma_i n_i + \frac{V}{2} n_p^2 (n_s + 1) (n_i + 1) - \frac{V}{2} n_s n_i (n_p + 1)^2. \end{aligned} \quad (1.46)$$

Here $\Gamma_{s,p,i}$ denote signal, pump and idler state decay rates respectively, and interaction constant V , governing the parametric scattering, is due to Coulombic scattering of excitonic parts of the polaritons.

The system of equations (1.46) is usually studied either at constant generation of p-state polaritons or with given initial conditions in case when optical pumping is pulsed. In both cases if the power of the pumping is sufficient to get several polaritons parametrically scattered, stimulated bosonic scattering occurs. As a result the dependence of signal emission power on that pumping has a threshold. Note that it does not account for polariton pseudospin. An analogous system with polarization degree of freedom taken into account will be introduced in Chapter 3.

One should note that being a powerful model for study of Bose-Einstein condensation, or macroscopic population of a single state, semiclassical Boltzmann equations miss fully quantum effects taking place in BECs. Namely, it does not predict dynamics of the order parameter of a BEC, which is described by the Gross-Pitaevskii equation. Consequently, it does not yield the physics of a condensate excitations, bogolons, solitons and quantized vortices.

1.3.5 Dipolaritons

Scattering of conventional polaritons is controlled by Coulomb exchange interaction between their excitonic parts. On the other hand, IXs are formed by an electron and a heavy hole in neighboring CQWs and thus have a dipole moment oriented along the growth direction (due to the applied bias) and proportional to the CQWs separation distance d . Consequently, the dipole-dipole repulsion of IXs is a first-order effect and is stronger than their exchange interaction, which switches from repulsive to attractive while increasing d [29, 30]. However, the coupling of an IX with a cavity photon mode is limited by the small oscillator strength of the IX, proportional to the overlap of the vanishing tails of the electron and hole wavefunctions in the barriers.

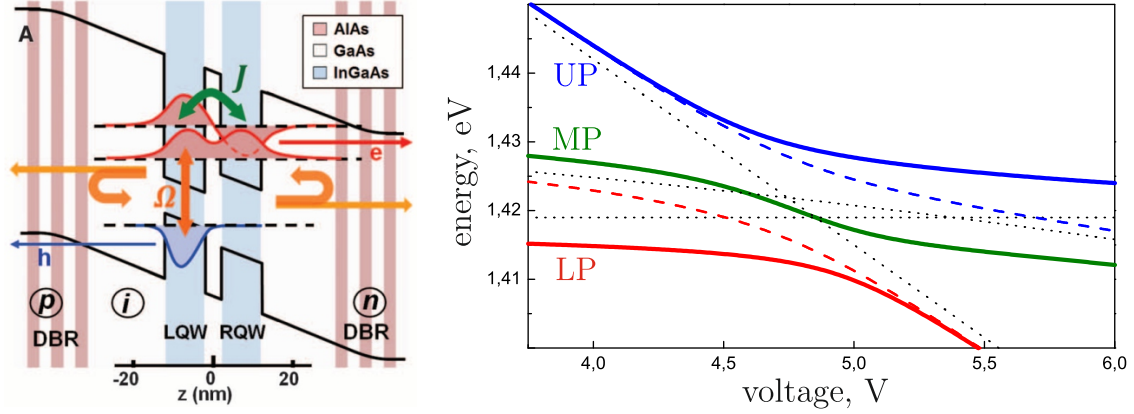


Figure 1.12: Dipolaritons in a microcavity with asymmetric double quantum wells. Left: Schematic sketch of the structure. From Cristofolini et al. (2012) [28] Right: calculation of the dipolariton branches. From Nalitov et al. (2014) [29]

Recently, exploiting the asymmetric double quantum wells (ASDQWs) for resonant tunnel coupling of IX to the conventional direct exciton (DX), their bound state was suggested and realized [28]. The ASDQW embedded in a microcavity structure is schematically shown in the left panel of Fig. 1.12. The coupling of three modes: indirect and direct exciton and cavity photon, gives rise to new two-dimensional quasi-particles *dipolaritons*. Being thus a mixture of dipolar matter and light, dipolaritons represent photons with strong dipolar interaction, at least one order of magnitude stronger than that between conventional polaritons.

The DX state is formed by an electron-hole pair in the ground state, confined in one QW, while the IX consists of a hole in the same QW as the one of the DX, and an electron in the other QW. The DX and IX are thus coupled via the electron tunneling through the barrier, described by the coupling constant J , while the DX coupling to the cavity mode is induced by the exciton oscillator strength, giving rise to the Rabi splitting Ω .

The ASDQWs are subject to an external electric field, normal to their plane, produced by a voltage V , applied to the contacts on the doped layers. The field shifts electron and hole levels of size quantization in both QWs, so that the DX energy $E_{\text{DX}}(V) = E_{\text{DX}}(0) - \beta V^2$ slowly decreases, depending quadratically on the field, due to the quantum confined Stark effect [31]. On the other hand, the IX energy $E_{\text{IX}}(V) = E_{\text{IX}}(0) - \gamma V$ shift is steeper and depends linearly on the field with the proportionality coefficient being the IX dipole moment [11].

In the absence of field, $E_{\text{IX}}(0) > E_{\text{DX}}(0)$. Therefore, at a certain voltage V_0 both exciton states have the same energy and become resonantly coupled. Let us consider the range of voltages around V_0 , where the IX energy shift is smaller than the energy distance to the nearest electron confinement level or the closest cavity photon mode. This allows one to neglect the presence of other states and to write the following system Hamiltonian [28]:

$$H(Q, V) = \begin{pmatrix} E_{\text{IX}}(V) & -J/2 & 0 \\ -J/2 & E_{\text{DX}}(V) & -\Omega/2 \\ 0 & -\Omega/2 & E_{\text{C}} + T_{\text{C}}(Q) \end{pmatrix}, \quad (1.47)$$

where $T_C(Q) = \hbar^2 Q^2 / 2m_C$ term accounts for the propagation of light in the cavity plane and represents the kinetic energy of the confined photon. Here \mathbf{Q} is the wave vector in the cavity plane and m_C stands for the effective mass of the cavity photon. Similar terms for excitons may be safely neglected due to the large exciton mass $m_I = m_D \sim 10^4 m_C$.

Diagonalization of the Hamiltonian (4.36) gives three dipolariton branches resulting from the strong coupling between the three initial resonances. They are shown as a function of voltage V in the right panel of Fig. 1.12. The following parameters were taken to qualitatively reproduce the results of Ref. [28]: $E_{IX}(0) = 1.55$ eV, $E_{DX}(0) = 1.43$ eV, $\gamma = 0.027|e|$, $\beta = 7.2 \cdot 10^{-16}$ eV $^{-1}$, $m_C = 10^{-4}m_e$, $\Omega = 6$ meV, $J = 6$ meV. Here e and m_e stand for electron charge and mass.

Each dipolariton eigenstate is a linear combination of excitonic and photonic components with the generalized Hopfield coefficients:

$$|\mathbf{Q}, S\rangle_{DP} = \sum_{j=IX,DX,C} c_j(Q, V) |\mathbf{Q}, S\rangle_j. \quad (1.48)$$

Here, the index j spans over indirect (IX), direct (DX) exciton and cavity photon (C) states. \mathbf{Q} and S designate quasi-momentum and total angular momentum projection (below denoted as spin for simplicity) on the QWs plane (in units of \hbar). These coefficients may be obtained by exact diagonalization of the Hamiltonian (4.36), but their analytical form is quite cumbersome and we do not present them here.

The excitonic part of dipolaritons, responsible for their scattering, reads:

$$|\mathbf{Q}, S\rangle_X = c_{IX}(Q, V) |\mathbf{Q}, S\rangle_{IX} + c_{DX}(Q, V) |\mathbf{Q}, S\rangle_{DX}, \quad (1.49)$$

as it is responsible for their Coulomb interactions. The quantum states $|\mathbf{Q}, S\rangle_{IX}$ and $|\mathbf{Q}, S\rangle_{DX}$ represent an IX and a DX in the 1s state with center of mass momentum \mathbf{Q} and spin $S = \pm 1$, described by wavefunctions having a common form with decoupled motional and spin parts [29]:

$$\Psi^{\mathbf{Q}, S}(\mathbf{r}_e, \mathbf{r}_h) = \Psi^{\mathbf{Q}}(\mathbf{R}) \Psi^\rho(\rho) \Psi^z(z_e, z_h) \chi^S(s_e, j_h), \quad (1.50)$$

where $\mathbf{R} = (m_e \mathbf{r}_e + m_h \mathbf{r}_h)_{QW} / (m_e + m_h)$ is the exciton center of mass projection on the QW plane, $\rho = (\mathbf{r}_e - \mathbf{r}_h)_{QW}$ is the in-plane distance between the electron and the hole bound into the exciton, $z_{e(h)}$ is the electron (hole) coordinate in the QW growth direction and s_e, j_h are the electron spin and the heavy hole angular momentum projections on the z axis. The center-of-mass motion part $\Psi^{\mathbf{Q}}(\mathbf{R}) = S^{-1/2} \exp(-i\mathbf{Q}\mathbf{R})$, where S is the normalization area, is the same plane wave for both types of excitons. The internal motion part $\Psi_\rho(\rho)$ reads:

$$\Psi_\rho(\rho) = \frac{1}{\sqrt{2\pi b(b+r_0)}} \exp\left(\frac{-\sqrt{\rho^2 + r_0^2} + r_0}{2b}\right),$$

where b and r_0 parameters are different for IX and DX. The out-of-plane part may be set as $\Psi^z(z_e, z_h) = \delta(z_e - Z_e) \delta(z_h - Z_h)$, where Z_e and Z_h are the coordinates of the QWs where the electron and the hole are confined. They coincide for DX and differ in the case of IX. The spin part $\chi^S(s_e, j_h)$ plays a major role in the calculation of the scattering matrix elements as they drastically depend on the spin configuration of a dipolariton pair. Only the exciton states with a total spin $S = \pm 1$ are coupled to the photonic mode, thus forming dipolaritons. For them, we define the spin part as $\chi^{\pm 1}(s_e, j_h) = \delta_{s_e, \mp 1/2} \delta_{j_h, \pm 3/2}$.

Chapter 2

Spin dynamics and topological effects in physics of indirect excitons

Indirect excitons can be transported over sufficiently long distances up to several micrometers [32], which allows to consider them as potential alternative carriers of information. Lacking the total charge, they possess the spin degree of freedom, which can be used in novel spintronics paradigm. IX condensates present a nontrivial case of bispinor BEC-type system. Its spin manipulation and the study of its dynamics therefore are promising from the fundamental point of view and because of the possible applications.

The experimental study of the IX spin behaviour is in most cases conducted via polarization-resolved IX photoemission spectra measurements with spatial and time resolution [33]. This type of experiment, however, leaves dark excitonic states with spin projection ± 2 on CQW growth axis out of view, since the emission of photons is forbidden for these excitons by the selection rules. At the same time, the dark excitonic spin states are lower than the bright ones in energy due to electron-hole short-range exchange [34]. Although the bright-dark splitting value is much smaller for IX in comparison with conventional QW excitons due to the electron-hole spatial separation, it may be enough for the condensation to occur on the dark states [35] instead of the bright ones. On the other hand, the spatial coherence of observed IX light emission [17] clearly demonstrated a macroscopical occupation of bright excitonic states. An experimental measurement technique based on nonlinear optical effects, optically induced reflectivity and Kerr rotation, can be able to resolve this contradiction. The theoretical base for this technique is described in Section 1.

The spin physics of a non-coherent gas of IXs is described using the density matrix formalism with Lindblad term phenomenologically included into the quantum Liouville equation describing the density matrix evolution. This approach, as well as the microscopic origins of the IX spin relaxation, are given in Section 2.

The situation is completely different for IX condensates obeying bispinor Gross-Pitaevskii equation. In this model, the evolution of four spin components of the condensate wavefunction is defined by the Hamiltonian taking into account the spin-orbit interaction and Coulomb interactions of IXs. Topologically nontrivial skyrmion-like configurations emerge in the condensate with specific boundary conditions. Section 3 is devoted to these effects.

2.1 Nonlinear optical spectroscopy of indirect excitons

The nonlinear optical effects such as the photoinduced reflectivity and Kerr rotation are often used for the study of excitons in QWs [36]. A nonlinear optical process, in its broadest definition, is a process in which the optical properties of the medium depend on the electromagnetic field itself. In the case of the optical pumping in semiconductors, the light-induced variations of the optical properties of the medium can persist for a long time after the perturbing light is switched off. In this case, a pump-probe arrangement can be used, with pump and probe interactions separated in time. This allows the time-resolved studies of optical and spin coherence in the medium. In semiconductor QWs, a resonant optical pumping of DX resonance with circularly polarized light, and subsequent detection of the pump-induced dispersive response are widely used to study the exciton population and spin dynamics. Experimentally, either the modification of the probe intensity (photoinduced reflectivity) or the rotation of the polarization plane of the linearly polarized probe pulse (photoinduced Kerr rotation) are measured. These signals are proportional to the square of the oscillator strength of the excitonic transition and have a pronounced resonant character. Thus, because the oscillator strength of IX is orders of magnitude lower than for DX, it is impossible to simply transpose the ideas developed for nonlinear spectroscopy of DX to IX.

However, IXs, despite their vanishing oscillator strengths, can induce measurable photoinduced reflectivity and Kerr rotation and therefore can be studied via these effects. Such study relies on two properties of the CQWs structures. The first essential property is the spin conserving tunneling of electrons between the QWs [37]. It allows creating a substantial spin polarization of IX via the optical generation of circularly polarized DXs. This has been unambiguously demonstrated by polarization-resolved photoluminescence experiments [38]. The second important effect is the spin-dependent coupling between DX and IX states. This coupling is quite strong in CQW, where each IX and each DX have either holes or electrons located in the same QW. This is why the presence of IX population in the structure alters the properties of the DX resonance, mainly via the spin-dependent exchange interactions. Probing an exciton sub-system with a low oscillator strength using an exciton sub-system with a higher oscillator strength was earlier explored in the studies of IXs by linear methods: the optically DXs with spin ± 2 [39] or with high momenta beyond the light cone [40, 41, 7] were probed via the energy shift and optical decay rate of bright IXs with spin ± 1 and momenta within the radiative zone, see e.g. [42]. Therefore, we suggest that the detection of IX population and spin polarization can also be realized by exploiting the DX resonance. The Kerr rotation measured at the DX resonance is a sensitive method to access populations and spin polarizations of both bright and dark IX states. It may be used, in particular, for the studies of dark excitons which strongly affect the spin properties of excitonic condensates [33, 30]. The phenomenological description of the two nonlinear effects measured at the DX transition frequency in presence of IXs due to the IX-DX coupling is given in Subsection 1. It is based on the non-local dielectric response model and predicts the spectral dependence of photoinduced Kerr rotation and reflectivity induced by IXs, allowing to analyze the impact of bright and dark IXs and DXs on these spectra.

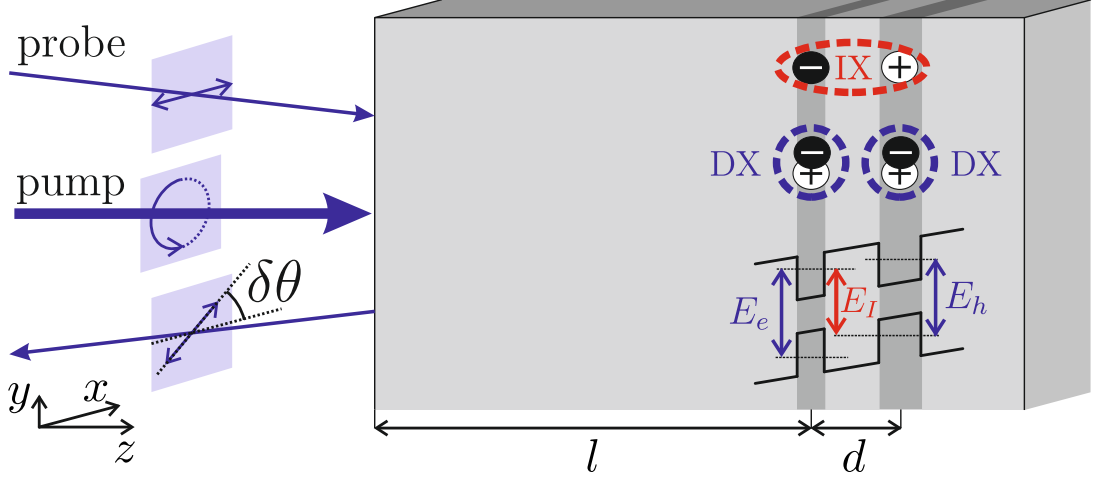


Figure 2.1: Sketch of pump-probe experiment on CQWs sample. DX and IX optical transitions are shown. Both pump and probe frequencies are resonant with one of DX resonance.

The effect of the DX-IX interaction is studied quantitatively in Subsection 2, by calculating the spin-dependent shifts of the DX resonances in the presence of spin-polarized gas of IXs within the Hartree-Fock and the effective mass approximations. The two other mechanisms of nonlinear optical effects, phase-space filling, and homogeneous line broadening are discussed in Subsection 3 and Subsection 4 respectively.

2.1.1 Photoinduced reflectivity and Kerr rotation

This Section presents the phenomenological analysis of the effect of the IX population in the CQW structure on the polarization and intensity of the linearly polarized weak probe wave, resonant with the DX transition. The considered CQW structure is schematically shown in Figure 2.1. It consists of two QWs, separated by a potential barrier of the width d and covered by a thick barrier layer of the width l . A static electric field is applied along the z -axis, perpendicular to the CQW plane. Two optically-active ground DX levels in this system with total spin ± 1 are denoted as E_e and E_h , and the corresponding wavefunctions as Ψ_e and Ψ_h , respectively. Dark DX states characterised by total spin ± 2 have zero oscillator strength and do not contribute to the reflectivity spectra. Hereafter, the indices e (h) denote the QW where electrons (holes) are driven by the static gate voltage. In the case of two identical quantum wells, DX levels split into symmetrical and antisymmetrical states with very small energy difference [43] that are ignored here and assumed to be $E_e = E_h$. Furthermore, the regimes of weak and strong coupling are distinguished between these levels.

The weak coupling implies coexistence of two spatially separated DX states with the wavefunctions Ψ_e and Ψ_h and is mostly relevant to asymmetric QWs. In symmetric QWs DX levels are strongly coupled and form symmetric (Ψ_s) and antisymmetric (Ψ_a) combinations of excitons in left and right QWs.

The electric field of the incident probe beam can be written as $\mathbf{E} = \mathbf{e}_x E_0 e^{i(kz - \omega t)}$. Here the normally incident probe beam characterized by the wavevector k and linearly

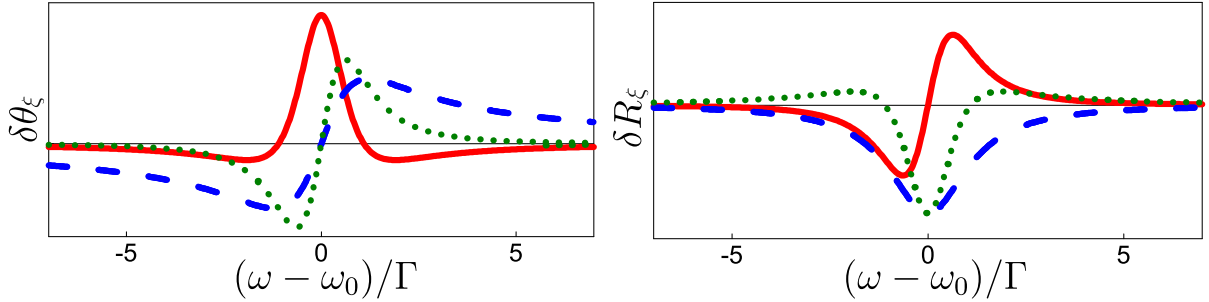


Figure 2.2: Kerr rotation ($\delta\theta_\xi$) and photoinduced reflectivity (δR_ξ) spectra, calculated from Eq. (2.7) assuming different nonlinearities: DX energy shift ($\xi = \omega_0$, red solid line), DX transition saturation ($\xi = \Gamma_0$, blue dashed line) and DX non-radiative broadening ($\xi = \Gamma$, green dotted line). From Nalitov et al. (2014) [45].

polarized along the x -axis propagates along z -axis. The amplitude reflection coefficient from QW for such wave in the vicinity of one of DX transition frequencies $\omega_0 = E_{e(h)}/\hbar$ is related to the exciton wavefunction $\Psi = \Psi_{e(h)}(\rho, z_{el}, z_{hh})$ by a textbook formula [44] taken in the limit of $kd \ll 1$:

$$r_{\text{QW}}(\omega) = \frac{i\Gamma_0}{\omega_0 - \omega - i(\Gamma_0 + \Gamma)}, \quad (2.1)$$

where the radiative decay rate is given in

$$\Gamma_0 = \frac{\pi}{2} k\omega_{LT} a_B^3 S \left[\int \Psi(\rho = 0, z, z) dz \right]^2, \quad (2.2)$$

ω_{LT} is the longitudinal-transverse splitting, a_B is the bulk exciton Bohr radius, S is the sample normalization area, and Γ is the exciton non-radiative broadening, ρ is the in-plane separation of electron and hole, $z_{el(hh)}$ are electron (hole) z coordinates. For the weak coupling case, the phase gained by light propagating between QWs is neglected, assuming $kd \ll 1$. In this case, one can distinguish the reflection coefficients r_e and r_h corresponding to $\Psi_{e/h}$ states. On the other hand, in the strong coupling regime, only r_s for the symmetric combination $\Psi_s = (\Psi_e + \Psi_h)/\sqrt{2}$ is important since for the antisymmetric exciton state the radiative decay is essentially suppressed.

In the most experimentally relevant case $|r_{\text{QW}}(\omega)| \ll 1$. Taking into account the interference between waves reflected from the surface of the cap layer having a refractive index n and those reflected from CQWs, the barrier and the covering layer, the total reflectivity coefficient is

$$r = \frac{1-n}{1+n} + e^{2ikl} \frac{4n}{(n+1)^2} r_{\text{QW}}. \quad (2.3)$$

Here, the re-reflections, the reflections from deeper layers of the structure, and the difference of the refraction indices of the CQWs are neglected.

Below, $r(\omega)$ will mean the reflection coefficient from the whole structure.

The presence of IXs can affect the DX transition parameters ω_0 , Γ_0 and Γ through various mechanisms. The spin-dependent Coulomb interactions between IXs and DXs lead to the blue shift of DX levels and, in the case when IXs are polarized, their spin-splitting. IXs also saturate DX transitions due to the phase space filling effect, since

IXs consist of electrons and holes in the same QWs as DXs. This effect is again spin-dependent. Finally, IXs may affect the non-radiative decay of DXs through the scattering processes involving spin-dependent transitions between DX and IX levels, or by screening the disorder potential. The renormalisation of exciton resonance frequencies and spin-splittings due to these interactions is responsible for the modulation of reflectivity and Kerr rotation spectra. Note that exciton resonance frequency renormalization due to the interaction with the carriers at other levels was also studied for excitons in dense electron-hole magnetoplasma [46] and for bright and dark indirect excitons [35]. Indeed, all the interaction effects listed above can be accounted for by correcting the reflection coefficients for two circularly polarized components of the probe pulse, σ^\pm :

$$\delta r^\pm = \frac{\partial r}{\partial \omega_0} \delta \omega_0^\pm + \frac{\partial r}{\partial \Gamma_0} \delta \Gamma_0^\pm + \frac{\partial r}{\partial \Gamma} \delta \Gamma^\pm \quad (2.4)$$

The electric field of the reflected probe wave can be expressed in terms of these corrections as

$$\mathbf{E}_r = E_0 \frac{1}{\sqrt{2}} [(r + \delta r^+) \mathbf{e}_+ + (r + \delta r^-) \mathbf{e}_-] e^{i(kz - \omega t)}. \quad (2.5)$$

Here the basis of right and left circularly polarized waves $\mathbf{e}_\pm = (\mathbf{e}_x \pm i\mathbf{e}_y)/\sqrt{2}$ is used. One can see, that in the most general case, the corrections of the reflection coefficient may induce (i) circular dichroism, which leads to the build up of circular polarization, (ii) circular birefringence, which leads to the rotation of the polarization plane, or Kerr rotation, and (iii) modification of the probe intensity. In the limit of $|\delta r^\pm| \ll |r_{\text{QW}}| \ll 1$ Kerr rotation angle is linear in $(\delta r^+ - \delta r^-)$ [47], while photoinduced reflectivity is linear in $(\delta r^+ + \delta r^-)$:

$$\delta \theta = -\text{Im} \left\{ \frac{\delta r^+ - \delta r^-}{2r} \right\}, \quad \delta R = |r|^2 \text{Re} \left\{ \frac{\delta r^+ + \delta r^-}{r} \right\}. \quad (2.6)$$

Substitution of Eqs.(2.3, 2.4) into Eq.(2.6) gives the expressions of the three contributions to the photoinduced Kerr rotation and the reflectivity as a function of corresponding modification of the excitonic characteristic ξ , which spans over the resonant frequency, radiative and non-radiative decay rates $\xi = \omega_0, \Gamma_0, \Gamma$:

$$\begin{aligned} \delta \theta_\xi &= \frac{2n}{n^2 - 1} \text{Im} \left\{ e^{2ikl} \frac{\partial r_{\text{QW}}}{\partial \xi} \right\} (\delta \xi^+ - \delta \xi^-), \\ \delta R_\xi &= -\frac{4n(n-1)}{(n+1)^3} \text{Re} \left\{ e^{2ikl} \frac{\partial r_{\text{QW}}}{\partial \xi} \right\} (\delta \xi^+ + \delta \xi^-), \\ \delta \theta &= \sum_\xi \delta \theta_\xi, \quad \delta R = \sum_\xi \delta R_\xi. \end{aligned} \quad (2.7)$$

Figure 2.4 shows the contributions of different mechanisms to photoinduced Kerr rotation and reflectivity spectra in the vicinity of the DX resonance, calculated using Eqs.(2.7), assuming $2kl \ll 1$ and $n > 1$, $\delta \omega_0^- = \delta \Gamma_0^- = \delta \Gamma^- = 0$, and normalized so that $\delta \omega_0^+/\Gamma = -\delta \Gamma_0^+/\Gamma_0 = \delta \Gamma^+/\Gamma$. This corresponds to: blue shift of the DX energy $\delta \omega_0$ (red solid line), reduction of the DX oscillator strength $\delta \Gamma_0$ (blue dashed line) and enhancement of non-radiative decay of DX, $\delta \Gamma$ (green dotted line). One can see that the

spectral profiles are qualitatively different. Thus, measuring the photoinduced spectra should make possible the identification of the underlying nonlinearity. Note also, that spectral shape depends on the value of the phase factor $2kl$ in the Eq. (2.7), so that $\delta\theta$ and δR transform as imaginary and real parts of a complex value between the braces.

The roadmap for the measurement of the pump-probe signal induced by IX and determination of the underlying nonlinearities can be as follows. First of all, in real time-resolved pump-probe experiments, one operates with short pulses of light rather than with monochromatic waves. Therefore, to measure spectral dependence of the nonlinear signal the probe spectral width must be smaller than the DX linewidth $(\Gamma + \Gamma_0)$, which is accessible experimentally [48]. Second, one should avoid any contribution of DX population to the nonlinear signal. This can be easily realized by setting the delay between pump and probe pulses sufficiently long, because the DX lifetime does not exceed 500 ps, while the IX lifetime is at least an order of magnitude longer. Finally, fitting the measured pump-induced reflectivity and Kerr rotation spectra to Eq.(2.6) assuming different excitonic nonlinearities, it should be possible to determine the relative importance of different mechanisms of the DX-IX interaction. The Faraday rotation spectroscopy provides the same information as the Kerr rotation spectroscopy with the only difference in the detection geometry: the transmitted signal is studied in the Faraday configuration, while in Kerr configuration the reflected signal is detected.

2.1.2 Exciton spin-anisotropic exchange interactions

The following Subsection demonstrates that at least one of the discussed mechanisms, namely the spin-selective energy shift of DX resonance, indeed produces a measurable nonlinear signal in realistic CQW structures. Following the approach of [49, 50, 30], it is possible to use the Hartree-Fock and the effective mass approximations to find the matrix elements of the Coulomb interaction Hamiltonian and estimate the strength of the DX-IX Coulomb interaction in a typical CQW structure. The objective is to calculate the energy shifts of the bright DX levels $E_e^{\pm 1}$ and $E_h^{\pm 1}$ induced in the first order by the population of both bright ($n_I^{\pm 1}$) and dark ($n_I^{\pm 2}$) IX states. Also it is possible to estimate the IX-IX interaction energy within the same model, to compare it with the PL line-shifts observed experimentally and with the other existing theoretical results.

The exciton-exciton interaction energy is calculated in the first order perturbation theory. The following orders would account for effects like mentioned interaction between IX static dipole moment and induced dipole moment of DX. They result in corrections, in particular, to the IX-DX interaction energy, proportional to the greater powers of the exciton density. this approximation is therefore valid in the low-density limit.

A wavefunction of a single 1s-exciton $\Psi_{\mathbf{Q}}(\mathbf{r}_{el}, \mathbf{r}_{hh})$, characterized by a center of mass wave vector \mathbf{Q} , may be decoupled into translational motion in the QW plane, the electron and hole motion along z axis and the relative in-plane motion of electron and hole:

$$\Psi_{\mathbf{Q}}^{\text{I(D)}}(\rho, z_{el}, z_{hh}) = \frac{1}{\sqrt{S}} \exp(i\mathbf{Q}\mathbf{R}_{c.m.}) \Psi_z^{\text{I(D)}}(z_{el}, z_{hh}) \Psi_{\rho}(\rho), \quad (2.8)$$

where $\mathbf{R}_{c.m.} = (m_{el}\mathbf{r}_{el}^{\parallel} + m_{hh}\mathbf{r}_{hh}^{\parallel})/(m_{el} + m_{hh})$, $\rho = \mathbf{r}_{el}^{\parallel} - \mathbf{r}_{hh}^{\parallel}$, $\mathbf{r}_{el, hh}^{\parallel}$ are the electron and hole radius vector projections on the CQW plane, $m_{el, hh}$ are the electron and hole in-plane effective masses. The relative motion part of this wavefunction $\Psi_{\rho}(\rho)$ for both DXs and

IXs can be found from the solution of a 2D radial Schrodinger equation [51] or by using the variational approach with the trial function of the form [30]:

$$\Psi_\rho(\rho) = \frac{1}{\sqrt{2\pi b(b+r_0)}} \exp\left(\frac{-\sqrt{\rho^2 + r_0^2} + r_0}{2b}\right), \quad (2.9)$$

with r_0 and b as variational parameters. The corresponding mean square of the in-plane radius for this exciton wavefunction is given by:

$$p^2 = \frac{2b}{b+r_0}(r_0^2 + 3br_0 + 3b^2). \quad (2.10)$$

Figure 2.4 (a) shows the ψ_ρ parameters p , b and r_0 as a function of the QWs separation d , as obtained from the variational procedure. In the limiting case of $d = 0$, Eq. (2.10) coincides with the exact solution for the in-plane radius of the DX wavefunction with $r_0 = 0$ and $b = a_B/4$. When the separation between QWs increases, the in-plane extension of the IX wavefunction grows sublinearly. The wave function in z -direction in the limit of two infinitely thin QWs reads:

$$\Psi_z^{e(h)} = \sqrt{\delta(z_{el} - Z_{e(h)})\delta(z_{hh} - Z_{e(h)})},$$

for DX state, and for IX state

$$\Psi_z^I = \sqrt{\delta(z_{el} - Z_e)\delta(z_{hh} - Z_h)},$$

where $Z_{e(h)}$ are the QW coordinates in the growth direction.

The spin part of the exciton wavefunction $\chi_S(s, j) = \delta_{S, s+j}$, where S , s , j are exciton, electron and hole spin projections on z axis, is identical for IX and DX.

Exciton pair wavefunction is obtained by antisymmetrization of the product of two single-exciton wavefunctions with respect to the permutation of either electrons or holes. For a pair of excitons, characterized by momenta \mathbf{Q} , \mathbf{Q}' and spins S , S' , it reads:

$$\begin{aligned} \Phi_{\mathbf{Q}, \mathbf{S}, \mathbf{Q}', \mathbf{S}'}^{l, m}(\mathbf{r}_{el}, s, \mathbf{r}_{hh}, j, \mathbf{r}'_{el}, s', \mathbf{r}'_{hh}, j') = & \frac{1}{2} \left[\Psi_{\mathbf{Q}}^l(\mathbf{r}_{el}, \mathbf{r}_{hh})\chi_S(s, j)\Psi_{\mathbf{Q}'}^m(\mathbf{r}'_{el}, \mathbf{r}'_{hh})\chi_{S'}(s', j') - \right. \\ & \Psi_{\mathbf{Q}}^l(\mathbf{r}_{el}', \mathbf{r}_{hh})\chi_S(s', j)\Psi_{\mathbf{Q}'}^m(\mathbf{r}_{el}, \mathbf{r}'_{hh})\chi_{S'}(s, j') - \\ & \Psi_{\mathbf{Q}}^l(\mathbf{r}_{el}, \mathbf{r}'_{hh})\chi_S(s, j')\Psi_{\mathbf{Q}'}^m(\mathbf{r}'_{el}, \mathbf{r}_{hh})\chi_{S'}(s', j) + \\ & \left. \Psi_{\mathbf{Q}}^l(\mathbf{r}'_{el}, \mathbf{r}'_{hh})\chi_S(s', j')\Psi_{\mathbf{Q}'}^m(\mathbf{r}_{el}, \mathbf{r}_{hh})\chi_{S'}(s, j) \right] \end{aligned} \quad (2.11)$$

Here superscripts l and m stand for I or D.

In Born approximation, scattering of such a pair of excitons is governed by the matrix element $\langle \mathbf{Q}_f, S_f, \mathbf{Q}'_f, S'_f | \widehat{V} | \mathbf{Q}, S, \mathbf{Q}', S' \rangle$ of interexcitonic Coulomb interactions operator:

$$\widehat{V} = \frac{e^2}{\epsilon} \left[\frac{1}{|\mathbf{r}_{el} - \mathbf{r}'_{el}|} + \frac{1}{|\mathbf{r}_{hh} - \mathbf{r}'_{hh}|} - \frac{1}{|\mathbf{r}_{el} - \mathbf{r}'_{hh}|} - \frac{1}{|\mathbf{r}_{hh} - \mathbf{r}'_{el}|} \right] \quad (2.12)$$

Here ϵ is the material permittivity, e is the electron charge.

The shifts of DXs and IXs energy levels are the averages of the Coulomb interaction energy over a two-exciton state and are obtained by equating initial and final states to

	$e \downarrow\uparrow (+1)$	$e \uparrow\downarrow (-1)$	$h \downarrow\uparrow (+1)$	$h \uparrow\downarrow (-1)$
$I \uparrow\uparrow (+2)$	0	V_{exch}^{D-1}	V_{exch}^{D-1}	0
$I \downarrow\uparrow (+1)$	V_{exch}^{D-1}	0	V_{exch}^{D-1}	0
$I \uparrow\downarrow (-1)$	0	V_{exch}^{D-1}	0	V_{exch}^{D-1}
$I \downarrow\downarrow (-2)$	V_{exch}^{D-1}	0	0	V_{exch}^{D-1}

Table 2.1: Matrix elements contributing to the interaction of four possible IX spin states with bright DX states. Indices e , h and I refer to DX in electron and hole QWs and IX states, the direction of the arrows defines the electron ($\uparrow\downarrow$) and hole ($\uparrow\downarrow$) angular momentum projection.

	$I \downarrow\uparrow (+1)$	$I \uparrow\downarrow (-1)$
$I \uparrow\uparrow (+2)$	$V_{\text{dir}}^{I-1} + V_{\text{exch}}^{I-1}$	$V_{\text{dir}}^{I-1} + V_{\text{exch}}^{I-1}$
$I \downarrow\uparrow (+1)$	$2(V_{\text{dir}}^{I-1} + V_{\text{exch}}^{I-1})$	V_{dir}^{I-1}
$I \uparrow\downarrow (-1)$	V_{dir}^{I-1}	$2(V_{\text{dir}}^{I-1} + V_{\text{exch}}^{I-1})$
$I \downarrow\downarrow (-2)$	$V_{\text{dir}}^{I-1} + V_{\text{exch}}^{I-1}$	$V_{\text{dir}}^{I-1} + V_{\text{exch}}^{I-1}$

Table 2.2: Matrix elements contributing to the interaction of four possible IX spin states with bright IX states. The direction of the arrows defines the electron ($\uparrow\downarrow$) and hole ($\uparrow\downarrow$) angular momentum projection.

the zero momentum exciton pair in scattering matrix elements. In the general case of two excitons with spin projections on the z axis S , S' , corresponding to the electron spin projections s , s' and the heavy hole angular momentum projections j , j' this average can be rewritten as a sum of direct and exchange integrals [49]:

$$V_{SS'}^{l,m} = V_{\text{dir}}^{l,m} + \delta_{SS'} V_{\text{exch},X}^{l,m} + \delta_{ss'} V_{\text{exch},el}^{l,m} + \delta_{jj'} V_{\text{exch},hh}^{l,m}, \quad (2.13)$$

where δ_{ij} is the Kronecker delta operator. The first term V_{dir} is the direct Coulomb term which corresponds to the classical electrostatic interaction between the two excitons:

$$V_{\text{dir}}^{l,m} = \int d^3\mathbf{r}_{el} d^3\mathbf{r}_{hh} d^3\mathbf{r}'_{el} d^3\mathbf{r}'_{hh} \Psi_0^l(\mathbf{r}_{el}, \mathbf{r}_{hh}) \Psi_0^m(\mathbf{r}'_{el}, \mathbf{r}'_{hh}) \widehat{V} \Psi_0^l(\mathbf{r}_{el}, \mathbf{r}_{hh}) \Psi_0^m(\mathbf{r}'_{el}, \mathbf{r}'_{hh}), \quad (2.14)$$

$V_{\text{exch},X}$ is the term describing the simultaneous exchange of the two identical electrons and the two identical holes between two excitons:

$$V_{\text{exch},X}^{l,m} = \int d^3\mathbf{r}_{el} d^3\mathbf{r}_{hh} d^3\mathbf{r}'_{el} d^3\mathbf{r}'_{hh} \Psi_0^l(\mathbf{r}'_{el}, \mathbf{r}'_{hh}) \Psi_0^m(\mathbf{r}_{el}, \mathbf{r}_{hh}) \widehat{V} \Psi_0^l(\mathbf{r}_{el}, \mathbf{r}_{hh}) \Psi_0^m(\mathbf{r}'_{el}, \mathbf{r}'_{hh}). \quad (2.15)$$

The third term V_{exch}^{el} is the term due to the electron-electron exchange:

$$V_{\text{exch},X}^{l,m} = \int d^3\mathbf{r}_{el} d^3\mathbf{r}_{hh} d^3\mathbf{r}'_{el} d^3\mathbf{r}'_{hh} \Psi_0^l(\mathbf{r}'_{el}, \mathbf{r}_{hh}) \Psi_0^m(\mathbf{r}_{el}, \mathbf{r}'_{hh}) \widehat{V} \Psi_0^l(\mathbf{r}_{el}, \mathbf{r}_{hh}) \Psi_0^m(\mathbf{r}'_{el}, \mathbf{r}'_{hh}), \quad (2.16)$$

while V_{exch}^{hh} is the analogous contribution arising from the hole-hole exchange:

$$V_{\text{exch},X}^{l,m} = \int d^3\mathbf{r}_{el} d^3\mathbf{r}_{hh} d^3\mathbf{r}'_{el} d^3\mathbf{r}'_{hh} \Psi_0^l(\mathbf{r}_{el}, \mathbf{r}'_{hh}) \Psi_0^m(\mathbf{r}'_{el}, \mathbf{r}_{hh}) \widehat{V} \Psi_0^l(\mathbf{r}_{el}, \mathbf{r}_{hh}) \Psi_0^m(\mathbf{r}'_{el}, \mathbf{r}'_{hh}), \quad (2.17)$$

In the limit of zero transferred momentum one can approximate $V_{\text{dir}}^{l,l} = V_{\text{exch},X}^{l,l}$ and $V_{\text{exch},el}^{l,l} = V_{\text{exch},hh}^{l,l}$ [49, 30]. In realistic systems, the electron and hole exchange integrals may be different for several reasons, including the differences in the Bloch amplitudes of electrons and holes and the differences in the penetration depths of their wavefunctions into the barrier layer. Besides this, if two quantum wells are not identical, $V_{\text{exch},el}^{l,l} \neq V_{\text{exch},hh}^{l,l}$, in general. It turns out that in this case the Kerr rotation and differential spectra provide information not only on the population but also on the spin polarization of the dark IX states. These effects will be discussed in the system of symmetric QWs, where $V_{\text{exch},el} = V_{\text{exch},hh}$ is assumed, as well as in the system of asymmetric QWs, where $V_{\text{exch},el} \neq V_{\text{exch},hh}$ for the sake of comparison.

Table 2.1 provides a convenient visual representation of all the interaction terms in Eq. (3.23). Along the vertical axis, all IX spin states are listed. Four columns show the matrix elements responsible for their interaction with a pair of bright excitons in each QW. The mutual orientation of the electron and hole spin in each exciton state is shown by the arrows. Analogous representation of the interactions between all the four IX spin states and the bright IX states are given by Table 2.2. All possible carrier exchange interactions are additionally illustrated in graphical form in Fig. 2.3.

For the IX-DX interaction it can be shown that $V_{\text{dir}}^{I,D} = V_{\text{exch},X}^{I,X} = 0$ due to the absence of stationary dipole moment for DXs and the assumed zero overlap of the DX and IX wavefunctions. Therefore, the energy shifts of DXs due to IXs are governed by just one carrier exchange matrix element $V_{\text{exch},el}^{D,I} = V_{\text{exch},hh}^{D,I} \equiv V_{\text{exch}}^{D-I}$. As can be seen from Table 1, carrier exchange interaction for bright IXs is only possible with DXs with the same spin in both QWs, while DXs interacting with dark IXs have different spin projection signs in left and right QWs.

In the case of IX-IX interaction the direct Coulomb term does not vanish in the Born approximation due to the oriented dipole moments of IXs, and the energy shifts of IXs are expressed in terms of two interaction constants $V_{\text{dir}}^{I,I} = V_{\text{exch},X}^{I,I} \equiv V_{\text{dir}}^{I-I}$ and $V_{\text{exch},el}^{I,I} = V_{\text{exch},hh}^{I,I} \equiv V_{\text{exch}}^{I-I}$. The direct Coulomb term is spin independent and enters every line in Table 1, while the carrier exchange between two IXs is only possible if either electrons or holes have the same spin projections. Two IXs with both electrons and holes having the same spin projections can also exchange them simultaneously. This gives the factor 2 before V_{dir}^{I-I} in corresponding cells of Table I.

Using the Table I, one can write the expressions for the DX and IX energy shifts, induced by the IX population. The bright DX energy shifts depend on the population of the IXs with different spin projections on the growth axis as:

$$\delta E_e^\pm = V_{\text{exch}}^{D-I}(n_I^{\pm 1} + n_I^{\mp 2}), \quad \delta E_h^\pm = V_{\text{exch}}^{D-I}(n_I^{\pm 1} + n_I^{\pm 2}). \quad (2.18)$$

The energy shifts of bright IXs are related to IXs populations in a similar way (see Table II):

$$\begin{aligned} \delta E_I^\pm &= (V_{\text{dir}}^{I-I} + V_{\text{exch}}^{I-I})(n_I^{+2} + n_I^{-2}) + \\ &+ 2(V_{\text{dir}}^{I-I} + V_{\text{exch}}^{I-I})n_I^{\pm 1} + V_{\text{dir}}^{I-I}n_I^{\mp 1} \end{aligned} \quad (2.19)$$

The listed interaction constants are the matrix elements of interaction operator (3.23):

$$\begin{aligned}
V_{\text{exch}}^{\text{D-I}} &= \int d^3\mathbf{r}_{el}d^3\mathbf{r}_{hh}d^3\mathbf{r}'_{el}d^3\mathbf{r}'_{hh}\Psi_0^{\text{D}}(\mathbf{r}_{el},\mathbf{r}_{hh})\Psi_0^{\text{I}}(\mathbf{r}'_{el},\mathbf{r}'_{hh})\widehat{V}\Psi_0^{\text{D}}(\mathbf{r}'_{el},\mathbf{r}_{hh})\Psi_0^{\text{I}}(\mathbf{r}_{el},\mathbf{r}'_{hh}), \\
V_{\text{dir}}^{\text{I-I}} &= \int d^3\mathbf{r}_{el}d^3\mathbf{r}_{hh}d^3\mathbf{r}'_{el}d^3\mathbf{r}'_{hh}\Psi_0^{\text{I}}(\mathbf{r}_{el},\mathbf{r}_{hh})\Psi_0^{\text{I}}(\mathbf{r}'_{el},\mathbf{r}'_{hh})\widehat{V}\Psi_0^{\text{I}}(\mathbf{r}_{el},\mathbf{r}_{hh})\Psi_0^{\text{I}}(\mathbf{r}'_{el},\mathbf{r}'_{hh}), \\
V_{\text{exch}}^{\text{I-I}} &= \int d^3\mathbf{r}_{el}d^3\mathbf{r}_{hh}d^3\mathbf{r}'_{el}d^3\mathbf{r}'_{hh}\Psi_0^{\text{I}}(\mathbf{r}_{el},\mathbf{r}_{hh})\Psi_0^{\text{I}}(\mathbf{r}'_{el},\mathbf{r}'_{hh})\widehat{V}\Psi_0^{\text{I}}(\mathbf{r}'_{el},\mathbf{r}_{hh})\Psi_0^{\text{I}}(\mathbf{r}_{el},\mathbf{r}'_{hh}). \quad (2.20)
\end{aligned}$$

While $V_{\text{dir}}^{\text{I-I}}$ can be found analytically [30], $V_{\text{exch}}^{\text{I-I}}$ and $V_{\text{exch}}^{\text{D-I}}$ should be calculated numerically using *e.g.* the Monte-Carlo integration method. The result of the matrix elements calculation by the Monte Carlo method is shown in Figure 2.4 (b) in the units of Ra_B^2 , where R and a_B are the bulk exciton Rydberg energy and Bohr radius, respectively. One can see that $V_{\text{exch}}^{\text{D-I}}$ almost does not depend on the separation between the QWs (dash-dotted line). In contrast, both $V_{\text{exch}}^{\text{I-I}}$ (solid line) and $V_{\text{dir}}^{\text{I-I}}$ (dashed line) terms increase in absolute value with increasing distance between QWs, but have different signs. This result is in a good agreement with the calculations of Refs. [49, 30].

To further check the validity of our approach, it is instructive to calculate using Eqs. (2.18)-(2.19) the PL shifts of IX and DX lines in a typical CQW structure. It is assumed that most of the IXs are depolarized, so that the energy shifts of the light emitting states should be averaged over the IX spin projections. This gives:

$$\begin{aligned}
\delta E_e &= \delta E_h = \frac{1}{2}V_{\text{exch}}^{\text{D-I}}n_I \\
\delta E_I &= \left(\frac{5}{4}V_{\text{dir}}^{\text{I-I}} + V_{\text{exch}}^{\text{I-I}}\right)n_I, \quad (2.21)
\end{aligned}$$

where n_I is the total density of IXs. The resulting energy shifts normalized to the unitary IX density $n_{10} = a_B^{-2}$ are shown in Figure 2.4 (c). Note that the shifts are obtained assuming a negligible tunnel coupling between QWs, which is incorrect in the vicinity of $d = 0$, where transition from weak to strong tunnel coupling occurs. In the latter case the DX PL shift is twice higher. One can see that for a given density of IX excitons, the PL shift of the IX line exceeds the DX line shift. This difference dramatically enhances with increasing separation between QWs. For IXs densities $\sim 10^{10} \text{ cm}^{-2}$ and $d \sim 10 \text{ nm}$, the DX and IX PL shifts are of the order of 0.1 meV and 1 meV respectively. This is consistent with the experimental observations [9].

Now it is possible to write down the expressions for both Kerr rotation and the photoinduced reflectivity in the vicinity of each DX resonance. Substituting Eq.(2.18) into Eq.(2.7) with $E_{e(h)}$ as ξ these signals related to the IX populations read:

$$\begin{aligned}
\delta\theta_e &= \frac{2n}{n^2-1}V_{\text{exch}}^{\text{D-I}}\text{Im}\{S_e\} [n_I^{+1} - n_I^{-1} + n_I^{+2} - n_I^{-2}] \\
\delta\theta_h &= \frac{2n}{n^2-1}V_{\text{exch}}^{\text{D-I}}\text{Im}\{S_h\} [n_I^{+1} - n_I^{-1} - n_I^{+2} + n_I^{-2}] \\
\delta R_e &= \frac{4n(1-n)}{(n+1)^3}V_{\text{exch}}^{\text{D-I}}\text{Re}\{S_e\} \sum_s n_I^s \\
\delta R_h &= \frac{4n(1-n)}{(n+1)^3}V_{\text{exch}}^{\text{D-I}}\text{Re}\{S_h\} \sum_s n_I^s \quad (2.22)
\end{aligned}$$

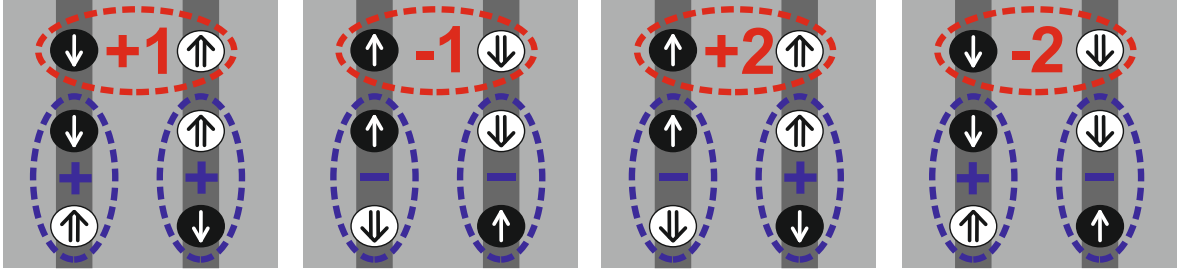


Figure 2.3: All possible carrier exchange interactions between IXs and bright DXs. IX consists of electron in the left(e) QW and hole in the right(h) QW, while electron and hole in one QW form DX. Bright IXs interact with DXs with the same spin in both QWs, while DXs interacting with dark IXs have different spin projection signs in left and right QWs.

where $s = -2, -1, +1, +2$ numerates the IX spin projections and the complex values between the braces are defined by:

$$S_{e(h)}(\omega) = e^{2ikl} \frac{\partial r_{\text{QW}}}{\partial E_{e(h)}} \quad (2.23)$$

The numerical application of these formula for IXs densities $\sim 10^{10} \text{ cm}^{-2}$, $d \sim 10 \text{ nm}$ and 100 % spin polarization of IXs, gives for both the photoinduced differential reflectivity and Kerr rotation angle the values of the order of 10^{-2} . This allows predicting a measurable nonlinear signal in the differential reflectivity and Kerr rotation even for weakly spin polarized IXs. Moreover, the measurement of Kerr rotation at both DX resonances, E_e and E_h , allows the determination of spin polarization degree of dark and bright IX separately: The above relations allow expressing the concentrations of spin-polarized dark and bright excitons induced by the pump in normalized values of signals:

$$\begin{aligned} n_I^{+1} - n_I^{-1} &\sim \delta\theta_L + \delta\theta_L, \\ n_I^{+2} - n_I^{-2} &\sim \delta\theta_L - \delta\theta_L, \\ n_I^{+1} + n_I^{-1} + n_I^{+2} + n_I^{-2} &\sim \delta R_L \sim \delta R_R. \end{aligned} \quad (2.24)$$

$$n_I^{+1} - n_I^{-1} \sim \delta\theta_e + \delta\theta_h, \quad n_I^{+2} - n_I^{-2} \sim \delta\theta_e - \delta\theta_h, \quad (2.25)$$

as well as for the determination of the total density of IXs:

$$n_I^{+1} + n_I^{-1} + n_I^{+2} + n_I^{-2} \sim \delta R_e \sim \delta R_h \quad (2.26)$$

On the other hand, measuring the decay times of the signals in pump-probe experiment one can extract the IX lifetime τ_{IX} and the IX-bound electron and hole spin depolarization rate γ_{es} and γ_{hs} :

$$\begin{aligned} \tau_{\text{IX}}^{-1} &= -\frac{\ln(\delta R_e(t))}{t} = -\frac{\ln(\delta R_h(t))}{t} \\ \gamma_{es} &= -\frac{\ln(\delta\theta_e(t))}{t} - \tau_{\text{IX}}^{-1} \\ \gamma_{hs} &= -\frac{\ln(\delta\theta_h(t))}{t} - \tau_{\text{IX}}^{-1}. \end{aligned} \quad (2.27)$$

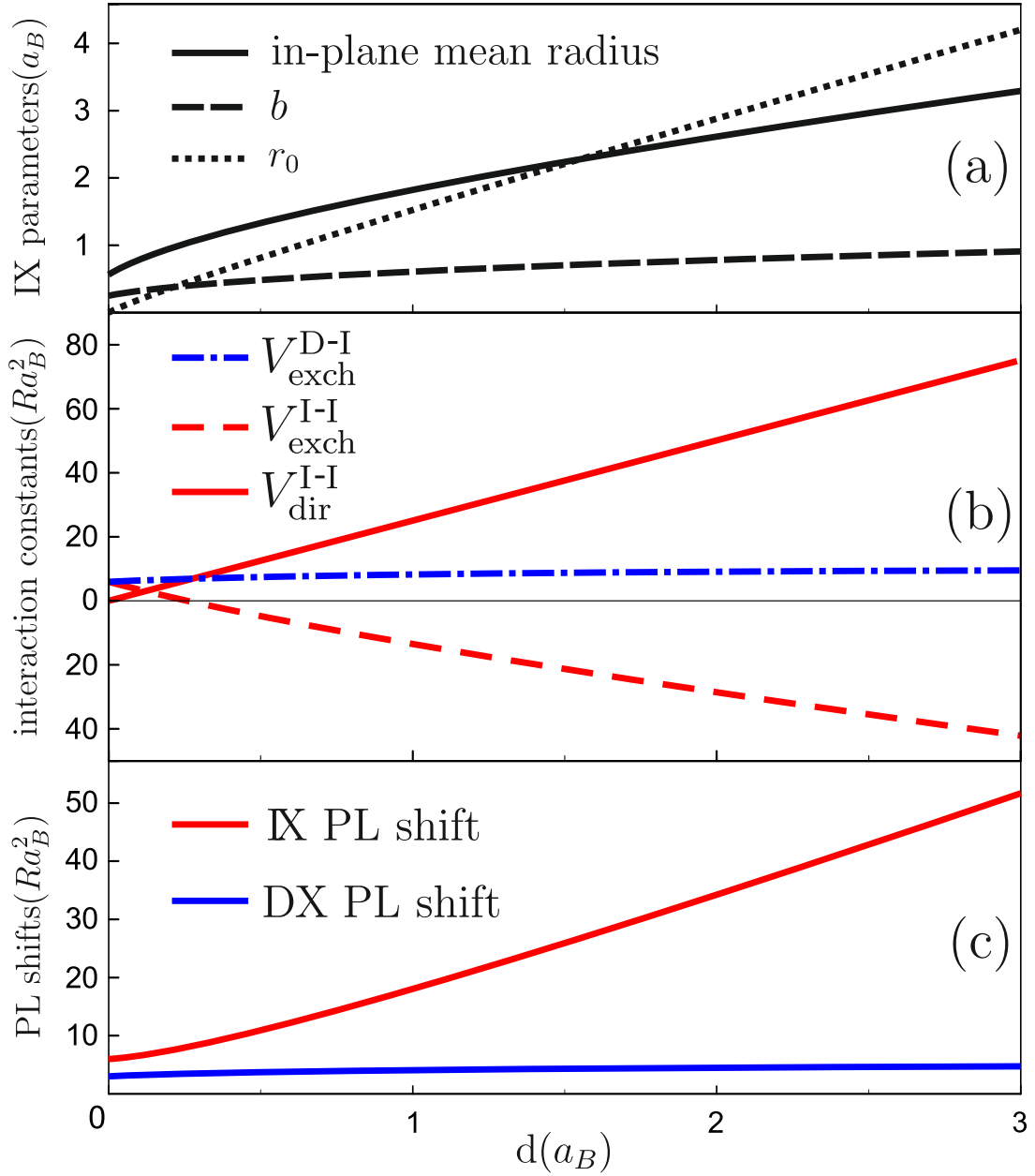


Figure 2.4: (a) Parameters of the IX wave function obtained via variational procedure and the resulting in-plane radius. (b) Interaction constants computed by Monte-Carlo method. DX-IX carrier exchange constant V_{exch}^{D-I} (blue dot-dashed line), IX-IX carrier exchange constant V_{exch}^{I-I} (red dashed line) and direct or exciton exchange interaction constant V_{dir}^{I-I} (red solid line). (c) PL shifts of IX and DX lines calculated from Eqs. 2.21. Units are given in the bulk exciton Rydberg energy R and Bihr radius a_B . From Nalitov et al. (2014) [45].

Note that the determination of the dark IX polarization degree is only possible for the asymmetric CQW structure, where $|E_e - E_h| \gg \Gamma$, and two resonances at direct transitions provide independent signals. In symmetric CQWs $\delta E_e^\pm = \delta E_h^\pm$, which means that only total IXs density and polarization of bright IXs can be determined, while the polarization of dark IXs remains hidden in this case.

IX and DX contributions to the energy shift of the DX transition frequencies are essentially the same (per particle) due to the fact that $V_{\text{exch}}^{I-I} \approx V_{\text{exch}}^{D-I}$ for any realistic distance between the QWs. This allows predicting a strong measurable nonlinear signal in differential reflectivity and Kerr rotation due to IXs. For a strongly polarized excitonic system with a density of the order of 10^{10} cm^{-2} , both the photoinduced differential reflectivity and Kerr rotation angle values are of the order of 10^{-2} in the vicinity of the DX resonance.

In principle, the same effects may be observed at the IX transition frequency, although their magnitude is proportional to the radiative decay Γ_0 entering Eq.(2.1), which decays exponentially for IX resonance with separation of QWs. Indeed, in the IX resonance case, the integrand of Eq.(2.2) describes the vanishing tails of the electron(hole) wavefunction in the hole(electron) QW. Substituting Eq.(2.19) into Eq.(2.7) in a similar manner yields the following expressions:

$$\begin{aligned} \delta\theta_I &= \frac{2n}{n^2 - 1} (V_{\text{dir}}^{I-I} + 2V_{\text{exch}}^{I-I}) \text{Im} \{S_I\} [n_I^{+1} - n_I^{-1}] \\ \delta R_I &= \frac{4n(1-n)}{(n+1)^3} \left(\frac{3}{2} V_{\text{dir}}^{I-I} + V_{\text{exch}}^{I-I} \right) \text{Re} \{S_I\} [n_I^{+1} + n_I^{-1}] + \\ &+ \frac{4n(1-n)}{(n+1)^3} (V_{\text{dir}}^{I-I} + V_{\text{exch}}^{I-I}) \text{Re} \{S_I\} [n_I^{+2} + n_I^{-2}]. \end{aligned} \quad (2.28)$$

where S_I is defined in the same manner as in Eq.(2.23).

Equations (2.22) and (2.28) form a closed non-degenerate system of linear equations on the IXs spin state occupancies n_I^\pm , therefore, the measurements of nonlinear effects on both DX and IX transition frequencies in asymmetric CQWs allow resolving all spin components of IXs system. In particular, bright and dark state populations can be resolved.

The experimental study of the spectra of the nonlinear effects have demonstrated that the mechanism of the spin-dependent exciton energy renormalization dominates in Kerr rotation angle, but does not describe the photoinduced rotation [52]. In terms of the spin-dependent amplitude reflectivity variations δr^\pm for DXs with spin projections $+1$ and -1 this means that the difference between them is smaller than their absolute values: $|\delta r^+ - \delta r^-| \ll |r^\pm|$.

2.1.3 Phase-space filling

Both IXs and DXs are spatially confined in the same CQWs and consist of physically indistinguishable electrons and holes. Consequently, any IX present in the system takes one electron from the valence band and partially fills the conduction band with it, reducing the number of electron states eligible for the direct interband transitions. Although the IX gas cannot empty the valence band and fill up the conduction band completely even at densities close to the Mott transition, it affects the oscillator strength of DX transitions in both QWs and reduces the radiational decay rate Γ_0 . Taking the electron and hole

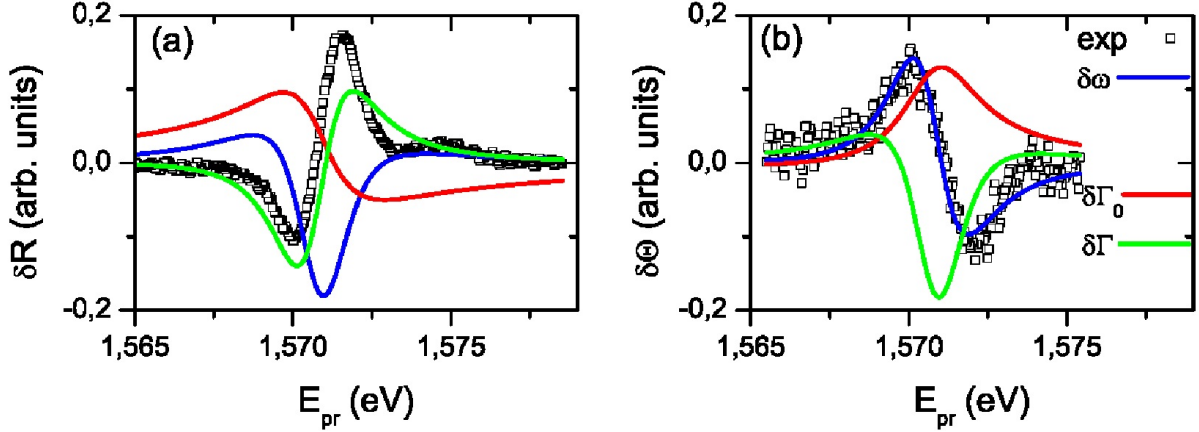


Figure 2.5: Probe spectra of the photoinduced reflectivity (a) and Kerr rotation (b) measured at 5 ns pump-probe delay, and at the direct exciton transition frequency. The direct exciton density at this delay is negligible, and the effect is due to long-living indirect ones. Lines are calculated using Eq.(2.7) assuming photoinduced modification of the DX properties: energy blue shift (blue), saturation (red) and narrowing (green) [17]. The covering layer thickness $l = 200$ nm. The other parameters are chosen to fit both spectra. From Andreakou et al. (2014) [52].

spins into account, one arrives to a spin-dependent reduction of DX decay rate Γ_0^\pm due to the presence of corresponding IX densities n^\pm .

The negative $\delta \Gamma_0^\pm$ entering Eq. (2.4) implies a contribution of this effect to the dynamical amplitude reflectivity coefficient and, consequently, to the nonlinear optical effects: the optically induced reflectivity and Kerr rotation. This contribution has a unique dependence on the probe frequency, which is clearly distinguishable from that of the IX-DX interaction contribution for a given covering layer thickness. This mechanism plays a major role in QW systems with substantial free carrier density, where the trion optical transition becomes important [47]. However, the comparison of the experimental nonlinear optical effect spectra due to IXs in CQWs with the theoretical prediction of the spectrum of this contribution did not demonstrate that this mechanism is dominant [52].

2.1.4 Homogeneous line broadening

The last mechanism of the nonlinear optical effects is related to the variations of the broadening of the optical transition linewidth Γ . Contrary to the energy shift and the phase filling contributions, the sign of $\delta \Gamma^\pm$ in this case is not known *prima facie*. The DX linewidth may be additionally homogeneously broadened due to the Coulomb scattering on IXs [53]. On the other hand, at sufficiently low temperatures IX, spatially localized on the QW disorder potential, may screen and flatten the disorder potential for DXs and therefore decrease the inhomogeneous broadening of the linewidth.

In the simplest approximation, the inhomogeneous broadening is taken into account as an additional imaginary term in the denominator of expression for the amplitude reflectivity (2.1). The total linewidth is then simply defined as a sum of radiative, homogeneous, and inhomogeneous nonradiative broadenings. A more accurate calculation of the re-

flectivity spectra is done via the averaging of the QW dielectric susceptibility [54]. The experimental dynamical photoinduced reflectivity spectra are fitted with the expression (2.7) [52] with a negative $\delta\Gamma^\pm$ when $|\delta\Gamma^\pm| \gg |\delta\Gamma^+ - \Gamma^-|$, implying the dominance of the line narrowing mechanism in the photoinduced reflectivity effect.

2.2 Relaxational spin dynamics of indirect excitons

The nonlinear optical effects described in the previous section are used to study the evolution of the IXs spin systems. On a sufficiently large time scale, the IX gas above the condensation temperature follows a relaxational spin dynamics. The total spin projection of the system on an axis, being a sum of all IXs spin projections, decays due to stochastic processes, like scattering of the excitons on a random potential. As scattering does not affect spin directly, the spin relaxation relies on SOC.

The microscopic mechanisms of exciton spin relaxation due to electron and hole SOC are introduced in Subsection 1. A phenomenological description of the IX spin relaxation based on the Lindblad equation written in terms of exciton spin density matrix is given in Subsection 2. Finally, a model of a nonlinear optical pump-probe experiment revealing the exciton density and the spin relaxation is constructed in Subsection 3.

2.2.1 Exciton gas spin relaxation

The spin relaxation of a two-dimensional exciton gas is mainly caused by the interplay between the SOC and exciton stochastic scattering, either due to dipole-dipole Coulombic repulsion or QW random disorder potential. The electron-hole exchange is suppressed in IXs by the spatial separation, the electron and hole spins are therefore uncoupled and relax independently. This marks the difference between the spatially direct and indirect exciton spin relaxation. The Maille, Andrada e Silva, and Sham mechanism [39], which relies on the electron-hole long-range exchange, is negligible for the latter. The IX spin relaxation is therefore in general slower than that of DX, as this mechanism plays an important role for excitons in QWs.

The IX gas spin relaxational dynamics is described with the Dyakonov-Perel' model [55]. In this representation, the electron and hole spins precess in effective fields Ω_e and Ω_h , attributed to SOC. The direction and the magnitude of this field depend on the exciton wave vector. As the momenta of the exciton ensemble are changing stochastically due to the scattering, the exciton spins are thus precessing in randomly changing effective fields. This process is described with an average free path time τ , during which an exciton keeps its momentum. This time may also be interpreted as the exciton momentum relaxation time, or the transport time. The average exciton electron and hole spin polarizations, which may be induced by circularly polarized optical excitation, decay with time exponentially with effective spin relaxation times τ_e and τ_h . They may be estimated in two opposite limits: $\langle\Omega_{e(h)}\rangle \ll \tau^{-1}$ and $\langle\Omega_{e(h)}\rangle \gg \tau^{-1}$:

$$\tau_{e(h)}^{-1} \approx \begin{cases} \langle\Omega_{e(h)}\rangle^2 \tau, & \langle\Omega_{e(h)}\rangle \ll \tau^{-1} \\ \tau^{-1}, & \langle\Omega_{e(h)}\rangle \gg \tau^{-1} \end{cases} \quad (2.29)$$

Here, the angular brackets denote the averaging of the effective field value over the exciton ensemble. It is defined by the SOC strength. For a conduction band electron it is primarily

determined by the Dresselhaus and Rashba SOC constants. For the valence band the situation is more complicated. The heavy hole energy dispersion branch is split from the light hole branch. However, the two branches anti-cross at large in-plane wave vectors, and the heavy hole strongly couples to the light hole, which strongly affects its spin structure. The exciton-bound hole relaxation time is in most cases shorter than that of the electron [34].

2.2.2 Spin density matrix model

The exponential relaxation of initially prepared spin polarization is commonly described via the Lindblad equation, written in terms of spin density matrix ρ [56, 57, 58]. It represents the quantum Liouville equation with phenomenologically introduced non-Hamiltonian Lindblad term $L(\rho)$:

$$\frac{d\rho}{dt} = -\frac{i}{\hbar} [H, \rho] + L(\rho), \quad (2.30)$$

where H is the Hermitian Hamiltonian of the system, describing all coherent processes.

For excitons, the dimensionality of the reduced spin density matrix ρ corresponds to the number of possible exciton spin projections and equals four. The Hamiltonian H accounts for (i) the Zeeman splittings $2\Delta^{e(h)} = g_{e(h)}\mu_B\mathbf{B}$ of electron(hole) spin states in external magnetic field \mathbf{B} , (ii) the bright-dark energy splitting 2δ and (iii) the splittings between the linearly polarized bright and dark states $2\delta_b$ and $2\delta_d$. In the basis of spin states $(+2 \ +1 \ -1 \ -2)^T$ it reads:

$$H = \begin{pmatrix} -\delta + \Delta_z^e + \Delta_z^h & \Delta_+^e & \Delta_+^h & -\delta_d \\ \Delta_-^e & -\Delta_z^e + \Delta_z^h & -\delta_b & \Delta_-^h \\ \Delta_-^h & -\delta_b & +\Delta_z^e - \Delta_z^h & \Delta_-^e \\ -\delta_d & \Delta_+^h & \Delta_+^e & -\delta - \Delta_z^e - \Delta_z^h \end{pmatrix}, \quad (2.31)$$

where $\Delta_{\pm}^{e(h)} = \Delta_x^{e(h)} \pm i\Delta_y^{e(h)}$.

The phenomenological Lindblad term, accounting for the electron and hole spin relaxation decay rates $\gamma_{e(h)} = 1/2\tau_{e(h)}$ and the recombination rates for bright and dark IXs τ_b and τ_d , is written as:

$$\begin{aligned} L(\rho) = & -\gamma_e [(\rho_{+2,+2} - \rho_{+1,+1})(\delta_{+2,+2} - \delta_{+1,+1}) + (\rho_{-2,-2} - \rho_{-1,-1})(\delta_{-2,-2} - \delta_{-1,-1})] \\ & -\gamma_h [(\rho_{+2,+2} - \rho_{-1,-1})(\delta_{+2,+2} - \delta_{-1,-1}) + (\rho_{-2,-2} - \rho_{+1,+1})(\delta_{-2,-2} - \delta_{+1,+1})] \\ & -\gamma_b [\delta_{+1,+1} + \delta_{-1,-1}] - \gamma_d [\delta_{+2,+2} + \delta_{-2,-2}]. \end{aligned} \quad (2.32)$$

Here $\delta_{i,j}$ is the Kronecker delta symbol. The terms with $\gamma_{e(h)}$ describe relaxation of electron(hole) spin and originate from electron(hole) individual spin flip processes, while that with $\gamma_{b(d)}$ describe simultaneous electron and hole spin flips in bright(dark) excitons due to electron-hole exchange interaction. The nondiagonal spin density matrix terms represent the coherence between the spin states. Their relaxation is described with another characteristic time.

In the following, contrary to the common approach, we neglect coherent effects and concentrate on the Lindblad term in order to describe a pump-probe experiment in CQWs.

Lindblad equation (2.30) is solved either with initial conditions to model a pulsed experiment, or with additional phenomenological source term in the constant excitation case. It is used to model time dependencies of the exciton spin component populations.

2.2.3 Pump-probe experiment model

The spin density matrix formalism may be used to model a proof-of-principle pump-probe nonlinear optical spectroscopy experiment. It is based on the time-resolved measurements of the optically induced reflectivity and Kerr rotation in CQWs. The proposed formalism is similar to the formalism which was developed and successfully applied to QW microcavities in Ref. [59]. In this type of experiment, a short and circularly polarized pump pulse is tuned to a direct exciton resonance and creates DXs with certain spin. The short living DXs either relax into an IX state or recombine, leaving a partially polarized IX system. The linearly polarized probe pulses, also set to the DX transition frequency and weak compared to the pump, act as analyzers of the current exciton density and polarization.

The density matrix formalism is used to model the dynamics of a system containing both DXs and IXs between the arrival of the pump and probe pulses. The system state may be conveniently described by a 16x16 density matrix with elements denoted as $\rho_{e,h,e',h'}^{s,s'}$, where $e, h, e', h' = 0, 1$ indicate the positions of electron and hole (0 or 1 for the electron or hole QW, respectively), $s, s' = -2, -1, +1, +2$ is the exciton spin state. This basis is convenient for the description of the electron and hole tunneling which converts DXs to IXs.

The initial conditions for the density matrix are governed by the pump polarization and frequency. In the considered case of circularly polarized pumping, only diagonal elements of the initial density matrix $\rho_{e,h,e,h}^{s,s}$, with $s = \pm 1$ for σ^\pm pump helicity, are nonzero. Furthermore, if CQWs are asymmetric, DXs in both QWs can be pumped independently, so that only one diagonal component of the initial density matrix is nonzero, $\rho_{0,0,0,0}^{\pm 1, \pm 1}$ if the pump is tuned to the electron QW resonance, or $\rho_{1,1,1,1}^{\pm 1, \pm 1}$ if it is set to the hole QW resonance. In the case of symmetric CQWs, both diagonal components with the same spin are initially nonzero.

The evolution of the density matrix is generally described by a quantum Liouville equation analogous to Eq.(2.30). The Lindblad term in this case accounts for: (i) the tunneling and energy relaxation of electrons from the hole QW to the electron QW and of holes vice versa, described by the rates γ_e and γ_h respectively, (ii) the radiative recombination rate of bright DXs in both QWs $\Gamma_0^e = \Gamma_0^h = \Gamma_0^D$, the one of bright IXs Γ_0^I and corresponding nonradiative recombination rates Γ_{NR}^D and Γ_{NR}^I , (iii) separate spin flips of electrons and holes, described by the spin relaxation rates $\gamma_{e,s}$ and $\gamma_{h,s}$, and the simultaneous electron and hole spin flips, its rate $\gamma_{X,s}$ is defined by electron-hole exchange and is only present for DXs, since this mechanism is suppressed for IXs by the spatial separation of electron and hole [39, 38, 60]. Note that the DX nonradiative recombination rate Γ_{NR}^D does not coincide with the nonradiative broadening Γ of the excitonic resonance, as the latter includes collisions and inhomogeneity contributions with nonradiative recombination. The

Lindblad term reads:

$$\begin{aligned}
L\left(\rho_{e,h,e',h'}^{s,s'}\right) = & \\
& \left[\left(\Gamma_0^D \delta_{e,h} \delta_{e',h'} + \Gamma_0^I \delta_{e,1-h} \delta_{e',1-h'} \right) (\delta_{s,+1} + \delta_{s,-1}) + \Gamma_{\text{NR}}^D \delta_{e,h} \delta_{e',h'} + \Gamma_{\text{NR}}^I \delta_{e,1-h} \delta_{e',1-h'} \right] \delta_{s,s'} \rho_{e,h,e',h'}^{s,s'} \\
& + \gamma_{es} \left[\delta_{s,+1} \delta_{s',+1} \rho_{e,h,e',h'}^{+2,+2} + \delta_{s,+2} \delta_{s',+2} \rho_{e,h,e',h'}^{+1,+1} + \delta_{s,-1} \delta_{s',-1} \rho_{e,h,e',h'}^{-2,-2} + \delta_{s,-2} \delta_{s',-2} \rho_{e,h,e',h'}^{-1,-1} \right] \\
& + \gamma_{hs} \left[\delta_{s,+1} \delta_{s',+1} \rho_{e,h,e',h'}^{-2,-2} + \delta_{s,-2} \delta_{s',-2} \rho_{e,h,e',h'}^{+1,+1} + \delta_{s,-1} \delta_{s',-1} \rho_{e,h,e',h'}^{+2,+2} + \delta_{s,+2} \delta_{s',+2} \rho_{e,h,e',h'}^{-1,-1} \right] \\
& + \delta_{e,h} \gamma_{Xs} \left[\delta_{s,+1} \delta_{s',+1} \rho_{e,h,e',h'}^{-1,-1} + \delta_{s,-1} \delta_{s',-1} \rho_{e,h,e',h'}^{+1,+1} + \delta_{s,+2} \delta_{s',+2} \rho_{e,h,e',h'}^{-2,-2} + \delta_{s,-2} \delta_{s',-2} \rho_{e,h,e',h'}^{+2,+2} \right] \\
& + \gamma_e \delta_{e,0} \delta_{e',0} \rho_{1,h,1,h'}^{s,s'} + \gamma_h \delta_{h,1} \delta_{h',1} \rho_{e,0,e',0}^{s,s'} \tag{2.33}
\end{aligned}$$

Only the lowest-energy IX state, for which $e = 0$ and $h = 1$, is populated in this model via the carrier tunneling and energy relaxation, while the one with $e = 1$ and $h = 0$ remains unpopulated and can be safely ignored. Neglecting the nondiagonal elements of the density matrix, Eq.(2.30) is reduced to a linear matrix differential equation on the 12-component vector of the DX and IX spin states populations $n_e^s = \rho_{0,0,0,0}^{s,s}$, $n_h^s = \rho_{1,1,1,1}^{s,s}$ and $n_I^s = \rho_{0,1,0,1}^{s,s}$:

$$\frac{d}{dt} \begin{pmatrix} n_e^s \\ n_h^s \\ n_I^s \end{pmatrix} = \begin{pmatrix} \widehat{L}_D & 0 & 0 \\ 0 & \widehat{L}_D & 0 \\ \gamma_h \widehat{I} & \gamma_e \widehat{I} & \widehat{L}_I \end{pmatrix} \begin{pmatrix} n_e^s \\ n_h^s \\ n_I^s \end{pmatrix}, \tag{2.34}$$

where \widehat{I} is the 4x4 identity matrix, \widehat{L}_D and \widehat{L}_I describe decay and spin relaxation of DXs and IXs, respectively:

$$\widehat{L}_D = \begin{pmatrix} -\Gamma_{\text{NR}}^D & \gamma_{es} & \gamma_{hs} & \gamma_{Xs} \\ \gamma_{es} & -\Gamma_0^D - \Gamma_{\text{NR}}^D & \gamma_{Xs} & \gamma_{hs} \\ \gamma_{hs} & \gamma_{Xs} & -\Gamma_0^D - \Gamma_{\text{NR}}^D & \gamma_{es} \\ \gamma_{Xs} & \gamma_{hs} & \gamma_{es} & -\Gamma_{\text{NR}}^D \end{pmatrix}, \tag{2.35}$$

$$\widehat{L}_I = \begin{pmatrix} -\Gamma_{\text{NR}}^I & \gamma_{es} & \gamma_{hs} & 0 \\ \gamma_{es} & -\Gamma_0^I - \Gamma_{\text{NR}}^I & 0 & \gamma_{hs} \\ \gamma_{hs} & 0 & -\Gamma_0^I - \Gamma_{\text{NR}}^I & \gamma_{es} \\ 0 & \gamma_{hs} & \gamma_{es} & -\Gamma_{\text{NR}}^I \end{pmatrix} \tag{2.36}$$

The solution of Eq.(2.34) can be expressed using a matrix exponent:

$$\begin{pmatrix} n_e^s & n_h^s & n_I^s \end{pmatrix}^T = \begin{pmatrix} n_e^s & n_h^s & n_I^s \end{pmatrix}^T \Big|_{t=0} \exp(t\widehat{M}), \tag{2.37}$$

where \widehat{M} is the 12x12 relaxation matrix given explicitly in the right part of (2.34).

The solution (2.37) may be analyzed in the region of time $t \gg (\Gamma_{\text{NR}}^D)^{-1}$, when all DXs have vanished and the time evolution is reduced to a 4x4 equation on IX spin component densities:

$$\frac{\partial}{\partial t} (n_I^{+2}, n_I^{+1}, n_I^{-1}, n_I^{-2})^T = \widehat{L}_I (n_I^{+2}, n_I^{+1}, n_I^{-1}, n_I^{-2})^T. \tag{2.38}$$

The four eigenvalues of \widehat{L}_I read:

$$-\gamma = -\Gamma_{\text{NR}}^I - \frac{\Gamma_0^I}{2} - \gamma_{es} - \gamma_{hs} \pm \sqrt{\left(\frac{\Gamma_0^I}{2}\right)^2 + (\gamma_{es} \pm \gamma_{hs})^2} \tag{2.39}$$

and correspond to characteristic decay rates of IX system, which in principle may be extracted from the time dependences of measured nonlinear signals. Those of the rates faster than DX decay Γ_{NR}^D , however, are not relevant in the considered regime. Realistically, the slowest decay rate, which fully describes the system relaxation at long times, reads:

$$\gamma_0 = \Gamma_{\text{NR}}^I + \frac{\Gamma_0^I}{2} + \gamma_{es} + \gamma_{hs} - \sqrt{\left(\frac{\Gamma_0^I}{2}\right)^2 + (\gamma_{es} + \gamma_{hs})^2}. \quad (2.40)$$

In the limits $\gamma_{es} + \gamma_{hs} \gg \Gamma_0^I$ and $\gamma_{es} + \gamma_{hs} \ll \Gamma_0^I$ it may be further simplified:

$$\gamma_0 \approx \Gamma_{\text{NR}}^I + \min(\Gamma_0^I/2, \gamma_{es} + \gamma_{hs}). \quad (2.41)$$

The model formulated above neglects several non-linear effects which may become important in realistic structures. In particular, it neglects all possible nonlinearities in the Lindblad superoperator, which may come from the effective exchange field arising in a circularly polarized dense exciton system, the decrease of DX radiative decay rate with increase of the exciton density, supplementary decoherence mechanism due to the collisional broadening of the exciton states, which is sensitive to the exciton density, pair scattering and resulting conversion of bright to dark excitons and vice versa [61]. Its purpose is to show on a simplest example how the Kerr rotation and differential reflection measured at the DX frequency can be used to obtain information on the population and polarization of bright and dark IX states.

Substituting different initial conditions into Eq.(2.37), one can address various experimental scenarios. In the numerical analyses we focus on three important cases: (i) DXs in both symmetric QWs are pumped simultaneously, (ii) CQWs are asymmetric, and we excite selectively DXs in the electron QW, in which case IXs are formed due to the hole tunneling, (iii) CQWs are asymmetric, and we excite selectively DXs in the hole QW, so that IXs are formed due to the electron tunneling. The cases (ii) and (iii) will be referred to as "electron QW pumping" and "hole QW pumping", respectively, to emphasize that in the case (ii) we optically create electrons in the same well where the electrons of the lowest energy IXs are, while in the case (iii) we excite holes in the same well where the holes of the lowest energy IXs stay.

Figures 2.6(a,b,c) show the populations of bright and dark DX and IX states as functions of time in the cases (i,ii,iii), respectively. In all cases, the main features of IX and DX population dynamics are the same: the IXs population initially increases, while the DX population shows a fast decay due to the tunneling of electrons (ii), holes (iii), or both (i), and due to the radiative recombination of DXs. At longer times, the IX population slowly decreases. The bright and dark exciton populations quickly equalize due to the hole spin relaxation. Note that the maximum amount of IXs left after the decay of DXs depends on the rate of conversion from DXs to IXs, which is different for listed cases. The conversion due to the electron tunneling is faster than one due to the hole tunneling because of the lighter electron effective mass with respect to the heavy hole (in the structure growth direction). Figure 2.6(d) shows the dynamics of polarization degrees of bright DXs and IXs which is the same for all considered cases. The DX polarization induced by light quickly decays due to the $\gamma_{X,s}$ relaxation term describing the simultaneous electron and hole spin-flips. IX polarization lives much longer, as for IXs this term is inhibited. Interestingly, the fast depolarization of holes does not lead to the decay of

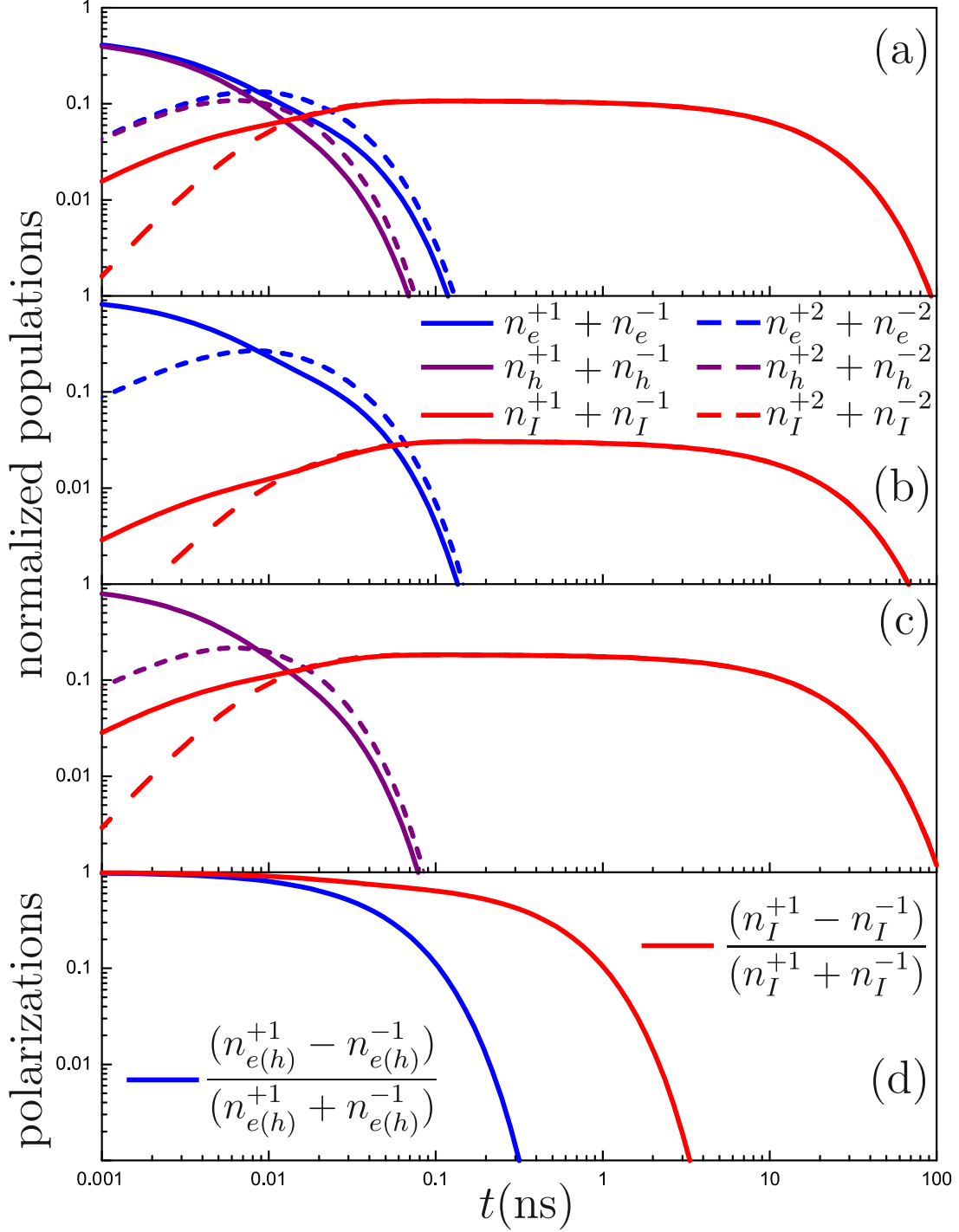


Figure 2.6: Exciton relaxation dynamics in CQWs after a short circularly polarized pump pulse: (a) the normalised exciton populations in equally pumped symmetric CQWs; (b) the same for the pumping of an "electron" QW in asymmetric CQWs; (c) the same for the pumping of a "hole" QW in asymmetric CQWs; (d) DX and IX bright exciton polarization degrees. For all panels solid and dashed curves correspond to bright and dark states, respectively, blue and purple curves are related to DXs in electron and hole QWs, while red curves describe IXs. The parameters used in this calculation: $\gamma_h = (300 \text{ ps})^{-1}$, $\gamma_e = (30 \text{ ps})^{-1}$, $\Gamma_{\text{NR}}^D \ll \Gamma_0^D = (100 \text{ ps})^{-1}$, $\Gamma_{\text{NR}}^I \ll \Gamma_0^I = (10 \text{ ns})^{-1}$ [62], $\gamma_{es} = (1 \text{ ns})^{-1}$, $\gamma_{hs} = (10 \text{ ps})^{-1}$, $\gamma_{Xs} = (50 \text{ ps})^{-1}$ [39]. From Nalitov et al. (2014) [45].

polarization degree of either bright or dark excitons. Indeed, the transformations from $+1(+2)$ to $-1(-2)$ spin states or vice versa require both electron and hole spin flips. Fast hole spin flips, however, do lock bright and dark excitons polarization degrees to the same absolute values and different signs, which is why we only plot bright excitons polarization. The simulations presented in Figure 4 neglect the nonradiative recombination of excitons. This approximation is well justified for high quality CQW structures, where the nonradiative recombination rate is much lower than the radiative recombination rate [63]. We note also, that the re-polarization of DXs due to the effective Zeeman splitting induced by polarized IXs is negligibly small in the chosen range of parameters.

Figure 2.2.3 shows the differential reflectivities and Kerr rotation angles obtained for asymmetric (a,b) and symmetric (c) CQWs. These quantities are obtained using Eqs.(2.22) for the IXs contributions and the following expressions for the DXs contributions obtained within the same assumptions as in the Section III:

$$\begin{aligned}\delta\theta_{e(h)} &= \frac{4n}{n^2 - 1} V_{\text{exch}}^{\text{D-D}} \text{Im} \{S_{e(h)}\} \left[n_{e(h)}^{+1} - n_{e(h)}^{-1} \right] \\ \delta R_{e(h)} &= \frac{8n(1-n)}{(n+1)^3} V_{\text{exch}}^{\text{D-D}} \text{Re} \{S_{e(h)}\} \sum_s n_{e(h)}^s,\end{aligned}\quad (2.42)$$

where $V_{\text{exch}}^{\text{D-D}} = V_{\text{exch}}^{\text{I-D}}(d=0) = V_{\text{exch}}^{\text{I-I}}(d=0)$ are the exchange interaction constants calculated in [49]. In the present calculation, we have assumed equality of the interaction constants $V_{\text{exch}}^{\text{D-D}} = V_{\text{exch}}^{\text{I-D}}$, which is reasonable due to the weak dependence of $V_{\text{exch}}^{\text{I-D}}$ on the distance between the QWs d (see Fig. (2.4)). One can see that the Kerr rotation signal decays faster than the differential reflectivity signal, in general. This is not surprising as the Kerr effect is sensitive not only to the population of IXs but also to their spin polarization, which decays faster than population. There are two time-scales in the Kerr signal corresponding to the hole and electron spin relaxation times. In the case of asymmetric CQWs both reflectivity and Kerr signals are initially much stronger at the exciton resonance in the pumped QW, while at the characteristic time-scale of the tunneling transfer the reflectivity signals from both wells become comparable. The Kerr signal is always stronger in the electron QW than in the hole QW as the electron spin relaxation time is much longer than the hole spin relaxation time. The dynamics of Kerr rotation and differential reflectivity gives a direct access to DX and IX spin relaxation and recombination times, but also to the electron and hole spin relaxation and tunneling times.

The calculated nonlinear optical signals may be compared with experimental Figure 2.8, showing optically induced reflectivity and Kerr rotation spectra as a function of the delay between pump and probe pulses. They demonstrate a short initial decay of both types of signals, attributed to DXs, and a transition to a long slow density and spin relaxation phase, corresponding to the phase where only IXs are left. In the absence of applied electric bias, both spin and density relaxation times are much shorter, as the ground exciton state is spatially direct. This demonstrates that the presence of IX is evidenced in both photoinduced reflectivity and Kerr rotation effects, measured at the DX transition frequency.

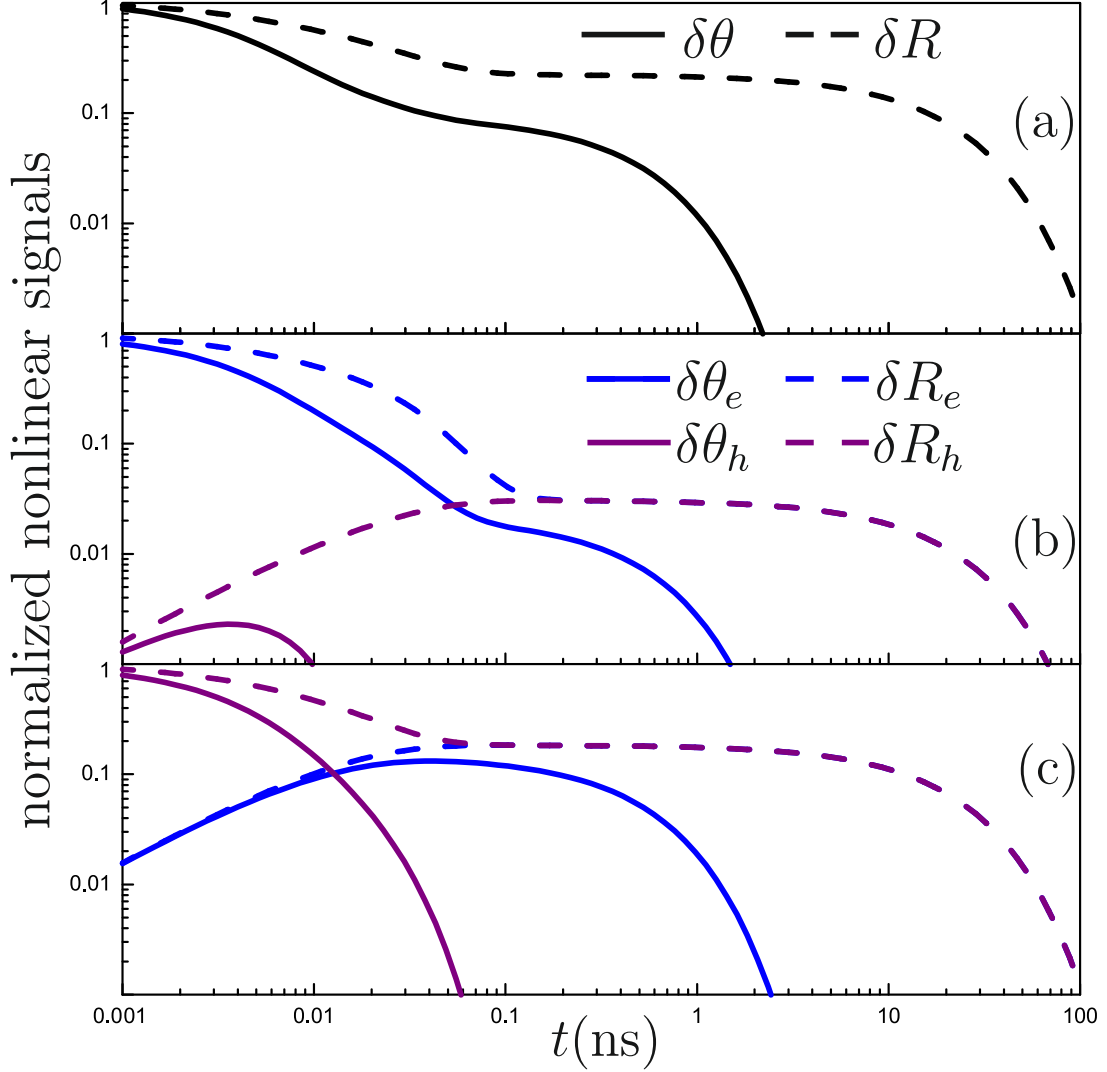


Figure 2.7: Calculated dynamics of the photoinduced reflectivity (dashed curves) and Kerr rotation (solid curves) signals in CQWs after a short circularly polarized pump: (a) symmetric CQWs, both QWs are pumped (b) asymmetric CQWs, electron QW pumping (c) asymmetric CQWs, hole QW pumping. Blue and purple lines describe signals on electron and hole QWs resonant frequencies respectively, black curves describe folded signals from both symmetric CQWs. Parameters of calculation are the same as in Figure 2.6. From Nalitov et al. (2014) [45].

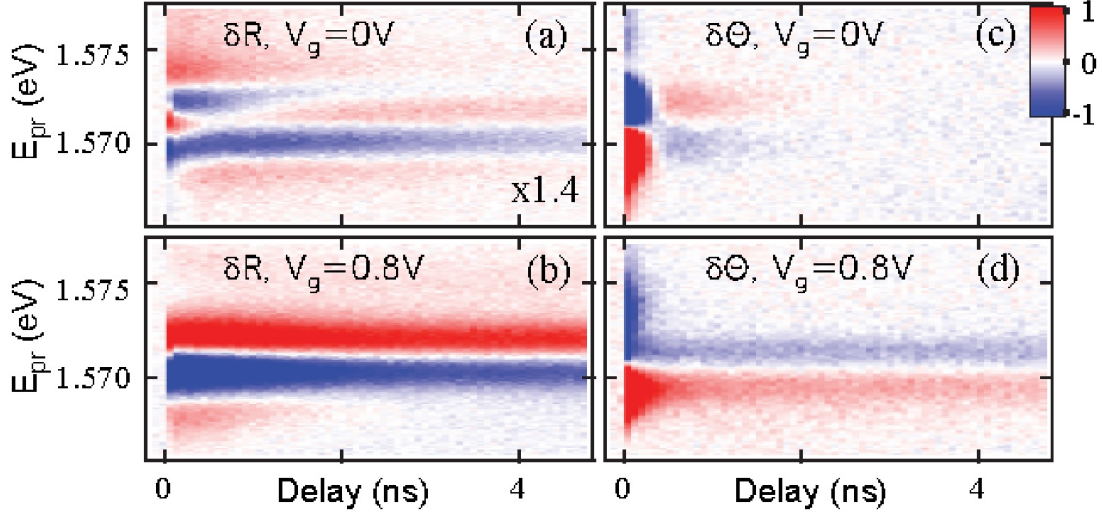


Figure 2.8: Reflectivity (a, b) and Kerr rotation (c, d) induced by pump pulses resonant with DX transition ($E_{pp} = 1.568$ eV), measured as a function of the pump-probe delay and probe energy in absence of applied bias (a, c) and at voltage 0.8 V (b, d). From Andreakou et al. (2014) [52].

2.3 Coherent spin dynamics of indirect excitons

Apart from the relaxational dynamics, an IX system in some cases may be described in terms of wavefunction and coherent wave equations of Schroedinger type. An example of such a system is an IX condensate, where the effect of interest is linear in exciton density and interactions therefore may be neglected in the Gross-Pitaevskii equation. In general, a ballistically propagating or expanding cloud of IXs is coherent on scales below the mean free path or the mean collision time, and obeys the wave equations.

To take into account the spin-orbit interaction, naturally present in zinc-blende symmetry CQWs and introduced in Subsection 1.2.2, the Schroedinger equation must be generalized to quasi-particles with spin. Excitons, having four possible spin projections on CQWs growth axis, are described with bispinor, or four-component wavefunction. The coherent wave equation on this bispinor is introduced in Subsection 1. Diagonalization of the Hamiltonian, entering this equation and defining the bispinor evolution, results in four branches of IX energy dispersion.

The ground state energy dispersion branch has an axial symmetry and a peculiar minimum at nonzero wavevector, which implies radial expansion of a IX system initially created at zero wavevector even in absence of interparticle repulsion. It is described in Subsection 2.

The solutions of the wave equation depending on the boundary conditions may have topologically nontrivial spin configurations of the skyrmion type, which is obtained in Subsection 3.

2.3.1 Bispinor evolution equation

Experimental results, recently obtained in Ref. [17], suggest that a coherent wave equation description may be used for their interpretation. They can be summarized as follows. Faraway from the local pumping area, the strong maxima in the bright exciton distribution are observed. They were attributed to complex processes of carrier diffusion. These localized bright spots (LBS) were found to generate a radial outward flow of bright excitons characterized by: 1) a spatial coherence, with a coherence length of the order of 10 microns; 2) a specific linear polarization pattern over the same length scale; and 3) the presence of phase singularities. This specific linear polarization pattern has been attributed to the radial cloud expansion from localized sources (See supplemental material of Ref.[17]). The wave vector distribution of the electron and the hole wavefunctions forming the excitonic wave packet was neglected. This approach allowed to reproduce the polarization pattern, but not the presence of phase singularities observed.

A different and more complete approach, allowing to qualitatively reproduce all the experimental features, may be used. First, the internal structure of excitons is taken into account to obtain comparable Dresselhaus spin-orbit interaction contributions coming from the electron and the hole composing the exciton. Second, a bright IX condensate with a well defined spin state is assumed to be locally formed at the center of the LBS, analogously to Ref.[17]. Then, unlike the approach of Ref.[17], coherent expansion of the resonantly created exciton cloud may be obtained by direct numerical solution of the Schroedinger equation, in the presence of the Dresselhaus SOC. The renormalization of the dispersion induces a radial flow of excitons outwards from the pump spot. The repulsive exciton-exciton interactions can also contribute to this effect, but may be neglected. Since the typical time scale of IXs scattering on phonons is of the order of a few ns [64], the ballistic propagation length is expected to be of the order of 10-20 microns. Within this length scale, we reproduce both the polarization pattern, and the presence of phase singularities of the wave function components, which are associated with the formation of skyrmions. These topological defects appear thanks to the interplay between the radial flow and the SOC, as recently shown theoretically [65] for cavity polaritons flowing in a TE-TM effective magnetic field. Inspired by the experimental results, we propose a configuration leading to the onset of circular polarization domains, fully equivalent to the one observed in the optical spin Hall effect[25]. This happens despite the fact that the wavevector dependence of the effective magnetic field of the Dresselhaus SOC is completely different from the one given by the TE-TM splitting in the microcavities.

As discussed in Subsection 1.2.2, for a gas of free 2D electrons, Dresselhaus SOC is linear versus the electron wave-vector and the corresponding term of the Hamiltonian in the basis $(+1/2, -1/2)^T$ takes the form:

$$H_e^D = \tilde{\beta}_e(\sigma_+ k_-^e + \sigma_- k_+^e), \quad (2.43)$$

where $\tilde{\beta}_e$ is a Dresselhaus interaction constant. Here and after, the following notations are used: $k_\pm^\gamma = k_x^\gamma \pm ik_y^\gamma$, $k_{x,y}^\gamma$ are x - and y -components of wave-vector k^γ , and $\gamma = e, h$ or X for electrons, holes or excitons respectively. $\sigma_\pm = \sigma_x \pm i\sigma_y$ when $\sigma_{x,y}$ are Pauli matrices.

For free heavy holes in 2D, the SOC terms of the same form and order as for electrons (2.43), but in the basis of spin states $(+3/2, -3/2)^T$, may be obtained either through averaging of cubic-in- k SOC terms over internal electron-hole motion, or directly from

multiple band $k \cdot p$ model [15, 16]. One may therefore write a common SOC term for both electron and hole bound into exciton as:

$$H_{e,h}^D = \beta_{e,h} \nu_{e,h} (\sigma_+ k_-^X + \sigma_- k_+^X). \quad (2.44)$$

Here $\beta_{e,h}$ are the effective Dresselhaus interaction constants of electrons and holes.

In addition to the SOC, a k -independent energy splitting between linearly polarized states, e.g. parallel and perpendicular to crystallographic axis, can occur and can be described as a k -independent effective magnetic field. Finally, we can write the Hamiltonian for IXs on the basis of the four spin states $(+2, +1, -1, -2)^T$ as follows:

$$H(\mathbf{k}^X) = \begin{pmatrix} E_{+2}(k^X) & \nu_e \beta_e k_+^X & \nu_h \beta_h k_-^X & -\delta_d \\ \nu_e \beta_e k_-^X & E_{+1}(k^X) & -\delta_b & \nu_h \beta_h k_-^X \\ \nu_h \beta_h k_+^X & -\delta_b & E_{-1}(k^X) & \nu_e \beta_e k_+^X \\ -\delta_d & \nu_h \beta_h k_+^X & \nu_e \beta_e k_-^X & E_{-2}(k^X) \end{pmatrix} \quad (2.45)$$

Here $E_{\pm 1, \pm 2}(k) = E_0(k) = \hbar^2(k^X)^2/2m_X$ are the parabolic dispersions of the bare IX states, $\delta_{b,d}$ give the energy splittings between linearly polarized bright (dark) states. We take the exciton energy at $k^X = 0$ as the zero point and put $\delta_b = \delta_d = 0$.

Introducing a phenomenological IX decay term, one may write the evolution equation on the bispinor $(\Psi_{+2}, \Psi_{+1}, \Psi_{-1}, \Psi_{-2})^T$ in the momentum representation with the Hamiltonian (2.45):

$$\frac{\partial}{\partial t} \begin{pmatrix} \Psi_{+2}(\mathbf{k}^X) \\ \Psi_{+1}(\mathbf{k}^X) \\ \Psi_{-1}(\mathbf{k}^X) \\ \Psi_{-2}(\mathbf{k}^X) \end{pmatrix} = -\frac{i}{\hbar} H(\mathbf{k}^X) \begin{pmatrix} \Psi_{+2}(\mathbf{k}^X) \\ \Psi_{+1}(\mathbf{k}^X) \\ \Psi_{-1}(\mathbf{k}^X) \\ \Psi_{-2}(\mathbf{k}^X) \end{pmatrix} - \frac{1}{2\tau(k^X)} \begin{pmatrix} 0 \\ \Psi_{+1} \\ \Psi_{-1} \\ 0 \end{pmatrix}, \quad (2.46)$$

where $\tau(k^X)$ is the wave vector dependent radiational recombination time, tending to infinity outside the light cone, and nonradiational decay is neglected. The evolution equation (2.46) may be solved under boundary conditions either with the source term in the case of constant pumping, or with initial conditions set by an excitation pulse.

2.3.2 The minimum of the energy dispersion

Diagonalization of the effective Hamiltonian (2.45) is trivial and results in four branches of energy dispersion, plotted in Fig. 2.9:

$$\begin{pmatrix} E_I(k^X) \\ E_{II}(k^X) \\ E_{III}(k^X) \\ E_{IV}(k^X) \end{pmatrix} = \begin{pmatrix} E_0(k^X) + (\nu_h \beta_h + \nu_e \beta_e) k^X \\ E_0(k^X) + (\nu_h \beta_h - \nu_e \beta_e) k^X \\ E_0(k^X) - (\nu_h \beta_h - \nu_e \beta_e) k^X \\ E_0(k^X) - (\nu_h \beta_h + \nu_e \beta_e) k^X \end{pmatrix} \quad (2.47)$$

with corresponding eigenstates:

$$\psi_I = \begin{pmatrix} 1 \\ +e^{-i\phi} \\ +e^{+i\phi} \\ 1 \end{pmatrix}, \psi_{II} = \begin{pmatrix} -1 \\ +e^{-i\phi} \\ -e^{+i\phi} \\ 1 \end{pmatrix}, \psi_{III} = \begin{pmatrix} -1 \\ -e^{-i\phi} \\ +e^{+i\phi} \\ 1 \end{pmatrix}, \psi_{IV} = \begin{pmatrix} 1 \\ -e^{-i\phi} \\ -e^{+i\phi} \\ 1 \end{pmatrix} \quad (2.48)$$

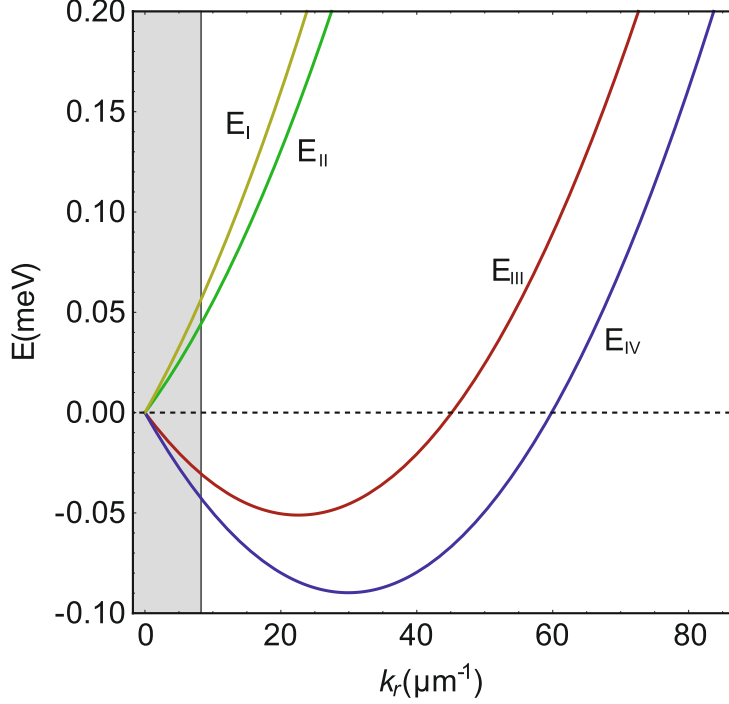


Figure 2.9: Isotropic dispersion branches of the indirect exciton eigen modes [see Eqs.(2.47)]. Gray area marks the light cone. From Vishnevsky et al. (2013) [66].

Here ϕ is the polar angle in reciprocal space.

The two lower branches of the energy dispersion have their minima at nonzero wave vector. This implies that a resonantly prepared IX system with zero momentum, be that a cold exciton gas or a condensate, is unstable with respect to relaxation. This stands, in particular, for the case of optical excitation, when excitons are created with small wave vectors within the light cone. Such an IX system starts expanding due to the effect of the SOC, even when the repulsion between the excitons is weak.

If the exciton ground state wave vector lays outside of the light cone, light emission from the ground state is forbidden due to energy-momentum conservation rather than total angular momentum conservation. In this case, a condensate eventually relaxes to a "dark" state and only emits light when it is scattered on the disorder.

The combinations of Eqs(2.48) correspond to "linear polarizations" for the bright (rows 2 and 3) part given the usual identities $\psi_{\pm} = \psi_X \pm i\psi_Y$. While the dark components are isotropic, the bright components have a linear polarization that is ϕ -dependent and the polarization changes from X to Y when ϕ is changed by $\pi/2$. This peculiarity is analogue to the exciton-polariton case in the presence of the so-called TE-TM splitting that gives birth to the optical spin Hall effect [65, 25, 26, 67]. One can therefore expect the formation of the same polarization pattern from the bright exciton states under proper excitation.

2.3.3 Topologically nontrivial spin configurations

Depending on the boundary conditions or on the exact type of the source term, equation (2.46) yields different polarization and IX density textures. In particular, spin configurations with nontrivial topology, that cannot be transformed to a trivial ones continuously, may emerge. Among these nontrivial configurations the most famous are the topological defects. The examples of such configurations are vortices and half-vortices, studied in cavity polariton condensates [68, 69]. The difference between an integer vortex in a spinor condensate and a half-vortex in the same condensate is that the latter is a topological defect in one spin component of a polariton condensate, while the first one is a couple of half-vortices in both spin components, characterized by a point in real space with zero total density. Another significant property of a quantized vortex in the indetermined phase in its center accompanied with a nonzero phase, gained in a full circumrotation around it in real space. They appear in experimental phase maps as fork-like dislocations.

Quantized vortices, however, do not exhaust all possible nontrivial spin configurations of an IX condensate. An example of topologically nontrivial spin configuration is the skyrmion. By definition it is a topologically nontrivial multicomponent wavefunction with constant total density. Similarly to vortices, it is characterized by pseudospin winding around the core with undefined phase. It may be realized if a density dip in one spin component, which creates phase uncertainty, is compensated in the others, so that that the total density remains constant. Unlike vortices and half-vortices, skyrmions in a IX system can not be seen on the total emission intensity maps, but appear as phase dislocation in phase maps.

In the idealized case of a Dirac delta source in real space, the excitation of an eigenstate can be found analytically. For example, the dynamical equation for the first component $\psi_I(k^X)$ of the full bispinor in the basis of spin states, given by (2.48), reads:

$$i\hbar \frac{\partial \psi_I(\mathbf{k}^X, t)}{\partial t} = \frac{\hbar^2}{2m} (k^X)^2 \psi_I(\mathbf{k}^X, t) + i\Delta\beta k^X \psi_I(\mathbf{k}^X, t) + A_P e^{i\omega_P t}. \quad (2.49)$$

Here \mathbf{k}^X is a two-dimensional in-plane wave vector, and A_P is the corresponding first component of the source term in the same spin basis (2.48).

and the stationary radial solutions are found writing $\psi_I(k_r^X, t) = \psi_I(k_r^X) \exp(i\omega_P t)$ which yields:

$$\hbar\omega_P \psi_I(k_r^X) = \left(\frac{\hbar^2}{2m} (k_r^X)^2 + i\Delta\beta k_r^X \right) \psi_I(k_r^X) + A_P \quad (2.50)$$

the Green's function of the problem reads

$$G_I(k^X) = -\frac{A_P}{\frac{\hbar^2}{2m} (k_r^X)^2 + i\Delta\beta k_r^X - \hbar\omega_P} \quad (2.51)$$

whose Fourier transform gives

$$G_I(r) = \frac{A_P \kappa_1}{\kappa_2 - \kappa_1} \left[\begin{array}{l} \log\left(\frac{2}{\kappa_1}\right) \frac{J_0(\kappa_1 r)}{2} - \frac{\pi}{2} \mathbf{H}_0(\kappa_1 r) \\ + {}_0F_1\left(1, -\frac{\kappa_1^2 r^2}{4}\right) \end{array} \right] \quad (2.52)$$

$$- \frac{A_P \kappa_2}{\kappa_2 - \kappa_1} \left[\begin{array}{l} \log\left(\frac{2}{\kappa_2}\right) \frac{J_0(\kappa_2 r)}{2} - \frac{\pi}{2} \mathbf{H}_0(\kappa_2 r) \\ + {}_0F_1\left(1, -\frac{\kappa_2^2 r^2}{4}\right) \end{array} \right] \quad (2.53)$$

which is nothing but $\psi_I(r)$ for the delta source. Here $J_0(\kappa r)$, $\mathbf{H}_0(\kappa r)$ and ${}_0F_1(1, -\kappa^2 r^2/4)$ are the Bessel, the Struve and the Generalized Hypergeometric functions respectively, $\kappa_{1,2}$ are the poles of Eq.(2.51) and Eqs.(2.52,2.53) require that $\kappa_1 > 0$ and $\kappa_2 < 0$ which means that $\hbar\omega_P > 0$. The solutions for the other eigenstates are found with a similar procedure and one can therefore construct any combination using the eigenstates (2.48).

For a numerical simulation, a linearly polarized ($P_{\pm 2} = 0, P_{\pm 1} \neq 0$) bright exciton state is chosen as the initial condition. Here and after, the Dresselhaus constants for electrons and holes $\beta_{e,h} = 6\mu eV \cdot \mu m$, and the masses $m_e = 0.07m_0, m_h = 0.5m_0$, where m_0 is the free electron mass. Figs. 2.10 (a,b,c) shows the stationary real space images of linear and circular polarization degrees and the phase of the bright states. One can observe the formation of a skyrmion lattice associated with the formation of the spin domains. The situation is analogous with the polaritonic spin Hall effect recently analyzed theoretically [65]. This similarity is expectable, since the effective field acting on the bright states is exactly equivalent to the case of exciton polaritons in the presence of the so-called TE-TM splitting. Fig. 2.10 (c) shows the density profile of bright states along the diagonal line (white dashed line on Fig. 2.10 (b)). Densities of σ^+ and σ^- states are oscillating while the total density decays in space with r . Phase structure of σ^+ -polarized bright state is plotted on Fig. 2.10 (d). However, the linear polarization pattern that we observe has 8 polarization domains and differs from the one measured in [17], which has 4 domains.

In order to reproduce the experimental picture, a different initial spin state for the condensate is chosen (Fig. 2.11). First, a condensate of dark states with a slight asymmetry between dark components is considered ($P_{-2}/P_{+2} = 0.9, P_{+1} = P_{-1} = 0$). Then, in order to mix the circularly polarized bright states, an additional constant splitting between the linearly polarized bright states along and perpendicular to the main crystallographic axis of the sample is introduced $\delta_b = 1\mu eV$.

Fig. 2.11 (a,b) shows the spatial distribution of linear and circular polarization degree, while Fig.2.11(d) shows the phase of the X -component. Both circular and linear polarization structures present 4 domains and are stretched along the x axis (because of δ_b) as it was observed in experiment [17]. Interestingly, we also observe pairs of phase singularities (red crosses), situated symmetrically with respect to the exciton source. This phase singularity is accompanied by a density dip only in the Y component. This topological defect is therefore similar to a skyrmion but in the linear polarization basis. Contrary to conventional skyrmion, for instance, in magnetic systems with Dzyaloshinskii-Moriya interactions, its existence is provided by SOC rather than interparticle interactions. On the contrary, the field configurations of this type are not stable with respect to nonlinear effects [65]. Our approach shows that the appearance of phase singularities is a general feature of radial flows of particles in the presence of coupling between the spin and motional degree of freedom.

2.4 Conclusion

The present chapter mainly gives an overview of our two recent theoretical works in the field of spatially indirect excitons in coupled quantum wells [45, 66].

The first one examines the possibility of applying nonlinear optical experimental techniques for the study of these quasiparticles. We demonstrated that despite their vanishing

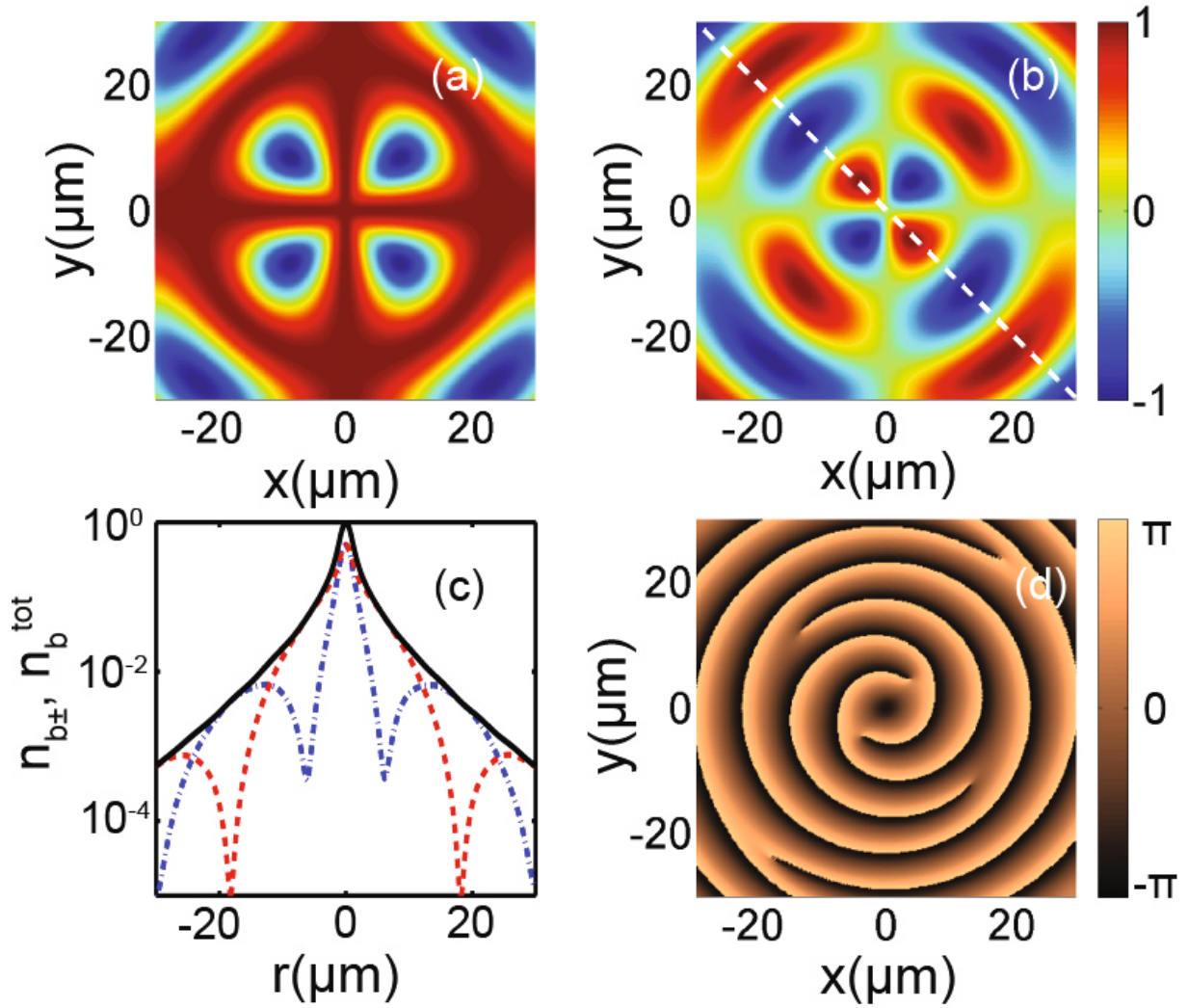


Figure 2.10: (Color online) (a) Degree of linear polarization of bright states. (b) Degree of circular polarization of bright states. (c) Density profile for σ^+ - (n_{b+} , red dashed line), σ^- - (n_{b-} , blue dashed line) polarized bright states and total density (n_b^{tot} , black solid line) of bright states along the diagonal line $y = -x$ (white dashed line in (b)). (d) Phase of σ^+ -polarized bright component. From Vishnevsky et al. (2013) [66].

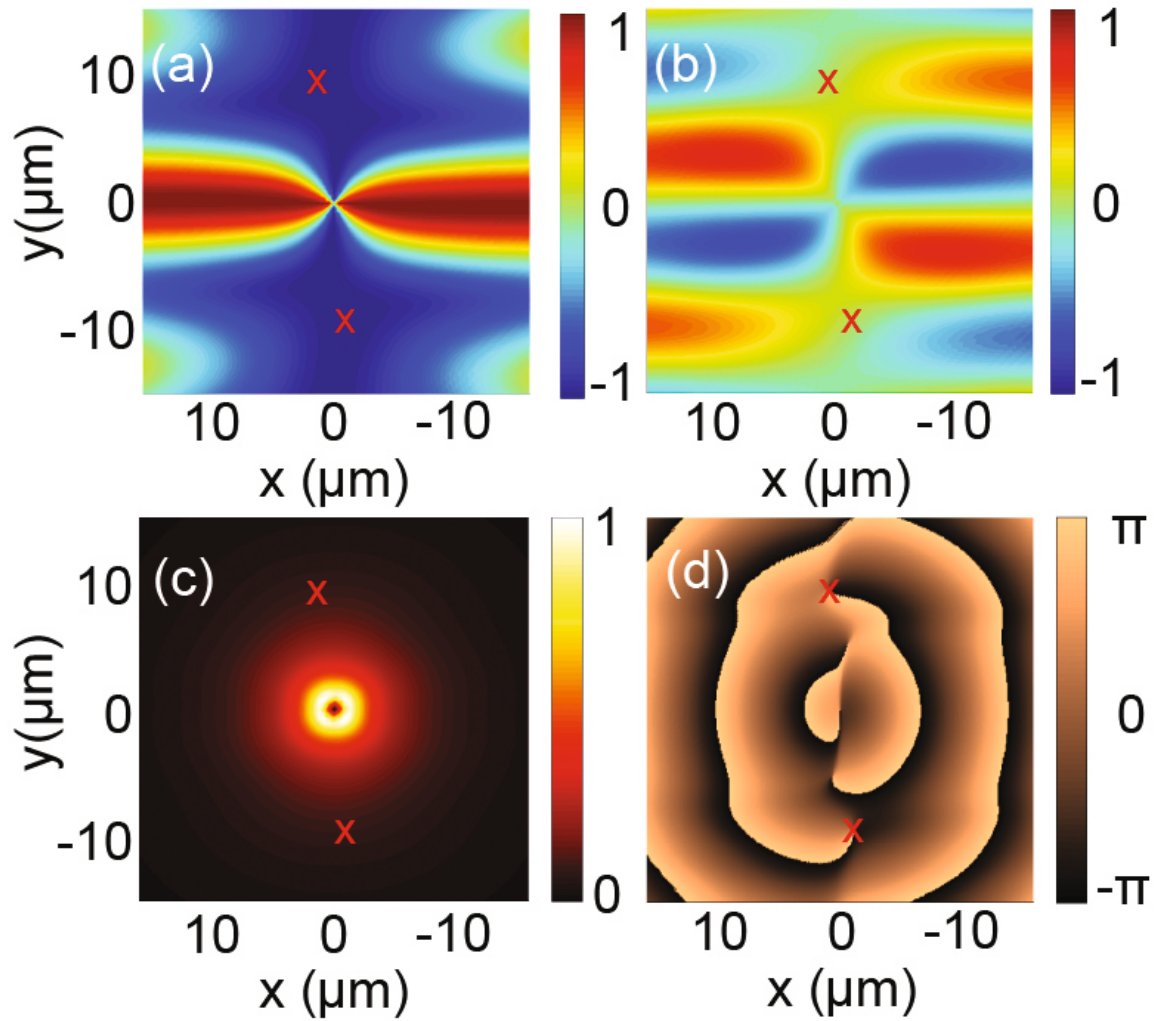


Figure 2.11: (Color online) (a) Degree of linear polarization of bright states. (b) Degree of circular polarization of bright states. (c) Total density of bright states. (d) Phase of x -component of bright states. Red crosses point the phase singularities in x -component. From Vishnevsky et al. (2013) [66].

oscillator strength, indirect excitons can be probed on the direct exciton transition frequency. The suggested technique is based on the optically induced reflectivity and Kerr rotation effects stemming from the interactions between direct and indirect excitons. Importantly, both dark and bright states can be probed using this approach, contrary to photoluminescence measurements. A proof-of-concept pump-probe experiment was modelled with the density matrix approach applied to relaxational kinetics of excitons. An experimental work based on the proposed technique confirmed our predictions [52].

The second work gives an explanation of experimentally observed specific phase dislocations in regions of an indirect exciton condensate, where the excitonic density does not vanish [17]. We have shown that skyrmions, topologically nontrivial spin configurations, may emerge in this type of condensates. Contrary to topological defects like vortices, they are described with a constant density field and their existence may explain the observed phase dislocations.

Chapter 3

Spin dynamics of the polariton optical parametric oscillator

The optical parametric oscillator (OPO) device scheme can be realized with planar microcavities, as it was demonstrated in the first chapter. The OPO is a frequency converting optical device, which exploits the light-matter coupling in microcavities to obtain a strong optical nonlinearity. Parametric scattering, which converts light frequency, is due to Coulomb interaction between excitonic components of polaritons. Apart from this, the OPO relies on the bosonic nature of cavity polaritons, which provides stimulation of parametric scattering.

The OPO may convert not only light frequency, but polarization as well. In particular, linear polarization of excitation may be rotated by 90° and also converted to circular polarization [70, 71, 72]. This system therefore is of a special interest from the point of view of spin dynamics.

This chapter is focused on two spin-related effects in the OPO scheme. Polarization inversion effect is introduced in Section 1 and studied profoundly on a particular case of a one-dimensional potential trap in a planar microcavity. Experimental observation of nontrivial behaviour of polarization inversion is explained in terms of Boltzmann kinetic equations formalism and Gross-Pitaevskii equation [73]. The idea of an OPO scheme realization with dipolaritons, light-matter quasi-particles with an indirect exciton component, is discussed in Section 2. Possibility of voltage control and switching of polarization inversion is predicted in this system [29].

3.1 Optical parametric oscillator in one-dimensional trap potential

Resonant optical excitation of a specific point on the lower polariton energy dispersion branch results in parametric scattering of polaritons. In this process, a pair of optically pumped polaritons elastically scatters, so that one of the polaritons loses its kinetic energy and goes towards the ground state, while the other gains energy and finishes on the top of the lower polariton branch. If pumping power is sufficient, a polariton macrooccupied state (which is sometimes simply called a "condensate") is formed in the bottom of the dispersion branch and the parametric scattering is stimulated due to bosonic nature of

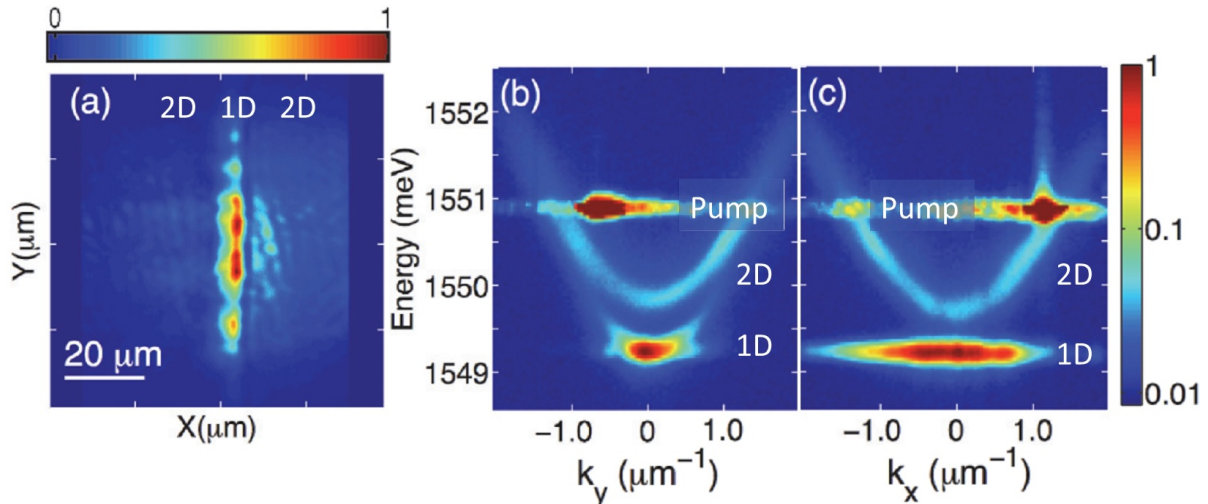


Figure 3.1: Real-space emission, and polariton dispersion for 2D phase-matching conditions. In (a), the normalized real-space emission is shown, integrated in energy and in a linear false-color scale, in a region of the sample where the planar cavity is split by a line defect; (b) shows the dispersion taken along the axis of the 1D system. Here, both systems show nonlinear emission from the bottom of their respective branch. In (c), the dispersion is normal to the 1D system: marked differences are seen, the 1D system shows no dispersion while the 2D remains the same. A logarithmic false-color scale is used for (b) and (c). From Cuadra et al. (2013) [73].

polaritons.

Polarization inversion effect in planar microcavities, explained by the opposite signs of polariton-polariton scattering matrix elements in signlet and triplet configurations (anti-parallel and parallel spins), consists in rotation of the linear polarization plane of light by 90° with respect to that of the optical pumping. Due to the axial symmetry of a planar microcavity (if the TE-TM splitting is neglected), the rotation angle is constant and does not depend on pump linear polarization plane orientation.

A one-dimensional in-plane cavity defect reduces the symmetry and may affect the polarization inversion behavior. It may also reduce the polariton dimensionality, acting as a potential trap for polaritons in the cavities of the type of a quantum wire. In this case, the OPO scheme may be tuned so that the signal state is confined in the trap, as it is shown in Fig. 3.1. The parametric scattering conditions may be as well satisfied for both confined 1D signal and planar 2D signal states, so that two condensates are formed at the same time. Such a situation is demonstrated in Fig. 3.2. The size quantization splits the 1D signal states linearly polarized parallel and perpendicularly to the defect axis. Should the value of this splitting exceed polariton linewidths, it strongly affects the energy conservation condition, making parametric scattering more preferable for one of the linear polarizations. Experimental measurement of the signal linear polarization plane orientation dependence on that of the pumping demonstrates that it makes two full circumrotations when the latter makes one [73].

The present section is organized as follows. Subsection 1 introduces the semi-classical Boltzmann equations approach used for the simulation of the OPO in a planar microcavity.

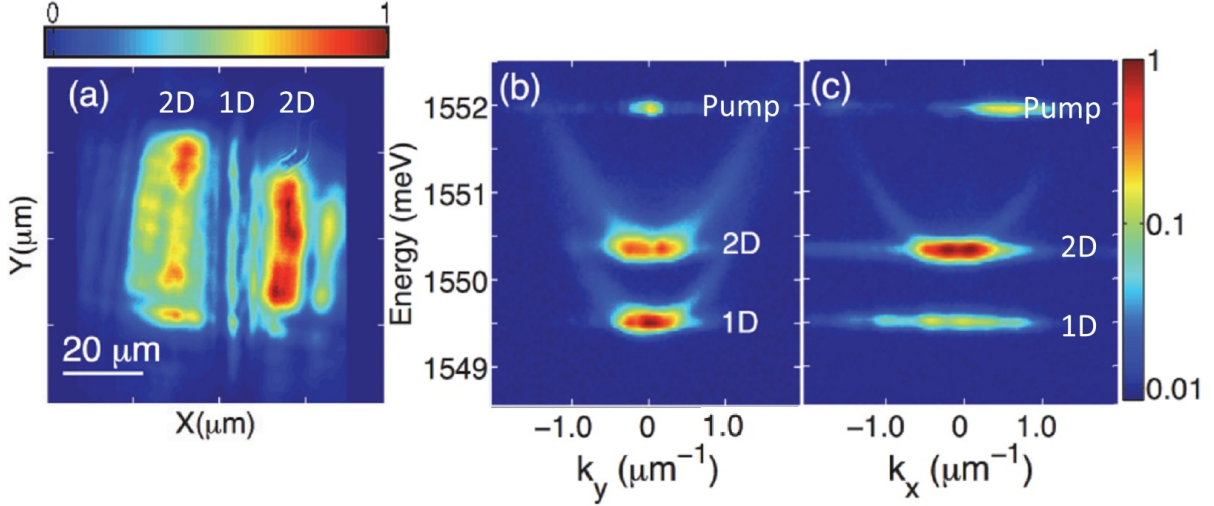


Figure 3.2: Real-space emission, and polariton dispersion for 1D phase-matching conditions. In (a), the normalized real-space emission, integrated in energy, at the same region as in Fig. 2 is shown in a linear false-color scale, but now there is only significant emission from the 1D condensate. (b) Dispersion taken along the axis of the 1D system. Here, the 2D polariton dispersion does not show condensation, whereas in the 1D system nonlinear emission is found. In (c), the dispersion is normal to the 1D system: marked difference are seen, the 1D system shows no dispersion while the 2D remains the same. A logarithmic false-color scale is used for (b) and (c). From Cuadra et al. (2013) [73].

The polarization inversion effect is derived from this model in Subsection 2. The model is generalized to the case of a one-dimensional potential trap in Subsection 3. The model is further checked with numerical solution of the Gross-Pitaevskii equation in Subsection 4.

3.1.1 Semiclassical Boltzmann kinetic equations model

Polariton-polariton scattering is strongly anisotropic. It stems from the Coulomb interaction between the excitonic components of microcavity polaritons. The latter is mostly due to carrier exchange between excitons and is only allowed for pairs of excitons with aligned spins. For excitons with opposite spin projections, scattering matrix element is only nonzero in the second order of perturbation theory [74].

The semi-classical Boltzmann equation formalism, introduced in Chapter 1, may be generalized to account for the spin anisotropic polariton-polariton scattering [75]. The equations for the populations of plane wave states $N_{\mathbf{k}\uparrow(\downarrow)}$, having spin up(down) spin projection, and the corresponding total in-plane pseudospin $\mathbf{S}_{\mathbf{k}}$ read [6]:

$$\frac{dN_{\mathbf{k}\uparrow(\downarrow)}}{dt} = -\frac{N_{\mathbf{k}\uparrow(\downarrow)}}{\tau_k} + \left(\frac{dN_{\mathbf{k}\uparrow(\downarrow)}}{dt}\right)\Big|_{rot} + \left(\frac{dN_{\mathbf{k}\uparrow(\downarrow)}}{dt}\right)\Big|_{p-p} + P_{\mathbf{k}}, \quad (3.1)$$

$$\frac{d\mathbf{S}_{\mathbf{k}}}{dt} = -\frac{\mathbf{S}_{\mathbf{k}}}{\tau_k} + \left(\frac{d\mathbf{S}_{\mathbf{k}}}{dt}\right)\Big|_{rot} + \left(\frac{d\mathbf{S}_{\mathbf{k}}}{dt}\right)\Big|_{p-p} + \mathbf{P}_{\mathbf{k}}. \quad (3.2)$$

Here τ_k is the radiational decay time, which depends on the polariton wave vector value k , $P_{\mathbf{k}}$ and $\mathbf{P}_{\mathbf{k}}$ are the source terms describing excitation of polarized quasiparticles.

The second terms in the right-hand parts of Eqs. (3.1,3.2) account for spin rotation in effective magnetic field created by TE-TM splitting ($\boldsymbol{\Omega}_{\text{TE-TM},\mathbf{k}}$) [76], (ii) polarization splittings due to microcavity in-plane asymmetry ($\boldsymbol{\Omega}_{\text{a},\mathbf{k}}$) and spin-anisotropic polariton-polariton interactions ($\boldsymbol{\Omega}_{\text{int},\mathbf{k}}$):

$$\left(\frac{dN_{k\uparrow}}{dt}\right)\Big|_{\text{rot}} = -\left(\frac{dN_{k\downarrow}}{dt}\right)\Big|_{\text{rot}} = \mathbf{e}_z \cdot [\mathbf{S}_k \times (\boldsymbol{\Omega}_{\text{TE-TM},\mathbf{k}} + \boldsymbol{\Omega}_{\text{a},\mathbf{k}})] , \quad (3.3)$$

$$\left(\frac{d\mathbf{S}_k}{dt}\right)\Big|_{\text{rot}} = [\mathbf{S}_k \times \boldsymbol{\Omega}_{\text{int},\mathbf{k}}] + \frac{N_{k\uparrow} - N_{k\downarrow}}{2} (\boldsymbol{\Omega}_{\text{TE-TM},\mathbf{k}} + \boldsymbol{\Omega}_{\text{a},\mathbf{k}}) . \quad (3.4)$$

The effective field describing the energy splitting between the two spin components due to the spin-anisotropic interactions reads [77, 78]:

$$\hbar\boldsymbol{\Omega}_{\text{int},\mathbf{k}} = 2\mathbf{e}_z \sum_{\mathbf{k}'} \left(V_{\mathbf{k},\mathbf{k}',0}^{(1)} - V_{\mathbf{k},\mathbf{k}',0}^{(2)} \right) (N_{\mathbf{k}'\uparrow} - N_{\mathbf{k}'\downarrow}) + 2 \sum_{\mathbf{k}'} V_{\mathbf{k},\mathbf{k}',0}^{(2)} \mathbf{S}'_{\mathbf{k}} \quad (3.5)$$

where $V^{(1)}$ and $V^{(2)}$ are the matrix elements of polariton-polariton scattering described in detail below, and \mathbf{e}_z is a unit vector in the z direction of the Stokes space, corresponding to circularly polarized light.

The third pair of terms in Eqs. (3.1,3.2) describe the polariton-polariton stimulated scattering with a transfer of momentum:

$$\begin{aligned} \left(\frac{dN_{\mathbf{k}\uparrow}}{dt}\right)\Big|_{p-p} = & \sum_{\mathbf{k}',\mathbf{q}} \left\{ W_{\mathbf{k},\mathbf{k}',\mathbf{q}}^{(1)} [(N_{\mathbf{k}\uparrow} + N_{\mathbf{k}'\uparrow} + 1)N_{\mathbf{k}+\mathbf{q}\uparrow}N_{\mathbf{k}'-\mathbf{q}\uparrow} - (N_{\mathbf{k}+\mathbf{q}\uparrow} + N_{\mathbf{k}'-\mathbf{q}\uparrow} + 1)N_{\mathbf{k}\uparrow}N_{\mathbf{k}'\uparrow}] \right. \\ & + W_{\mathbf{k},\mathbf{k}',\mathbf{q}}^{(1)} [(N_{\mathbf{k}\uparrow} + N_{\mathbf{k}'\downarrow} + 1)(N_{\mathbf{k}+\mathbf{q}\uparrow}N_{\mathbf{k}'-\mathbf{q}\downarrow} + N_{\mathbf{k}+\mathbf{q}\downarrow}N_{\mathbf{k}'-\mathbf{q}\uparrow}) + 2\mathbf{S}_{\mathbf{k}+\mathbf{q}} \cdot \mathbf{S}'_{\mathbf{k}'-\mathbf{q}}] \\ & - (N_{\mathbf{k}\uparrow}N_{\mathbf{k}'\downarrow} + (\mathbf{S}_{\mathbf{k}} \cdot \mathbf{S}'_{\mathbf{k}'}))(N_{\mathbf{k}+\mathbf{q}\uparrow} + N_{\mathbf{k}'-\mathbf{q}\downarrow} + N_{\mathbf{k}+\mathbf{q}\downarrow} + N_{\mathbf{k}'-\mathbf{q}\uparrow} + 2) \\ & + 2W_{\mathbf{k},\mathbf{k}',\mathbf{q}}^{(12)} [N_{\mathbf{q}\uparrow}(\mathbf{S}'_{\mathbf{k}'} \cdot \mathbf{S}'_{\mathbf{k}'-\mathbf{q}}) + N_{\mathbf{k}'-\mathbf{q}\uparrow}(\mathbf{S}'_{\mathbf{k}'} \cdot \mathbf{S}_{\mathbf{k}+\mathbf{q}}) - N_{\mathbf{k}\uparrow}\mathbf{S}'_{\mathbf{k}'} \cdot (\mathbf{S}'_{\mathbf{k}'-\mathbf{q}} + \mathbf{S}_{\mathbf{k}+\mathbf{q}})] \\ & + W_{\mathbf{k},\mathbf{k}',\mathbf{q}}^{(12)} [(\mathbf{S}_{\mathbf{k}} \cdot \mathbf{S}_{\mathbf{k}+\mathbf{q}})(N_{\mathbf{k}'-\mathbf{q}\uparrow} + N_{\mathbf{k}'-\mathbf{q}\downarrow} - N_{\mathbf{k}'\uparrow} - N_{\mathbf{k}'\downarrow}) \\ & \left. + (\mathbf{S}_{\mathbf{k}} \cdot \mathbf{S}'_{\mathbf{k}'-\mathbf{q}})(N_{\mathbf{k}+\mathbf{q}\uparrow} + N_{\mathbf{k}+\mathbf{q}\downarrow} - N_{\mathbf{k}'\uparrow} - N_{\mathbf{k}'\downarrow}) \right\} \quad (3.6) \end{aligned}$$

$$\begin{aligned}
\left(\frac{d\mathbf{S}_k}{dt}\right)\Big|_{p-p} &= \sum_{\mathbf{k}',\mathbf{q}} \left\{ \frac{W_{\mathbf{k},\mathbf{k}',\mathbf{q}}^{(1)}}{2} \mathbf{S}_k [N_{\mathbf{k}+\mathbf{q}\uparrow} N_{\mathbf{k}'-\mathbf{q}\uparrow} + N_{\mathbf{k}+\mathbf{q}\downarrow} N_{\mathbf{k}'-\mathbf{q}\downarrow}] \right. \\
&\quad - N_{\mathbf{k}'\uparrow} (N_{\mathbf{k}+\mathbf{q}\uparrow} + N_{\mathbf{k}'-\mathbf{q}\uparrow} + 1) - N_{\mathbf{k}'\downarrow} (N_{\mathbf{k}+\mathbf{q}\downarrow} + N_{\mathbf{k}'-\mathbf{q}\downarrow} + 1)] \\
&\quad + W_{\mathbf{k},\mathbf{k}',\mathbf{q}}^{(1)} (\mathbf{S}_{\mathbf{k}+\mathbf{q}} (\mathbf{S}_{\mathbf{k}'} \cdot \mathbf{S}_{\mathbf{k}'-\mathbf{q}}) + \mathbf{S}_{\mathbf{k}'-\mathbf{q}} (\mathbf{S}_{\mathbf{k}'} \cdot \mathbf{S}_{\mathbf{k}+\mathbf{q}}) - \mathbf{S}_{\mathbf{k}'} (\mathbf{S}_{\mathbf{k}+\mathbf{q}} \cdot \mathbf{S}_{\mathbf{k}'-\mathbf{q}})) \\
&\quad + \frac{W_{\mathbf{k},\mathbf{k}',\mathbf{q}}^{(2)}}{2} [2(\mathbf{S}_k + \mathbf{S}_{\mathbf{k}'})(N_{\mathbf{k}+\mathbf{q}\uparrow} N_{\mathbf{k}'-\mathbf{q}\downarrow} + N_{\mathbf{k}+\mathbf{q}\downarrow} N_{\mathbf{k}'-\mathbf{q}\uparrow}) + 2(\mathbf{S}_{\mathbf{k}+\mathbf{q}} \cdot \mathbf{S}_{\mathbf{k}'-\mathbf{q}})] \\
&\quad - (\mathbf{S}_k (N_{\mathbf{k}'\uparrow} + N_{\mathbf{k}'\downarrow}) + \mathbf{S}_1 (N_{\mathbf{k}\uparrow} + N_{\mathbf{k}\downarrow})) (N_{\mathbf{k}+\mathbf{q}\uparrow} + N_{\mathbf{k}'-\mathbf{q}\uparrow} + N_{\mathbf{k}+\mathbf{q}\downarrow} + N_{\mathbf{k}'-\mathbf{q}\downarrow} + 2)] \\
&\quad - 2W_{\mathbf{k},\mathbf{k}',\mathbf{q}}^{(12)} \mathbf{S}_k ((\mathbf{S}_{\mathbf{k}'} \cdot \mathbf{S}_{\mathbf{k}+\mathbf{q}}) + (\mathbf{S}_{\mathbf{k}'} \cdot \mathbf{S}_{\mathbf{k}'-\mathbf{q}})) \\
&\quad + \frac{W_{\mathbf{k},\mathbf{k}',\mathbf{q}}^{(12)}}{2} \mathbf{S}_{\mathbf{k}'-\mathbf{q}} [2((N_{\mathbf{k}'\uparrow} + 1)N_{\mathbf{k}+\mathbf{q}\uparrow} + (N_{\mathbf{k}'\downarrow} + 1)N_{\mathbf{k}+\mathbf{q}\downarrow}) \\
&\quad + (N_{\mathbf{k}+\mathbf{q}\uparrow} + N_{\mathbf{k}+\mathbf{q}\downarrow} - N_{\mathbf{k}'\uparrow} - N_{\mathbf{k}'\downarrow})(N_{\mathbf{k}\uparrow} + N_{\mathbf{k}\downarrow})] \\
&\quad + \frac{W_{\mathbf{k},\mathbf{k}',\mathbf{q}}^{(12)}}{2} \mathbf{S}_{\mathbf{k}+\mathbf{q}} [2((N_{\mathbf{k}'\uparrow} + 1)N_{\mathbf{k}'-\mathbf{q}\uparrow} + (N_{\mathbf{k}'\downarrow} + 1)N_{\mathbf{k}'-\mathbf{q}\downarrow}) \\
&\quad + (N_{\mathbf{k}'-\mathbf{q}\uparrow} + N_{\mathbf{k}'-\mathbf{q}\downarrow} - N_{\mathbf{k}'\uparrow} - N_{\mathbf{k}'\downarrow})(N_{\mathbf{k}\uparrow} + N_{\mathbf{k}\downarrow})] \left. \right\}. \tag{3.7}
\end{aligned}$$

A similar term for $N_{\mathbf{k}\uparrow}$ is obtained with a transformation $\uparrow \leftrightarrow \downarrow$. The parameters $W^{(1)}$, $W^{(2)}$ and $W^{(12)}$ represent the polariton-polariton interactions in different spin configurations:

$$W_{\mathbf{k},\mathbf{k}',\mathbf{q}}^{(1)} = \frac{2\pi}{\hbar} \left| V_{\mathbf{k},\mathbf{k}',\mathbf{q}}^{(1)} \right|^2 \delta(\Omega_{\mathbf{k}} + \Omega_{\mathbf{k}'} - \Omega_{\mathbf{k}+\mathbf{q}} - \Omega_{\mathbf{k}-\mathbf{q}}) \tag{3.8}$$

$$W_{\mathbf{k},\mathbf{k}',\mathbf{q}}^{(2)} = \frac{2\pi}{\hbar} \left| V_{\mathbf{k},\mathbf{k}',\mathbf{q}}^{(2)} \right|^2 \delta(\Omega_{\mathbf{k}} + \Omega_{\mathbf{k}'} - \Omega_{\mathbf{k}+\mathbf{q}} - \Omega_{\mathbf{k}-\mathbf{q}}) \tag{3.9}$$

$$W_{\mathbf{k},\mathbf{k}',\mathbf{q}}^{(12)} = \frac{2\pi}{\hbar} \text{Re}(V_{\mathbf{k},\mathbf{k}',\mathbf{q}}^{(1)} V_{\mathbf{k},\mathbf{k}',\mathbf{q}}^{*(2)}) \delta(\Omega_{\mathbf{k}} + \Omega_{\mathbf{k}'} - \Omega_{\mathbf{k}+\mathbf{q}} - \Omega_{\mathbf{k}-\mathbf{q}}) \tag{3.10}$$

Eq. (3.8)-(3.10) are written for the most general case. Taking into account the excitonic fraction of the relevant to the OPO scheme states $V^{(1)}$ and $V^{(2)}$ are the polariton parametric scattering matrix elements in triplet and singlet configurations respectively.

Kinetic equations (3.1,3.2) are formulated for an infinite and, in general, continuous space of states. In the case of the OPO, the population of most of these states, except for the pump, signal and idler ones, may be safely neglected. The infinite system of equations thus is reduced to a system of 9 equations for the populations and the total in-plane pseudospins.

3.1.2 Polarization inversion

The semi-classical Boltzmann kinetic equations account for the bosonic stimulation of parametric scattering. However, it is only important when the population of the signal state is macroscopic ($N_{s,\uparrow(\downarrow)} \sim 1$). This condition is not fulfilled at the initial phase of OPO, when a constant wave optical pumping is being turned on. In this case, $N_{s(i),\uparrow(\downarrow)} \ll 1 \ll N_{p,\uparrow(\downarrow)}$, $|\mathbf{S}_{s(i),\uparrow(\downarrow)}| \ll 1 \ll |\mathbf{S}_{p,\uparrow(\downarrow)}|$, and the kinetic equations for the signal state are

simplified:

$$\frac{dN_{s\uparrow(\downarrow)}}{dt} = W^{(1)} N_{p\uparrow(\downarrow)}^2 + 2W^{(2)} (N_{p\uparrow(\downarrow)} N_{p\downarrow(\uparrow)} + |\mathbf{S}_p|^2), \quad (3.11)$$

$$\frac{d\mathbf{S}_s}{dt} = 2W^{(12)} \mathbf{S}_p (N_{p\uparrow} + N_{p\downarrow}), \quad (3.12)$$

If the pump state is linearly polarized, $N_{p\uparrow} = N_{p\downarrow} = |\mathbf{S}_p|$, and therefore the signal average pseudospin in this regime reads:

$$\frac{\mathbf{S}_s}{N_{s\uparrow} + N_{s\downarrow}} = \frac{4W^{(12)}}{W^{(1)} + 4W^{(2)}} \frac{\mathbf{S}_p}{|\mathbf{S}_s|}. \quad (3.13)$$

The characteristic values of the ratio $V^{(2)}/V^{(1)} \sim -0.01$ [70, 79] yields negative parameter $W^{(12)}$ and positive $W^{(1)} \gg W^{(2)}$. From this, one concludes that signal and pump pseudospins have opposite directions. For a pair of in-plane pseudospins this means that the linear polarization planes of the states, described with these pseudospins, are perpendicular. In other words, the signal linear polarization plane is rotated with respect to that of the pump by 90° . The relation between the signal and pump linear polarization degrees reads:

$$\frac{\rho_s}{\rho_p} \approx -4 \frac{V^{(2)}}{V^{(1)}}. \quad (3.14)$$

The initial signal pseudospin and, therefore, the linear polarization are conserved when the stimulated scattering regime turns on. This is due to the fact that scattering to the signal states, initially populated during the spontaneous scattering regime, becomes stimulated and preferable. Signal parameters are thus auto-locked and the OPO system works in a steady state, defined by the initial phase.

3.1.3 One-dimensional trap potential effect

A quantum-wire type potential trap acting on the photonic component of cavity polaritons may be either engineered or appear spontaneously from a structure defect. Depending on the trap width and energy depth, it produces a number of size-quantized polaritonic subbands from the lower branch of the energy dispersion. The quasi-1D polariton states, nevertheless, have a finite overlap with 2D cavity states, so that the freely propagating states may be parametrically scattered into the confined ones. Taking into account the finite lifetime and linewidth of lower branch polaritons, several signal states, 1D and 2D, may satisfy the energy conservation conditions for parametric scattering.

The TE-TM splitting, which may be interpreted in terms of different effective masses $m_L < m_T$ for states, linearly polarized longitudinally and transversely to the wave vector, affects the size quantization in the trap. It is even further enhanced in 1D confined systems because of strain and other mechanisms. The size quantization energy depends on the masses of states with in-plane wave vectors normal to the potential trap axis. Polariton states in a sufficiently thin trap contain sufficiently large wavevectors in the reciprocal space, in the normal to the trap axis direction. TE-TM splitting therefore produces a strong energy splitting of linear polarizations parallel and perpendicular to the trap.

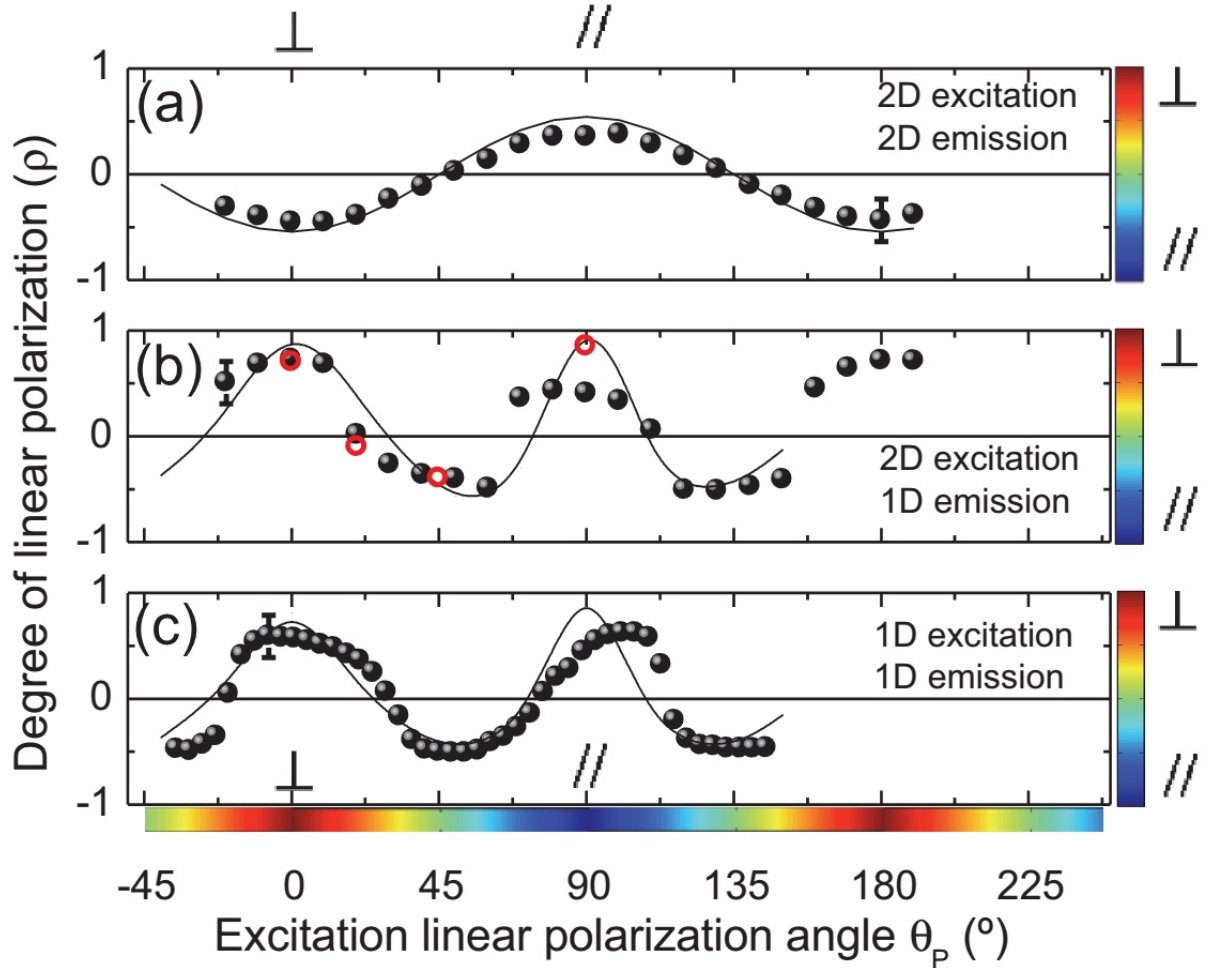


Figure 3.3: Degree of linear polarization as a function of the linear polarization angle of the pump: Color bars next to the vertical and bottom axis represent the DLP of the emission and the pump, respectively. At $\theta_P = 0^\circ$ ($\theta_P = 90^\circ$), the laser is polarized normal (parallel) to the wire, as indicated by the \perp (\parallel) symbol. The symbols at the ordinates indicate the main orientation of the emissions polarization plane: \perp (\parallel) perpendicular (normal) to the wire axis. (a) The evolution of the DLP for the 2D system, for 2D phase-matching conditions. (b) The evolution of the DLP for the 1D system, for 2D phase-matching conditions. (c) The evolution of the DLP for the 1D system, for 1D phase-matching conditions. Experimental data is plotted with black circles. The solid lines (red open points) are calculated DLPs using the Boltzmann (GP) model. From Cuadra et al. (2013) [73].

In Ref. [73], this splitting is of the order of 0.1 meV and is comparable to the polaron linewidths. Consequently, it strongly affects the energy conservation conditions for parametric scattering and cannot be included into the Boltzmann kinetic equations model only via an effective magnetic field, rotating the spin of the signal state. To incorporate the linear polarization splitting into the model, one may introduce a phenomenological term to the signal pseudospin evolution equation:

$$\frac{d\mathbf{S}_s}{dt} = -\frac{\mathbf{S}_s}{\tau_s} + \left(\frac{d\mathbf{S}_s}{dt}\right)\Big|_{rot} + \left(\frac{d\mathbf{S}_s}{dt}\right)\Big|_{p-p} + \mathbf{e}_x \delta W \left(\frac{dN_s}{dt}\right)\Big|_{p-p}, \quad (3.15)$$

where \mathbf{e}_x is the unitary vector along the x axis, coinciding with the trap axis, and the coefficient δW is defined by:

$$\delta W = (W_\perp - W_\parallel)/(W_\perp + W_\parallel). \quad (3.16)$$

The new term proportional to δW originates from the difference in the overlap integrals between the states localized in the trap and the extended propagating states of the pump and the idler. Indeed, the trap is wide enough to contain several quantized levels, and the highest levels of the two orthogonal polarizations that become strongly populated in the experiments, do not have the same transverse quantum number n , otherwise the transverse-polarized state \perp would be higher in energy than the longitudinal-polarized state \parallel because of the longitudinal-transverse splitting. The overlap integrals, contained in the scattering rates W , exhibit a $1/n$ dependence, implying that scattering into the lower lying states is favored. On the other hand, phase matching conditions favor the population of higher lying ones, because the pump is tuned to the free 2D signal resonance conditions. This balance leads actually to a further decrease of δW . Thus, this term is comparable to the one responsible for the polarization inversion (the latter is proportional to α_2/α_1), and the competition between them can determine the relative sign of the signal and pump DLP. Values of $\alpha_2/\alpha_1 = -0.01$ and $\delta W = 0.008$ are typically used in the simulations. Thus, in the spontaneous scattering regime the term given in Eq.(3.15) competes with the polarization inversion, which is proportional to $\alpha_1 \times \alpha_2$.

The signal linear polarization degree, obtained with numerical solution of the semi-classical Boltzmann kinetic equations, in dependence on the pump linear polarization plane orientation with respect to the trap axis, is plotted with solid lines in Fig. 3.3 in different situations. It qualitatively reproduces the experimental results. In particular, the linear polarization degree of the 1D signal changes sign twice faster than that of the 2D signal both for 2D and 1D phase-matching conditions.

3.1.4 Gross-Pitaevskii model

In the first model, we write the coupled equations for a 2D four-component exciton-photon wavefunction composed by a photonic fraction $\psi_{\uparrow\downarrow}(x, y)$ and an excitonic fraction $\varphi_{\uparrow\downarrow}(x, y)$:

$$i\hbar \frac{\partial \psi_{\uparrow\downarrow}}{\partial t} = -\frac{\hbar^2}{2m_{ph}} \Delta \psi_{\uparrow\downarrow} + \frac{\hbar\Omega_R}{2} \varphi_{\uparrow\downarrow} + H_x \psi_{\uparrow\downarrow} + U \psi_{\uparrow\downarrow} - \frac{i\hbar}{2\tau_{ph}} \psi_{\uparrow\downarrow} + P_{\uparrow\downarrow} + f_{\uparrow\downarrow} \quad (3.17)$$

$$i\hbar\frac{\partial\varphi_{\uparrow\downarrow}}{\partial t} = -\frac{\hbar^2}{2m_X}\Delta\varphi_{\uparrow\downarrow} + \frac{\hbar\Omega_R}{2}\psi_{\uparrow\downarrow} + \alpha_1|\varphi_{\uparrow\downarrow}|^2\varphi_{\uparrow\downarrow} + \alpha_2|\varphi_{\downarrow\uparrow}|^2\varphi_{\uparrow\downarrow} \quad (3.18)$$

Here, $m_{ph} = 4 \times 10^{-5}m_0$ is the photon mass, $m_X = 0.6m_0$ is the exciton mass (m_0 is the free electron mass), $\hbar\Omega_R = 4.2$ meV is the Rabi splitting, $\alpha_1 = 6E_b a_B^2$ and $\alpha_2 \sim -0.01\alpha_1$ are the triplet and singlet interaction constants [79], respectively ($E_b = 10$ meV is the exciton binding energy and $a_B = 10$ nm is the exciton Bohr radius). The potential acting on photons and confining them in the trap (width $4.25 \mu\text{m}$, depth 0.6 meV) is described by U ; $\tau_{ph} = 1$ ps is the photon lifetime (the exciton decay is neglected), P is the quasi-resonant pumping term, exciting the system at a given frequency $\omega \approx 1.6$ meV/ \hbar above the bottom of the polariton branch and f is the noise, which serves to account for the effects of spontaneous scattering. Pumping provides an average of 10 particles in a unit cell of $h = 0.25 \mu\text{m}$ in the steady state, and the spontaneous scattering creates 0.01 particle. The term $H_x = \sigma_x \times 30 \mu\text{eV}$ describes the effective magnetic field (and corresponds to polarization splitting of $60 \mu\text{eV}$) acting only inside the 1D wire.

The results of the simulations performed for the same four orientations of the pump polarization as in the experiments ($\theta_P = 0^\circ, 20^\circ, 45^\circ$ and 90°) are presented in the Fig. 3.3, and reproduce qualitatively the experimental values.

In these simulations, as in the experiments, in the 2D region the polarization is always inverted because of the opposite signs of α_1 and α_2 , while in the quantized 1D region the polarization is determined by an interplay between the signs of the α 's coefficients and the splitting between the parallel and transverse polarized modes, as explained in detail below.

Note, that in the simulations the 2D condensate extends over the entire area shown in the figure, in contrast to the experiments, where the condensate's extension is about $40 \mu\text{m}$. Also, the DLP is higher in the calculations than in the experiments; however, a qualitative overall agreement between experiment and theory is evident. Although this model is nicely fitting the experiments, it is quite demanding numerically because of the need for a large 2D grid, small step size (to describe accurately the potential defect and the profiles of the modes), and long calculation times (necessary to obtain spontaneous OPO with a relatively weak noise). However, it further justifies the assumptions and validity of the semiclassical kinetic equations model. The latter is based on the phenomenologically introduced polarization generation term (3.15). The Gross-Pitaevskii equation model naturally satisfies energy conservation and does not need terms introduced by hand. Nevertheless, both models give qualitatively similar predictions for signal polarization dependence on the pump linear polarization angle, in particular, specific doubled angular dependence.

3.2 Dipolariton optical parametric oscillator

Dipolaritons, quasi-particles representing a mixture of light with direct and indirect excitons, have an intrinsic dipole moment oriented normally to the cavity plane by applied electric bias. Coulombic interaction between dipolaritons is therefore stronger in comparison with conventional polaritons. The latter have zero dipole moment on the average and mostly interact via the carrier exchange, which is only possible in a triplet configura-

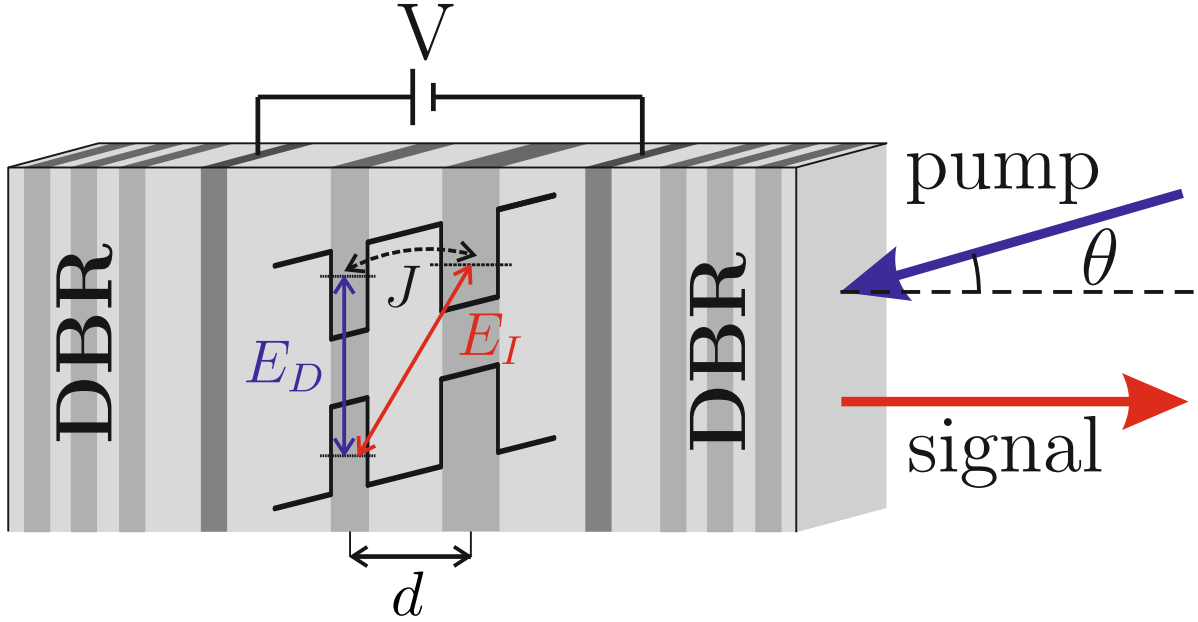


Figure 3.4: A sketch of the studied system: asymmetric double quantum well (ASDQWs) is situated between the contacts and two Bragg reflectors forming a microcavity. Voltage V , applied to the contacts, shifts the energy diagram of the ASDQW and the energies of the indirect (E_I) and direct (E_D) exciton states, coupled via tunneling of the electron through the barrier.

tion of polariton pair [74]. Aside from this mechanism of scattering, dipolaritons directly interact through dipole-dipole repulsion. This mechanism may be at least one order of magnitude stronger [29] than the exchange. This is why the dipolaritons in asymmetric double quantum wells (ASDQWs) are promising candidates for realization of optical parametric oscillators, which rely on parametric scattering of polaritonic quasi-particles.

Moreover, the properties of the dipolaritons strongly depend on the applied electric bias. Indirect excitonic part of the dipolariton states, in particular, may be controlled with voltage, as it is demonstrated in the first chapter. The energy dispersion itself is transformed depending on the electric bias magnitude. Overall, it means that the parametric scattering of dipolaritons may be tuned with applied voltage.

A model cavity with ASDQWs, experimentally studied in Ref. [28], is considered in this chapter. All physical parameters of the system are chosen to fit the photoluminescence measurements [80] for definitiveness. The physical effects, demonstrated on this particular structure, however, may be obtained with arbitrary parameters.

The section is organized as follows. The possibilities of parametric scattering with dipolariton energy dispersion is examined in Subsection 1. The dipolariton-dipolariton scattering matrix elements, entering the Boltzmann kinetic equations for parametric scattering, are calculated in Subsections 2 and 3. Finally, the controllability of polarization inversion effect with voltage is discussed in Subsection 4.

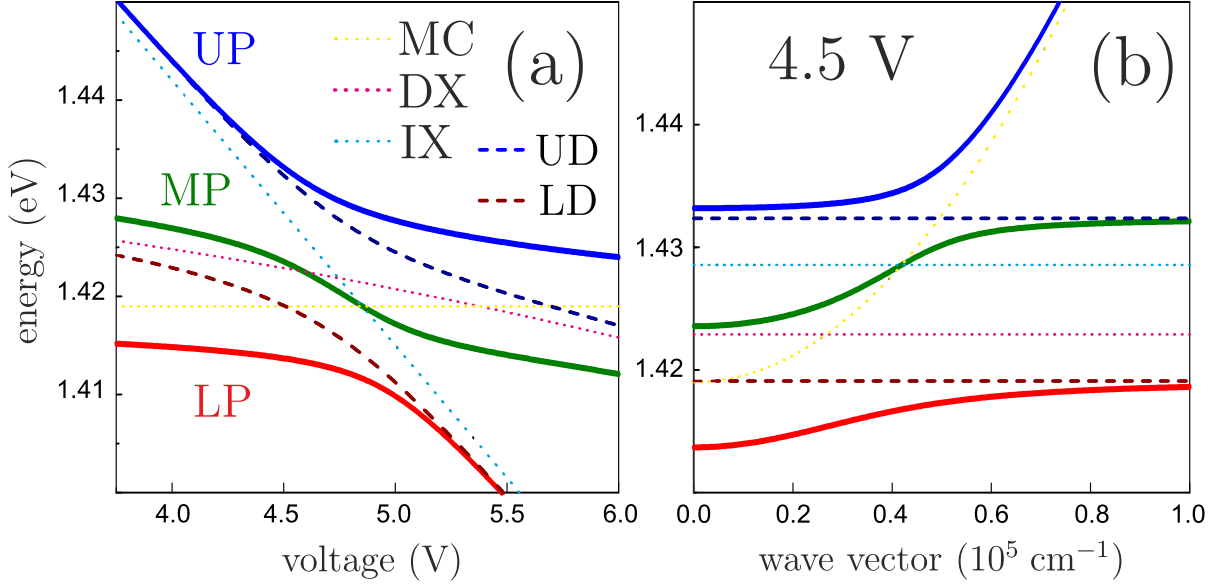


Figure 3.5: Dipolaritonic branches stemming from direct (DX), indirect (IX) excitonic and microcavity photonic modes. (a) Lower (LP), middle (MP) and upper (UP) dipolaritonic branches (solid lines), lower (LD) and upper (UD) dark exciton branches (dashed lines), uncoupled DX, IX and microcavity energies (dotted lines) versus applied voltage at zero wave vector. (b) The same branches versus wave vector at specific voltage (4.5 V). Parameters of the branches calculation are taken to fit the results of the reference [80]. From Nalitov et al. (2014) [29].

3.2.1 Dipolariton parametric scattering

The dipolariton energy dispersion consists of three branches, among which the two lower ones are s-shaped and have inflection points. Therefore, they provide multiple variations of the OPO configuration. The parametric scattering of two dipolaritons from the resonantly excited pump state (Q_p) into the signal ($Q_s = 0$) and idler ($Q_i = 2Q_p$) states conserves both energy and momentum. Solution of the energy conservation equation $2E_p = E_s + E_i$ gives all possible pump state wave vectors, satisfying the parametric scattering condition, as a function of the applied voltage, plotted in Fig. 3.6.

Note, that in contrast to the single-branch OPO schemes, where all states involved in the OPO lie on the same branch (for example, lower polariton branch), the ASDQW structure permits in principle an interbranch OPO scheme with LP signal, MP pump and UP idler states. Such an OPO configuration may be used for generation of entangled photon pairs as both signal and idler states are photonic, therefore the problem of idler polariton coherence loss due to the strong excitonic interactions is avoided.

The UP branch alone does not provide a possibility of a single-branch OPO scheme due to the absence of an inflection point. Moreover, the states lying above the bare exciton energy are resonantly coupled to a large density of excitonic states and can suffer from a significant dephasing, even if their excitonic fraction is small. This dephasing is not accounted for in our approach. The resonant pumping of the LP is therefore the only configuration which we expect to be properly described by our approach.

Parametric scattering rate and spin dynamics are governed by the dipolariton scat-

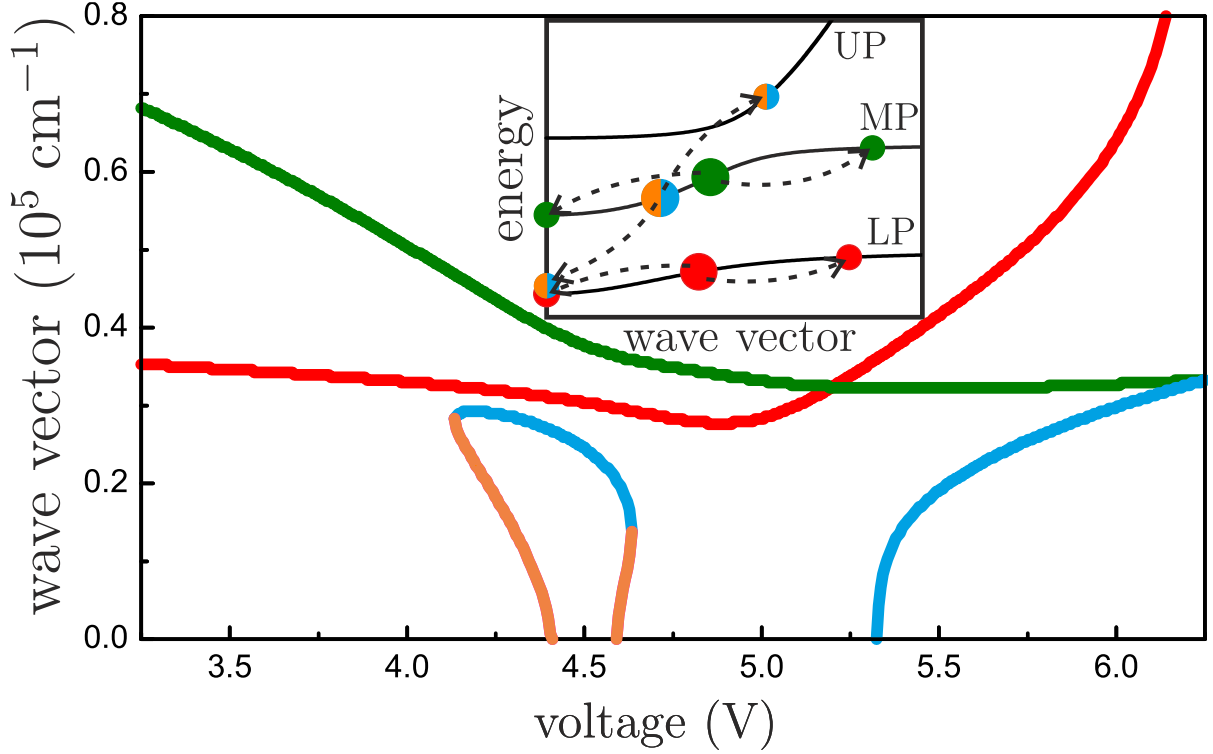


Figure 3.6: Numerical solution of energy-momentum conservation law for parametric scattering, sketched on the inset. Two dipolaritons in the pump state (large circles) scatter to signal and idler states (small circles). Depending on applied bias there are from 2 to 4 solutions corresponding to different scattering configurations. Wave vector of the pump state, representing the magic angle of optical excitation, is plotted with colours corresponding to configurations: red and green for scattering within LP and MP branches, orange and blue for interbranch scattering. From Nalitov et al. (2014) [29].

tering matrix elements entering Boltzmann kinetic equations. They are calculated in the following subsections.

3.2.2 Dipolariton scattering: Born approximation

Dipolariton-dipolariton scattering matrix elements may be calculated using the perturbation theory within the Born approximation and following the approach of references [81, 82, 83]. When the corresponding contribution becomes weak, as it happens for the inter-spin interaction in the range of voltages where IX and DX modes are weakly coupled, we need to proceed further to the second order correction, which is presented in the next subsection.

The excitonic part of a dipolariton pair state, accounting for the fermionic nature of carriers, is constructed from the direct product of two excitonic parts of single dipolariton states, introduced in Chapter 1:

$$|\mathbf{Q}, S; \mathbf{Q}', S'\rangle = [|\mathbf{Q}, S\rangle_{\mathbf{x}} \otimes |\mathbf{Q}', S'\rangle_{\mathbf{x}}]_a, \quad (3.19)$$

where the subscript a denotes the antisymmetrization with respect to the permutations

of both electrons ($\mathbf{r}_e \leftrightarrow \mathbf{r}'_e$, $s_e \leftrightarrow s'_e$) and holes ($\mathbf{r}_h \leftrightarrow \mathbf{r}'_h$, $j_h \leftrightarrow j'_h$).

Considering the two possible spin configurations of a scattering pair, triplet ($S = S'$) and singlet ($S = -S'$), without loss of generality one may write the scattering matrix elements in the Born approximation as:

$$V_{f \leftarrow i}^{(1)} = \langle f | \hat{V} | i \rangle \equiv \langle \mathbf{Q}_f, S; \mathbf{Q}'_f, S' | \hat{V} | \mathbf{Q}_i, S; \mathbf{Q}'_i, S' \rangle$$

with \hat{V} for the scattering potential, which accounts for the inter-exciton carrier Coulomb interactions:

$$\hat{V} = \frac{e^2}{\epsilon} \left[\frac{1}{|\mathbf{r}_e - \mathbf{r}'_e|} + \frac{1}{|\mathbf{r}_h - \mathbf{r}'_h|} - \frac{1}{|\mathbf{r}_e - \mathbf{r}'_h|} - \frac{1}{|\mathbf{r}_h - \mathbf{r}'_e|} \right],$$

where e is the electron charge and ϵ is the dielectric constant.

The matrix elements (3.20) may be decomposed into the following sum:

$$V_{f \leftarrow i}^{(1)} = \sum_{i,j,k,l=IX,DX} C_{i,j}^{k,l}(Q_i, Q'_i, Q_f, Q'_f, V) [\langle \mathbf{Q}_f, S | k \rangle \otimes \langle \mathbf{Q}'_f, S' | l \rangle]_a \hat{V} [|\mathbf{Q}_i, S\rangle_i \otimes |\mathbf{Q}'_i, S'\rangle_j]_a, \quad (3.20)$$

where $C_{i,j}^{k,l} = c_i(Q_i, V) c_j(Q'_i, V) c_k^*(Q_f, V) c_l^*(Q'_f, V)$.

Let us consider the range of wave vectors $Q \ll a_B^{-1}$, where $a_B \sim 10$ nm is the bulk exciton Bohr radius. In this range, all quantum averages in the summation (3.20) are independent on the wave vectors, as their characteristic scale of variation is a_B^{-1} . Therefore, the dependence on the wave vectors, as well as on the bias, is only kept in the Hopfield coefficients product $C_{i,j}^{k,l}(Q_i, Q'_i, Q_f, Q'_f, V)$. Finally, the vanishing overlap of DX and IX wavefunctions allows us to keep only the terms where either $i = k$, $j = l$ or $i = l$, $j = k$, and to obtain:

$$V_{f \leftarrow i}^{(1)} = C_{DX,DX}^{DX,DX} V_{DX,DX}^{S,S'} + C_{IX,IX}^{IX,IX} V_{IX,IX}^{S,S'} + \left[C_{IX,DX}^{IX,DX} + C_{IX,DX}^{DX,IX} + C_{DX,IX}^{IX,DX} + C_{DX,IX}^{DX,IX} \right] V_{DX,IX}^{S,S'} \quad (3.21)$$

with interaction constants $V_{DX,DX}^{S,S'}$, $V_{IX,IX}^{S,S'}$ and $V_{DX,IX}^{S,S'}$ representing DX-DX [49], IX-IX [84] and DX-IX [45] interactions. The corresponding matrix elements can be written as follows:

$$V_{i,j}^{S,S'} = [\langle 0, S | i \rangle \otimes \langle 0, S' | j \rangle]_a \hat{V} [|\mathbf{0}, S\rangle_i \otimes |\mathbf{0}, S'\rangle_j]_a. \quad (3.22)$$

where i, j span over IX, DX. The spin dependence of each of the above integrals is then conveniently described by its decomposition into a sum of four terms with evident spin parts:

$$V_{i,j}^{S,S'} = V_{i,j}^{\text{dir}} + \delta_{S,S'} V_{i,j}^{\text{X}} + \delta_{s_e, s'_e} V_{i,j}^{\text{e}} + \delta_{j_h, j'_h} V_{i,j}^{\text{h}}, \quad (3.23)$$

The first term represents the direct dipole-dipole interaction and is present for any combination of exciton spins. The second term describes the exciton exchange contribution and accounts for the bosonic nature of the exciton. Finally, the last two terms represent the electron and hole exchange contributions, accounting for the fermionic nature of the carriers. Matrix elements (3.22) are evidently expressed in these terms:

$$\begin{aligned} V_{i,j}^{+1,+1} &= V_{i,j}^{\text{dir}} + V_{i,j}^{\text{X}} + V_{i,j}^{\text{e}} + V_{i,j}^{\text{h}}, \\ V_{i,j}^{+1,-1} &= V_{i,j}^{\text{dir}} \end{aligned} \quad (3.24)$$

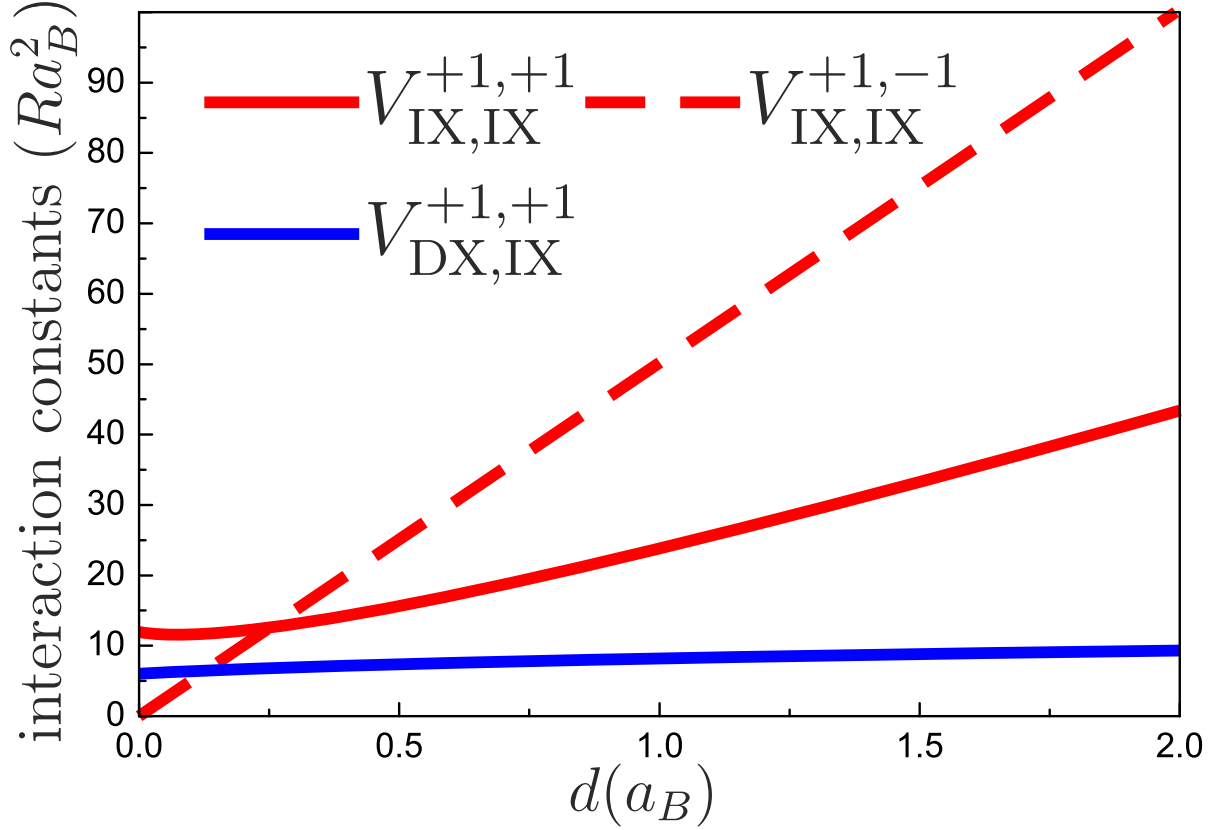


Figure 3.7: Interaction parameters calculated in Born approximation as a function of the separation distance between the QWs. The red lines represent interaction between two IXs, while the blue one corresponds to the interaction of an IX with a DX. The solid lines describe interaction of two excitons with the same spin ($\alpha_1^{\text{II}}, \alpha_1^{\text{DI}}$) and the dashed one is for two excitons with opposite spins (α_2^{II}). From Nalitov et al. (2014) [29].

Neglecting the DX dipole with respect to that of the IX results in $V_{\text{DX,DX}}^{+1,-1} = V_{\text{DX,IX}}^{+1,-1} = 0$. Figure 3.7 shows the dependence of nonzero matrix elements (3.24) on the QWs separation distance d . The zero separation limit corresponds to the transition from IX to DX. At $d \approx a_B/4$, the carrier exchange contribution changes sign and therefore $V_{\text{IX,IX}}^{+1,-1} > V_{\text{IX,IX}}^{+1,+1}$ for $d > a_B/4$.

Note that $V_{\text{DX,IX}}^{+1,+1}$, plotted by the blue line, is inaccurate in the vicinity of the point $d = 0$, where the IX and DX are indistinguishable. Moreover, the range where the distance between the QWs centers is shorter than their widths is physically meaningless.

Setting $i = f = |\mathbf{Q}, S, \mathbf{Q}, S'\rangle$ states at a given point of the energy dispersion branches, one calculates the effective dipolaritonic interaction constants α_1 and α_2 responsible for frequency shifting of dipolaritonic luminescence due to interaction between dipolaritons with the same (α_1) and opposite (α_2) spins, as quantum averages (3.20):

$$\begin{aligned} \alpha_1 &= |c_{\text{DX}}(Q, V)|^4 V_{\text{DX,DX}}^{+1,+1} + |c_{\text{IX}}(Q, V)|^4 V_{\text{IX,IX}}^{+1,+1} + 4|c_{\text{DX}}(Q, V)|^2 |c_{\text{IX}}(Q, V)|^2 V_{\text{DX,IX}}^{+1,+1}, \\ \alpha_2 &= |c_{\text{IX}}(Q, V)|^4 V_{\text{IX,IX}}^{+1,-1}. \end{aligned} \quad (3.25)$$

Figure 3.8 presents the results of the numerical calculation of these constants throughout the three dipolaritonic branches in dependence on the applied bias. Note that $\alpha_{1(2)}$

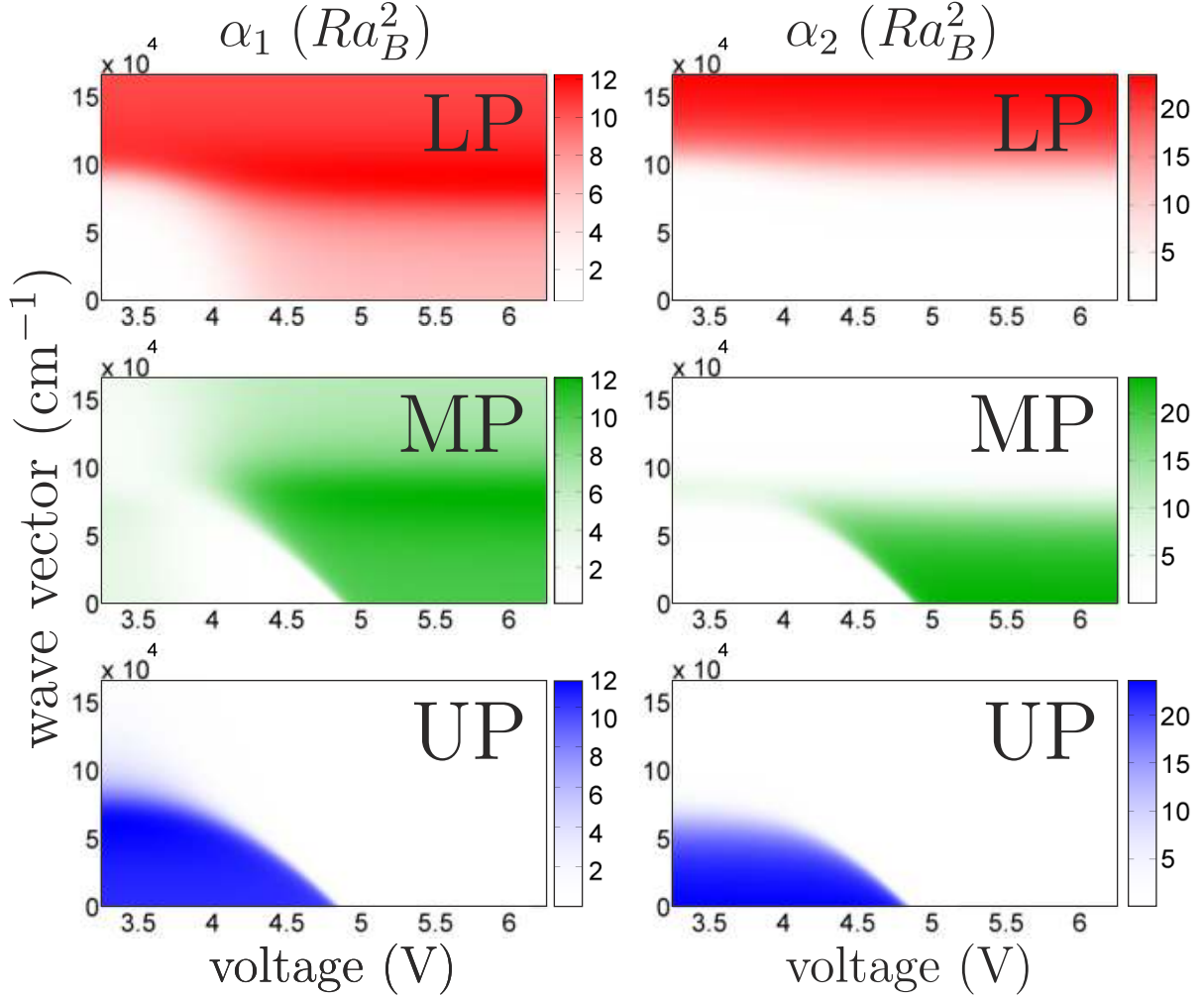


Figure 3.8: Interaction constants responsible for the blueshift and the bistability of pumped dipolariton states calculated in Born approximation. Left and right columns correspond to α_1 and α_2 , while the three rows correspond to LP, MP and UP dipolariton branches. The voltage and wave-vector dependences are due to the variation of Hopfield coefficients. From Nalitov et al. (2014) [29].

reflects blueshift of photoluminescence in a particular circular polarization due to optical pumping with the same(opposite) circular polarization.

All listed interaction constants are positive, therefore, the dipolariton scattering matrix elements (3.22) obtained in this section only describe repulsive interactions. In order to include the dipolariton attraction in our model we continue the expansion of the interactions to the second order.

3.2.3 Dipolariton scattering: Second order correction

Second order corrections to the interaction matrix elements are important for scattering of two dipolaritons with opposite spins in the region of voltages and momenta, where the IX fraction of either initial or final state are small and so is the first order matrix element.

This condition can be satisfied for the voltages where $|E_I - E_D| \gg J$ and excitonic modes are uncoupled. The IX state in this case may be excluded from the consideration and dipolariton reduces to conventional polariton. One may expect the change of sign of the singlet interaction parameter α_2 at the point where the first and the second order contributions become comparable.

Scattering of two polaritons with opposite spins has been recently studied theoretically [74] and experimentally [79]. In particular, the reference [79] reports a strong attraction of singlet lower branch polariton pairs depending on the energy detuning between the DX and cavity modes.

Generalization of reference [74] results to the case of the lower branch dipolaritons with the expression for the correction to the scattering matrix element in the second order of the perturbation theory [85]:

$$V_{f \leftarrow i}^{(2)\uparrow\downarrow} = \sum_m \frac{\langle f | \hat{V} | m \rangle \langle m | \hat{V} | i \rangle}{E_i - E_m} = \sum_m \frac{\langle \mathbf{Q}_f, +1; \mathbf{Q}'_f, -1 | \hat{V} | m \rangle \langle m | \hat{V} | \mathbf{Q}_i, +1; \mathbf{Q}'_i, -1 \rangle}{E_i - E_m} \quad (3.26)$$

where m enumerates all intermediate states of two electrons and two holes playing the role of the interaction mediator. Their energies E_i and E_f coincide due to the elasticity of the scattering, while the energy distance between them and the intermediate states must be large enough so that $|E_i - E_{int}| \ll V_{f \leftarrow i}^{(2)}$ for the applicability of the perturbation theory.

Intermediate states representing two dipolaritons with opposite spins are coupled with initial and final states by spin-conserving dipole-dipole scattering and result in a second order correction to the repulsion. On the contrary, states formed by two "dark" excitons $|\mathbf{Q} + \mathbf{P}, +2; \mathbf{Q}' - \mathbf{P}, -2\rangle$ are coupled to dipolariton pair states $|\mathbf{Q}, +1; \mathbf{Q}', -1\rangle$ via virtual fermion exchange. Terms with such intermediate states give negative contribution to the interaction potential exceeding the first order repulsion in absolute value. The same applies to the contribution coming from biexcitonic intermediate states. It becomes important in the case of polaritonic Feshbach resonance [86], when the dipolariton pair energy coincides with the biexciton energy and expression (3.26) diverges. If polariton states are far from the bi-exciton and dark exciton resonance, both terms gives qualitatively the same type contributions. Then, in order to simplify the calculations, one may neglect biexciton states contribution and focus on the contribution of dark exciton states.

Due to the electron tunneling through the barrier, the dark IX and DX states are coupled and form two anti-crossing branches LD and UD plotted with dashed lines in Figure 3.5. Direct and indirect fractions $d_D^{\text{LD(UD)}}$ and $d_I^{\text{LD(UD)}}$ of the dark branches, obtained by diagonalization of the Hamiltonian 3x3 matrix form, introduced in Chapter 1, with $\Omega = 0$, are independent of Q due to equal IX and DX effective masses. Similarly to the previous subsection, we derive the following:

$$V_{f \leftarrow i}^{(2)\uparrow\downarrow} = \sum_{i,j,k,l=IX,DX}^{m,n=LD,UD} C_{i,j}^{k,l} D_{i,j,k,l}^{m,n} \sum_{\mathbf{P}} \frac{V_{k,l}^{\text{exch}}(P) V_{i,j}^{\text{exch}}(P)}{-\Delta_{m,n} - \hbar^2 P^2 / M_X},$$

where $D_{i,j,k,l}^{m,n}(V) = d_i^m(V) d_j^n(V) d_k^m(V) d_l^n(V)$ and $\Delta_{m,n}(V) = E_m(V) + E_n(V) - E_i$. Here, once again the dependence of the virtual fermion exchange matrix elements $V_{i,j}^{\text{exch}}(P)$ on the dipolariton momenta $Q \ll a_B$ are neglected, although the virtual transferred

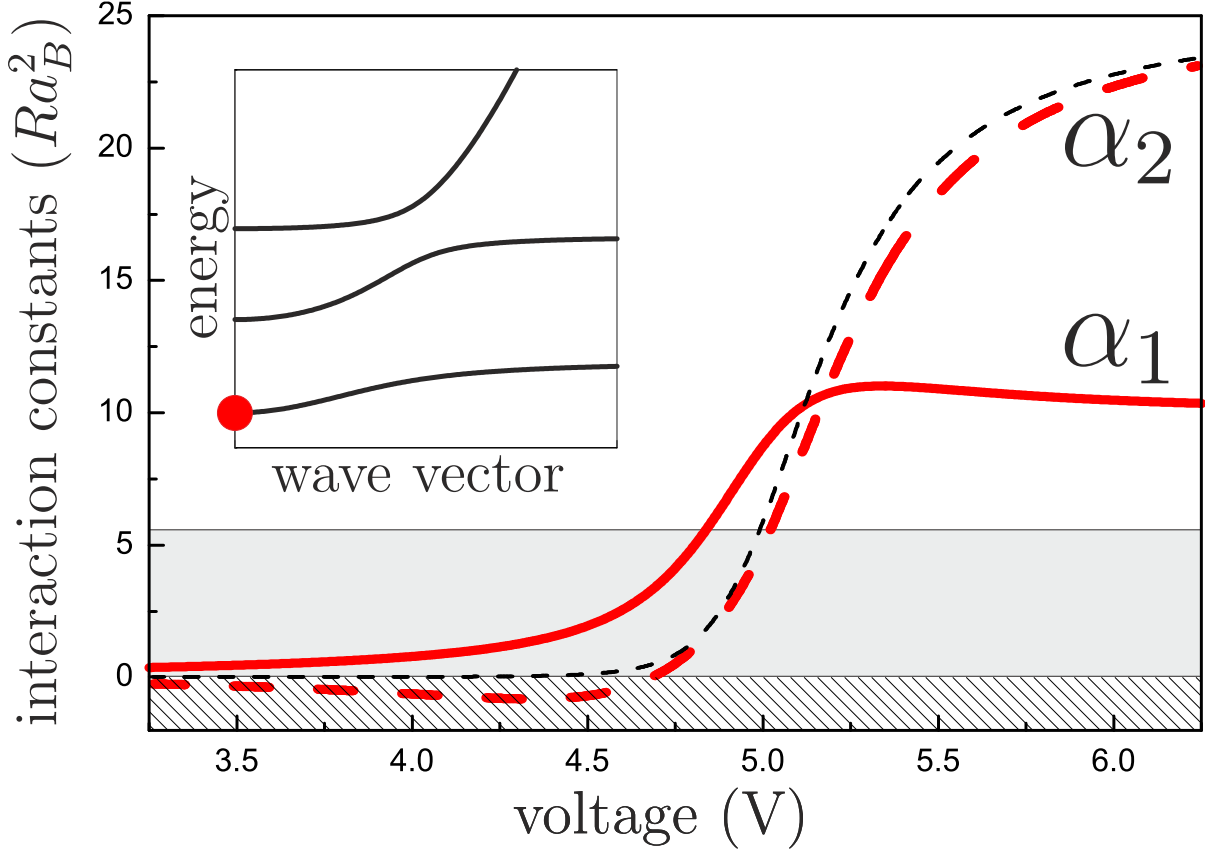


Figure 3.9: Effective interaction parameters responsible for blueshift, bistability and polarization of the ground dipolariton state (sketched in the inset), calculated in the second order of the perturbation theory, are plotted in red. Interaction parameter α_2 , describing interaction potential of two dipolaritons with opposite spins, changes sign with voltage and even exceeds α_1 , the one describing two dipolaritons with aligned spins. Grey(hatched) area represent possible values of α_1 (α_2) for conventional polaritons. The result of the first order calculation of α_2 is plotted with black dashed line for comparison. From Nalitov et al. (2014) [29].

momentum \mathbf{P} , which spans over the whole reciprocal space, is kept. Furthermore, the terms where $i = j = \text{IX}$ and $k = l = \text{IX}$, representing the next order correction to the IX repulsive contribution, are omitted. The virtual exchange matrix elements read:

$$\begin{aligned}
 V_{\text{IX,DX}}^{\text{exch}}(P) &= [\langle 0, +1 |_{\text{IX}} \otimes \langle 0, -1 |_{\text{DX}}]_a \hat{V} [| \mathbf{P}, -2 \rangle_{\text{IX}} \otimes | -\mathbf{P}, +2 \rangle_{\text{DX}}]_a, \\
 V_{\text{DX,DX}}^{\text{exch}}(P) &= [\langle 0, +1 |_{\text{DX}} \otimes \langle 0, -1 |_{\text{DX}}]_a \hat{V} [| \mathbf{P}, -2 \rangle_{\text{DX}} \otimes | -\mathbf{P}, +2 \rangle_{\text{DX}}]_a \\
 &\quad + [\langle 0, +1 |_{\text{DX}} \otimes \langle 0, -1 |_{\text{DX}}]_a \hat{V} [| \mathbf{P}, +2 \rangle_{\text{DX}} \otimes | -\mathbf{P}, -2 \rangle_{\text{DX}}]_a.
 \end{aligned}$$

Note that the two terms of the latter correspond to electron and hole exchange, contrary to the IX-DX case, where only the hole exchange is possible. Both matrix elements are integrated numerically as functions of the transferred momentum [49, 45] and vanish at $P > a_B/2$.

Substituting the two-particle ground dipolariton state as both i and f into Eqs. (3.21,3.26), one calculates the effective interaction constants for the ground state. The

results of this calculation are plotted in Figure 3.9. One may observe that α_2 is changing sign at a particular voltage, similarly with the case of resonant interaction with the bi-exciton resonance [79, 86], which has the disadvantage of inducing strong losses. Here, the mechanism is the increase of the mixing with the IX state which does not add any losses to the dipolarion. However, the whole system can be affected by the large intrinsic losses of the dipolaritonic states, induced by the presence of the metallic contacts and doped mirrors. A second remarkable point occurs at a slightly larger voltage, when α_2 and α_1 become equal. In case of a dipolariton condensation, this boundary corresponds to a transition between linearly and circularly polarized states [79] which can therefore be tuned, simply by changing the applied voltage.

3.2.4 Polarization inversion switching

OPO spin kinetics strongly depends on the type of polariton-polariton interaction. Polarization of photons, emitted from the signal state once the OPO turns on, is defined by the one of pumping and two interaction constants α_1 and α_2 describing parametric scattering of a pair of dipolaritons with aligned and anti-aligned spins respectively. In the particular case of linearly polarized pumping, the signal linear polarization degree is expressed by a simple relation, following from Eq. (3.13) [72]:

$$P_{lin,s} = \frac{\alpha_1 \alpha_2}{\alpha_1^2 + \alpha_2^2} P_{lin,p}, \quad (3.27)$$

where $P_{lin,p}$ is the linear polarization of the optical pumping. The sign of $P_{lin,s}$ and thus the orientation of the signal polarization plane are therefore determined by the relative sign of the interaction parameters α_1 and α_2 describing parametric scattering of dipolaritons with aligned and opposite spins.

To calculate them accounting for the second order correction one substitutes the pump, signal and idler dipolariton states into Eqs.(3.21,3.26):

$$\begin{aligned} \alpha_1 &= c_{DX}^2(Q_p, V) c_{DX}(Q_s, V)^* c_D(Q_i, V)^* V_{DX,DX}^{+,+1} + c_{IX}^2(Q_p, V) c_{IX}(Q_s, V)^* c_{IX}(Q_i, V)^* V_{IX,IX}^{+,+1} \\ &\quad + 2c_{IX}(Q_p, V) c_{DX}(Q_p, V) [c_{DX}(Q_s, V)^* c_{IX}(Q_i, V)^* + c_{DX}(Q_s, V)^* c_{IX}(Q_i, V)^*] V_{DX,IX}^{+,+1}, \\ \alpha_2 &= c_{IX}^2(Q_p, V) c_{IX}(Q_s, V)^* c_{IX}(Q_i, V)^* V_{IX,IX}^{+, -1} \\ &\quad + \sum_{\substack{m,n=LD,UD \\ i,j,k,l=IX,DX}} c_i(Q_p, V) c_j(Q_p, V) c_k(Q_s, V)^* c_l(Q_i, V)^* \\ &\quad \times d_i^m(V) d_j^n(V) d_k^m(V) d_l^n(V) \sum_{\mathbf{P}} \frac{V_{k,l}^{\text{exch}}(P) V_{i,j}^{\text{exch}}(P)}{-\Delta_{m,n} - \hbar^2 P^2 / M_X}, \end{aligned} \quad (3.28)$$

The results of this calculation are plotted in Figure 3.10 for LP, MP and interbranch scattering configurations. Notably, the following situations may be achieved by voltage variation for different OPO configurations: (i) $\alpha_2 < 0$, linear polarization inversion is on; (ii) $0 < \alpha_2 < \alpha_1$ and (iii) $\alpha_2 > \alpha_1$, linear polarization inversion is off. Moreover, as can be seen in Figure 3.10, in a certain range of voltages, the dipolaritonic OPO interaction constant exceeds the theoretically achievable value of $\alpha_1 = 6Ra_B^2$ for conventional microcavity polaritons [74].

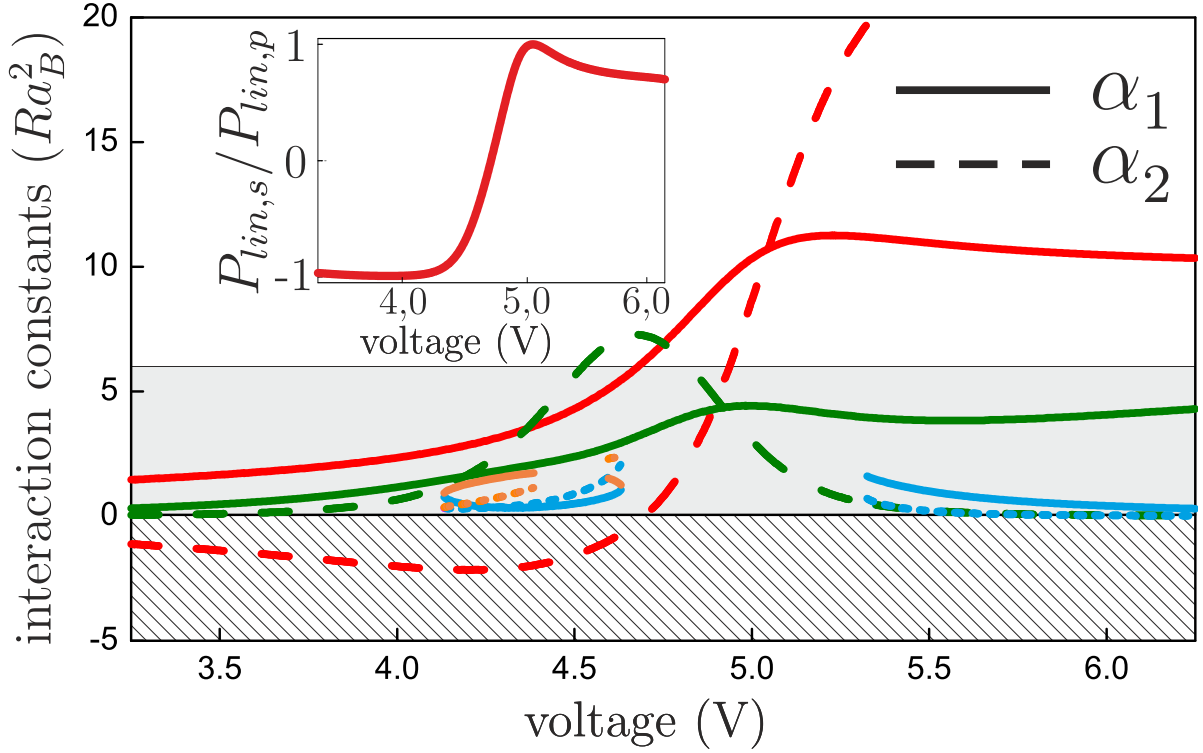


Figure 3.10: Interaction constants calculated for dipolariton parametric scattering in the second order of the perturbation theory. Solid lines represent interaction between the dipolaritons with the same spin (α_1), dashed lines are for dipolaritons with opposite spins (α_2). Grey (hatched) area limits the possible values of α_1 (α_2) for conventional microcavity polaritons. Both LP and MP configurations have a range of voltages where $\alpha_2 > \alpha_1$. In the LP case, α_2 is changing sign due to variation of the energy detuning and dipolariton oscillator strength. The inset shows the relation between linear polarization degrees of signal emission and optical pumping in the most relevant case of LP parametric scattering. From Nalitov et al. (2014) [29].

Substitution of the calculated interaction constants into the relation (3.27) finally gives the dependence of the signal linear polarization degree on the applied bias for the case of full linear polarization of the pumping ($P_{lin,p} = 1$), plotted in the inset of Figure 3.10. It has a narrow switching region from negative to positive values in the vicinity of the crossing point of the three modes, where α_2 value crosses zero. Realistically, the absolute value of the signal polarization degree is lowered by spin relaxation processes. However, the main result is that the orientation of the signal emission polarization plane may be switched between the one of the optical pump and the one orthogonal to it.

In conclusion, the calculated spin-dependent interaction parameters can be one order of magnitude larger than for conventional polaritons. By tuning the applied voltage, the interaction parameter α_2 between dipolaritons with opposite spin changes sign and can become larger than α_1 – the interaction parameter between dipolaritons having the same spin.

This shows that dipolaritons are promising particles for spin-optronic applications. In particular, a dipolaritonic OPO scheme has a very low threshold due to the large values of the interaction parameters. It offers the possibilities of interbranch parametric scattering. The flipping of the sign of the singlet interaction α_2 parameter allows the on-demand linear polarization inversion switching and polarization degree control by the applied bias.

3.3 Conclusion

The two works overviewed in this chapter are united with the common topic of the optical parametric oscillator (OPO) [73, 29]. Section 1 covers our collaborative attempt with experimentalists to explain specific behaviour of polarization inversion effect of an OPO in presence of one-dimensional trap potential. In particular, linear polarization plane of the OPO signal rotates twice faster than that of the pump: while the latter makes a full circumrotation, signal polarization plane makes two. Two independent approaches were used to account for the trap potential effect on parametric scattering, and both qualitatively reproduced the observations.

The second work is a proposal of a novel OPO device based on dipolaritons in a special type of cavities. Dipolaritons were proven to provide at least one order of magnitude stronger parametric scattering, which reduces potential threshold pump power of the device. Importantly, parametric scattering interaction parameters, as well as the polariton band structure, depend on the electric bias applied to cavity contacts. We have shown that the singlet configuration parametric scattering may be tuned from attractive to repelling with changing the bias. This property may be used for fast voltage controlled signal switching between two perpendicular linear polarizations.

Chapter 4

Spin dynamics and topological effects in microcavity pillar structures

The present chapter is devoted to the study of polariton spin physics in cavity superstructures, based on planar microcavities. In particular, pillar cavity lattices are considered for definiteness, although the same conclusions hold for other realizations of in-plane potentials for polaritons. This type of structures present interest as a platform for simulation of bosonic analogs of electron states and bands in molecules and solids. We concentrate here on the effects related to the effective spin-orbit coupling (SOC) for cavity polaritons, which is due to the TE-TM splitting, inherited by pillar structures from planar microcavities. Its strength may be controlled by tuning the Bragg reflectors and cavity parameters, and generally exceeds that of SOC acting on the QW exciton component of polaritons.

The first Section introduces basic properties of the effective SOC in microcavity pillar structures, starting from polariton molecules and proceeding to polariton graphene - a honeycomb lattice of overlapping pillar cavities. Some of consequences of the effective SOC properties, including peculiar behaviour of the optical spin Hall effect (OSHE), which may be evidenced in experiment, are demonstrated as well.

The second Section is focused on one particular implication of the SOC on the spin dynamics in polariton graphene. It is demonstrated that in presence of sufficiently strong external magnetic field the polariton graphene band structure resembles that of a \mathbb{Z} topological insulator. This yields a very specific behaviour of polaritons on the edges of the polariton graphene. Polariton edge states are propagating along the edge and protected from both scattering into the bulk and backscattering. They only have one allowed propagation direction governed by the magnetic field direction.

4.1 Effective spin-orbit interaction

The splitting of TE and TM linearly polarized photonic confined modes in a microcavity results in a coupling between the polariton pseudospin and momentum, or an effective spin-orbit interaction. In planar microcavities it manifests itself in the optical spin Hall effect [25]. The present chapter is, however, devoted to the description of more sophisticated microcavity pillar structures, etched out of planar microcavities. Spin-orbit interaction properties are strongly modified in this type of structures due to the specific geometry.

Pillar microcavities are characterized by size-quantized polariton states because of the in-plane confinement of the photonic mode. In this sense they represent photonic "atoms" with discrete spectra. Placed sufficiently close to each other, they form polariton "molecules" and even "crystals" due to the overlapping of the photonic modes in the neighbouring pillars. Contrary to the real molecules, the photonic ones may have arbitrary geometry in two dimensions. Basic types of polariton molecules and the effect of the photonic spin-orbit interaction on their eigenstates are introduced in Subsection 1. Polaritons in these structures simulate the electronic subsystem of real molecules and solids, with the possibility of direct optical probing of any state. In particular, single polariton dispersion in polariton graphene reproduces that of real graphene, a two-dimensional honeycomb lattice of carbon atoms [87]. This includes conical dispersion law in the vicinity of the touching points of the conduction and valence bands. Polaritons in this region of the reciprocal space behave like ultra-relativistic Dirac particles.

The present section is organized in the following way. The tight-binding approximation, which is used later for description of polariton graphene, is introduced on a simple example of polariton molecules in Subsection 1. Polariton benzene [88] is considered in Subsection 2. The polariton graphene effective Hamiltonian, accounting for SOC, is constructed in Subsection 3. The energy dispersion law, obtained with diagonalization of the effective Hamiltonian, is analyzed in Subsection 4. In particular, a peculiar transition of the band structure topology is obtained. Finally, the effective SOC field is derived and developed in the vicinity of the Dirac points in Subsection 5.

4.1.1 Polariton molecules

A microcavity pillar contains a discrete spectrum of photonic modes coupled to excitons which, in the strong coupling case, result in size-quantized polariton states. The lowest energy mode is axially symmetric and twice degenerate in polariton spin. The higher modes are characterized with quantized non-zero angular momenta. Each pillar thus can be treated as a two-dimensional polaritonic atom. If placed sufficiently close, microcavity pillars form coupled polariton modes and represent molecules in this sense.

The simplest case of a polariton molecule is a pair of overlapping microcavity pillars [89]. The localized polariton states overlap and form bonding and anti-bonding states, evidenced by photoluminescence spectra, shown in Fig. 4.1. A conventional way to describe the coupling between the localization centers is the tight-binding approach. It is based on the perturbation theory, with polariton states localized in each pillar taken as the zero approximation, and polariton tunneling between the pillars as the perturbation. Below, the ground polariton state with energy E_0 is considered by default and only the tunneling between the nearest neighbours is introduced. For simplicity, all pillars are assumed to be equal and axially symmetric, therefore, the ground polariton states in all pillars are degenerate.

To construct the Hamiltonian, we take into account the TE-TM splitting. It acts as an effective magnetic field, acting on propagating polariton spin and thus entering the nondiagonal Hamiltonian matrix elements. It can also be treated by assigning different effective masses for polaritons polarized longitudinally (m_L) and transversely ($m_T > m_L$) to their wave vectors.

The consequence of the action of the TE-TM splitting on the simplest polariton

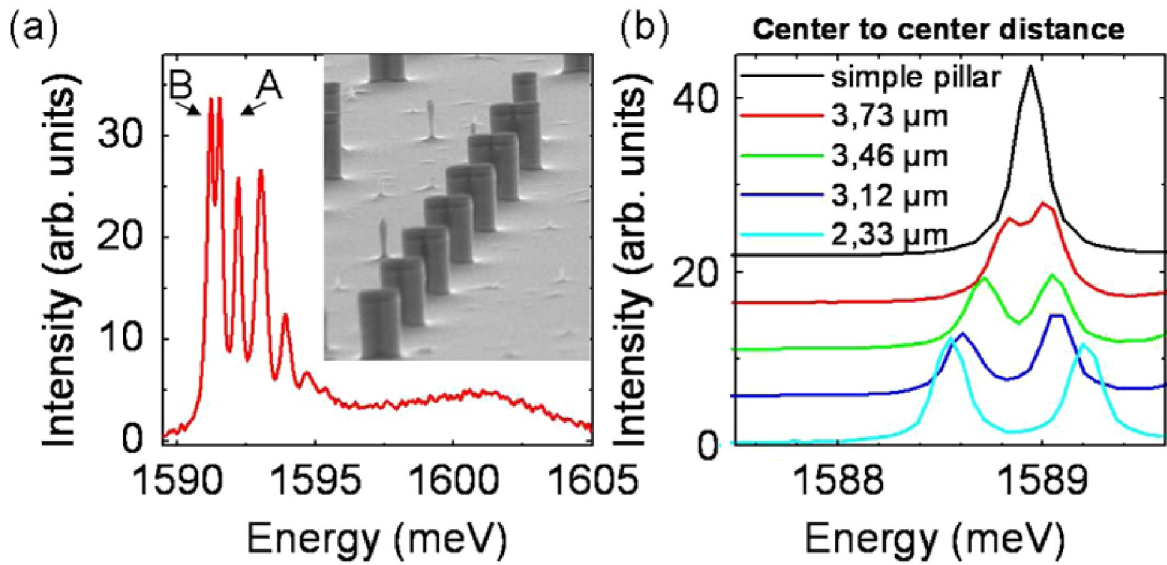


Figure 4.1: A photoluminescence experiment, demonstrating the coupling of the polariton modes localized in the pillars. (a) Emission spectrum measured on a single molecule at low excitation power (pillar diameter $d = 4 \mu\text{m}$ and the distance between the centers of pillars $d_{CC} = 3.73 \mu\text{m}$); A and B indicate the binding and antibinding states, respectively. Inset: Scanning electron micrograph of an array of pillars and molecules. (b) Emission spectra measured on a $4 \mu\text{m}$ round micropillar (black line) and on photonic molecules with $d = 4 \mu\text{m}$ and various values of d_{CC} . From Galbiati et al. (2012) [89]

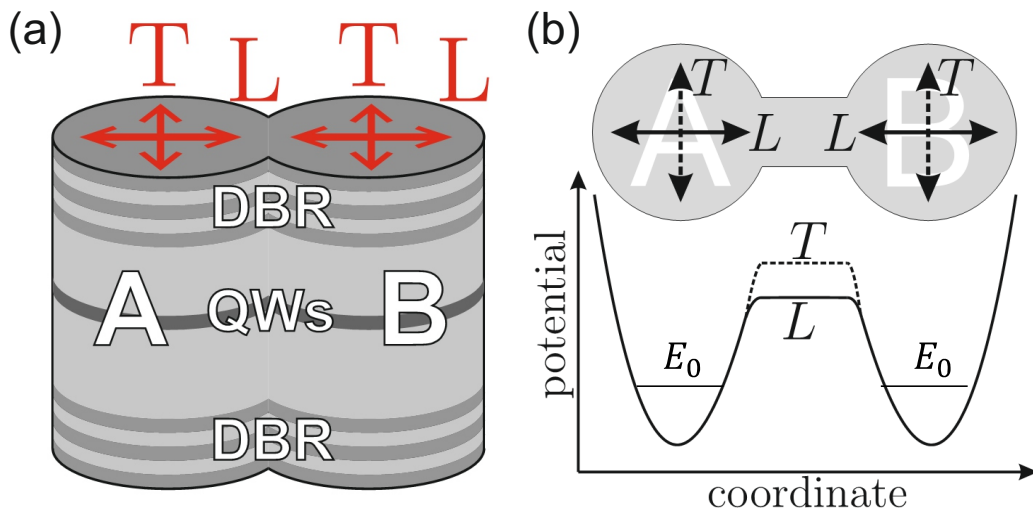


Figure 4.2: (a) A scheme of the simplest polariton molecule - a pair of overlapping pillar microcavities. The basis of linearly polarized polariton modes, localized in each cavity, is chosen according to the axis between the pillar centers. (b) A sketch of effective potential for polaritons. Potential barrier dependence on polarization is due to TE-TM coupling.

molecule, consisting of A and B pillars, is the dependence of the tunneling probability on polarization. The potential barrier due to the size quantization at the narrow junction between the pillars for a given polarization may be estimated as $V_{L(T)} = \pi^2 \hbar^2 / 2m_{L(T)} w^2$, where w is the junction width. Note that the barrier height depends on the mass of the same polarization, but in the direction, orthogonal to the axis between the pillars. For the state $|A, L(T)\rangle$, localized in the pillar "A" and having $L(T)$ polarization (see Fig. 4.2), the wavefunction tail in the pillar "B" is determined by tunnel extinction coefficient $\kappa_{L(T)} = \hbar^{-1} \sqrt{2m_{L(T)}(V_{T(L)} - E)}$. Therefore, we find that the nondiagonal blocks of the Hamiltonian matrix have different matrix elements $-J_{L,T}$, $J_L > J_T$ at their diagonals, whose values depend on the overlaps of corresponding wavefunctions. The off-diagonal terms are zero, because all sources of spin conversion other than LT splitting are neglected. In the basis of states $|A, L\rangle$, $|A, T\rangle$, $|B, L\rangle$ and $|B, T\rangle$ the Hamiltonian therefore reads:

$$H_{AB} = - \begin{pmatrix} 0 & 0 & J_L & 0 \\ 0 & 0 & 0 & J_T \\ J_L & 0 & 0 & 0 \\ 0 & J_T & 0 & 0 \end{pmatrix}. \quad (4.1)$$

A transition to the basis of circularly polarized polaritons $|A, +\rangle$, $|A, -\rangle$, $|B, +\rangle$, $|B, -\rangle$, where the polarization state $|\pm\rangle = |x\rangle \pm i|y\rangle$ is defined with reference to x , y axes, only affects nondiagonal blocks of the Hamiltonian (4.1):

$$H_{AB} = - \begin{pmatrix} 0 & 0 & J & \delta J e^{-2i\varphi} \\ 0 & 0 & \delta J e^{2i\varphi} & J \\ J & \delta J e^{-2i\varphi} & 0 & 0 \\ \delta J e^{2i\varphi} & J & 0 & 0 \end{pmatrix}, \quad (4.2)$$

where $J = (J_L + J_T)/2$, $\delta J = (J_L - J_T)/2$ and φ is the angle between AB and x axes.

The diagonalization of the Hamiltonian (4.2) gives the eigenstates of the polariton molecule. In the absence of the TE-TM splitting ($\delta J = 0$) the eigenstates are double degenerate pairs of symmetric and anti-symmetric polariton states. Effective SOC therefore lifts the degeneracy for both binding and anti-binding states and splits them by $2\delta J$.

Estimations of J may be made from energy splitting between bonding and anti-bonding states of a single polariton molecule (see Fig. 4.1(b)). It may be of the order of 10 meV for closely positioned microcavity pillars.

4.1.2 Polariton benzene

A peculiar nontrivial case of polariton molecules is a hexagon, composed by six overlapping pillars [88]. The same tight-binding formalism may be applied in this case to obtain polariton eigenstates composed of the ground pillar-pinned modes.

Let us consider the tunnel coupling between two neighboring pillars j and $j + 1$. In the basis of linearly polarized polariton single pillar states $|j, L/T\rangle$ tunneling is described by single polariton Hamiltonian matrix elements

$$\begin{aligned} J_L &= -\langle j, L | \hat{H} | j + 1, L \rangle, \\ J_T &= -\langle j, T | \hat{H} | j + 1, T \rangle, \end{aligned} \quad (4.3)$$

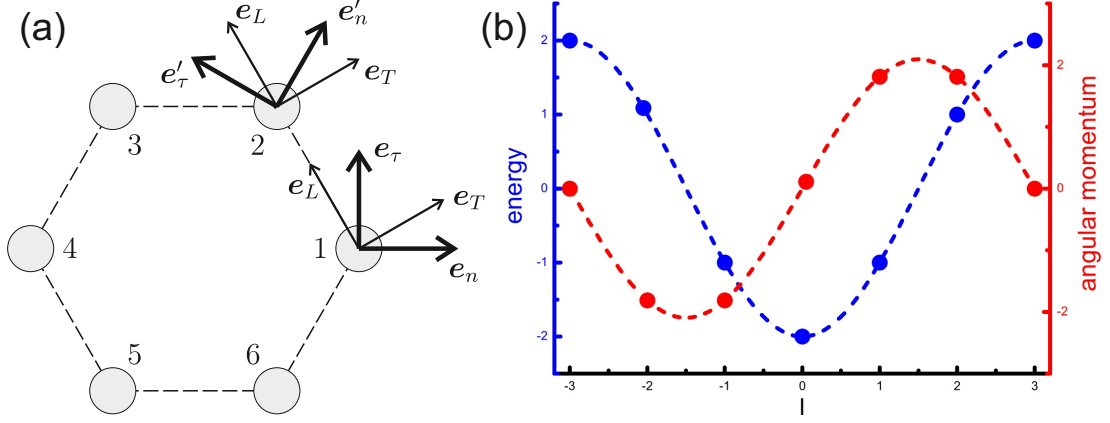


Figure 4.3: (a) A polariton benzene scheme with basis polarization vectors. (b) Eigenstate energy (blue, in units of J) and angular momentum (red, in arbitrary units) mean value versus total angular momentum quantum number. Dashed lines are given as guides for the eye.

while

$$\langle j, L | \hat{H} | j + 1, T \rangle = \langle j, T | \hat{H} | j + 1, L \rangle = 0. \quad (4.4)$$

In normal and tangential polarizations basis,

$$\begin{aligned} |j, n\rangle &= \frac{\sqrt{3}}{2} |j, T\rangle - \frac{1}{2} |j, L\rangle, \\ |j, \tau\rangle &= \frac{1}{2} |j, T\rangle - \frac{\sqrt{3}}{2} |j, L\rangle, \\ |j + 1, n\rangle &= \frac{\sqrt{3}}{2} |j + 1, T\rangle + \frac{1}{2} |j + 1, L\rangle, \\ |j + 1, \tau\rangle &= -\frac{1}{2} |j + 1, T\rangle + \frac{\sqrt{3}}{2} |j + 1, L\rangle, \end{aligned} \quad (4.5)$$

polariton benzene Hamiltonian reads

$$\hat{H} = \begin{pmatrix} E_n & 0 & -J_{nn} & J_{n\tau} & 0 & 0 & 0 & 0 & 0 & 0 & -J_{nn} & -J_{n\tau} \\ 0 & E_\tau & -J_{n\tau} & -J_{\tau\tau} & 0 & 0 & 0 & 0 & 0 & 0 & J_{n\tau} & -J_{\tau\tau} \\ -J_{nn} & -J_{n\tau} & E_n & 0 & -J_{nn} & J_{n\tau} & 0 & 0 & 0 & 0 & 0 & 0 \\ J_{n\tau} & -J_{\tau\tau} & 0 & E_\tau & -J_{n\tau} & -J_{\tau\tau} & 0 & 0 & 0 & 0 & 0 & 0 \\ 0 & 0 & -J_{nn} & -J_{n\tau} & E_n & 0 & -J_{nn} & J_{n\tau} & 0 & 0 & 0 & 0 \\ 0 & 0 & J_{n\tau} & -J_{\tau\tau} & 0 & E_\tau & -J_{n\tau} & -J_{\tau\tau} & 0 & 0 & 0 & 0 \\ 0 & 0 & 0 & 0 & -J_{nn} & -J_{n\tau} & E_n & 0 & -J_{nn} & J_{n\tau} & 0 & 0 \\ 0 & 0 & 0 & 0 & J_{n\tau} & -J_{\tau\tau} & 0 & E_\tau & -J_{n\tau} & -J_{\tau\tau} & 0 & 0 \\ 0 & 0 & 0 & 0 & 0 & 0 & -J_{nn} & -J_{n\tau} & E_n & 0 & -J_{nn} & J_{n\tau} \\ 0 & 0 & 0 & 0 & 0 & 0 & J_{n\tau} & -J_{\tau\tau} & 0 & E_\tau & -J_{n\tau} & -J_{\tau\tau} \\ -J_{nn} & J_{n\tau} & 0 & 0 & 0 & 0 & 0 & 0 & -J_{nn} & -J_{n\tau} & E_n & 0 \\ -J_{n\tau} & -J_{\tau\tau} & 0 & 0 & 0 & 0 & 0 & 0 & J_{n\tau} & -J_{\tau\tau} & 0 & E_\tau \end{pmatrix}, \quad (4.6)$$

where

$$\begin{aligned}
J_{nn} &= \frac{1}{4}(3J_T - J_L), \\
J_{\tau\tau} &= \frac{1}{4}(3J_L - J_T), \\
J_{n\tau} &= \frac{\sqrt{3}}{4}(J_T + J_L).
\end{aligned} \tag{4.7}$$

To change the basis one may express normal and tangential polarization states in each pillar $|j, n\rangle$ and $|j, \tau\rangle$ in right and left circular polarization single pillar states:

$$\begin{aligned}
|j, n\rangle &= \frac{1}{\sqrt{2}} \left[\exp\left(-i\pi\frac{j-1}{3}\right) |j, +\rangle + \exp\left(i\pi\frac{j-1}{3}\right) |j, -\rangle \right] \\
|j, \tau\rangle &= \frac{1}{\sqrt{2}} \left[\exp\left(-i\pi\left(\frac{j-1}{3} + \frac{1}{2}\right)\right) |j, +\rangle + \exp\left(i\pi\left(\frac{j-1}{3} + \frac{1}{2}\right)\right) |j, -\rangle \right]
\end{aligned} \tag{4.8}$$

via basis transition matrix

$$X_0 = \frac{1}{\sqrt{2}} \begin{pmatrix} 1 & 1 & 0 & 0 & 0 & 0 & 0 & 0 & 0 & 0 & 0 & 0 & 0 \\ -i & i & 0 & 0 & 0 & 0 & 0 & 0 & 0 & 0 & 0 & 0 & 0 \\ 0 & 0 & e^{-i\frac{\pi}{3}} & e^{i\frac{\pi}{3}} & 0 & 0 & 0 & 0 & 0 & 0 & 0 & 0 & 0 \\ 0 & 0 & e^{-i\frac{5\pi}{6}} & e^{i\frac{5\pi}{6}} & 0 & 0 & 0 & 0 & 0 & 0 & 0 & 0 & 0 \\ 0 & 0 & 0 & 0 & e^{-i\frac{2\pi}{3}} & e^{i\frac{2\pi}{3}} & 0 & 0 & 0 & 0 & 0 & 0 & 0 \\ 0 & 0 & 0 & 0 & e^{i\frac{5\pi}{6}} & e^{-i\frac{5\pi}{6}} & 0 & 0 & 0 & 0 & 0 & 0 & 0 \\ 0 & 0 & 0 & 0 & 0 & 0 & -1 & -1 & 0 & 0 & 0 & 0 & 0 \\ 0 & 0 & 0 & 0 & 0 & 0 & i & -i & 0 & 0 & 0 & 0 & 0 \\ 0 & 0 & 0 & 0 & 0 & 0 & 0 & 0 & e^{i\frac{2\pi}{3}} & e^{-i\frac{2\pi}{4}} & 0 & 0 & 0 \\ 0 & 0 & 0 & 0 & 0 & 0 & 0 & 0 & e^{i\frac{\pi}{6}} & e^{-i\frac{\pi}{6}} & 0 & 0 & 0 \\ 0 & 0 & 0 & 0 & 0 & 0 & 0 & 0 & 0 & 0 & e^{i\frac{\pi}{3}} & e^{-i\frac{\pi}{3}} & 0 \\ 0 & 0 & 0 & 0 & 0 & 0 & 0 & 0 & 0 & 0 & e^{-i\frac{\pi}{6}} & e^{i\frac{\pi}{6}} & 0 \end{pmatrix} \begin{matrix} 1^+ \\ 1^- \\ 2^+ \\ 2^- \\ 3^+ \\ 3^- \\ 4^+ \\ 4^- \\ 5^+ \\ 5^- \\ 6^+ \\ 6^- \end{matrix} \tag{4.9}$$

Let us now introduce a basis of many-pillar states with left and right circular polarizations:

$$|l\pm\rangle = \sum_{j=1}^6 \exp\left(i\frac{l(j-1)\pi}{3}\right) |j\pm\rangle, \tag{4.10}$$

where $l = 0, \pm 1, \pm 2, 3$, via transition matrix

$$X = \sqrt{6} \begin{pmatrix} 1 & 0 & 1 & 0 & 1 & 0 & 1 & 0 & 1 & 0 & 1 & 0 \\ 0 & 1 & 0 & 1 & 0 & 1 & 0 & 1 & 0 & 1 & 0 & 1 \\ 1 & 0 & e^{i\frac{\pi}{3}} & 0 & e^{i\frac{2\pi}{3}} & 0 & -1 & 0 & e^{-i\frac{2\pi}{3}} & 0 & e^{-i\frac{\pi}{3}} & 0 \\ 0 & 1 & 0 & e^{i\frac{\pi}{3}} & 0 & e^{i\frac{2\pi}{3}} & 0 & -1 & 0 & e^{-i\frac{2\pi}{3}} & 0 & e^{-i\frac{\pi}{3}} \\ 1 & 0 & e^{-i\frac{\pi}{3}} & 0 & e^{-i\frac{2\pi}{3}} & 0 & -1 & 0 & e^{i\frac{2\pi}{3}} & 0 & e^{i\frac{\pi}{3}} & 0 \\ 0 & 1 & 0 & e^{-i\frac{\pi}{3}} & 0 & e^{-i\frac{2\pi}{3}} & 0 & -1 & 0 & e^{i\frac{2\pi}{3}} & 0 & e^{i\frac{\pi}{3}} \\ 1 & 0 & e^{i\frac{2\pi}{3}} & 0 & e^{-i\frac{2\pi}{3}} & 0 & 1 & 0 & e^{i\frac{2\pi}{3}} & 0 & e^{-i\frac{2\pi}{3}} & 0 \\ 0 & 1 & 0 & e^{i\frac{2\pi}{3}} & 0 & e^{-i\frac{2\pi}{3}} & 0 & 1 & 0 & e^{i\frac{2\pi}{3}} & 0 & e^{-i\frac{2\pi}{3}} \\ 1 & 0 & e^{-i\frac{2\pi}{3}} & 0 & e^{i\frac{2\pi}{3}} & 0 & 1 & 0 & e^{-i\frac{2\pi}{3}} & 0 & e^{i\frac{2\pi}{3}} & 0 \\ 0 & 1 & 0 & e^{-i\frac{2\pi}{3}} & 0 & e^{i\frac{2\pi}{3}} & 0 & 1 & 0 & e^{-i\frac{2\pi}{3}} & 0 & e^{i\frac{2\pi}{3}} \\ 1 & 0 & -1 & 0 & 1 & 0 & -1 & 0 & 1 & 0 & -1 & 0 \\ 0 & 1 & 0 & -1 & 0 & 1 & 0 & -1 & 0 & 1 & 0 & -1 \end{pmatrix}^{-1} \begin{matrix} 0^+ \\ 0^- \\ +1^+ \\ +1^- \\ -1^+ \\ -1^- \\ +2^+ \\ +2^- \\ -2^+ \\ -2^- \\ 3^+ \\ 3^- \end{matrix} \quad (4.11)$$

Desired Hamiltonian in new basis ($|0\pm\rangle, |\pm 1\pm\rangle, |\pm 2\pm\rangle, |3\pm\rangle$) $\hat{H}' = X^{-1}X_0^{-1}\hat{H}X_0X$ has the following form:

$$\hat{H} = \begin{pmatrix} E_1 & 0 & 0 & 0 & 0 & 0 & 0 & \Delta_{1,8} & 0 & 0 & 0 & 0 \\ 0 & E_2 & 0 & 0 & 0 & 0 & 0 & 0 & \Delta_{2,8} & 0 & 0 & 0 \\ 0 & 0 & E_3 & 0 & 0 & 0 & 0 & 0 & 0 & 0 & 0 & \Delta_{3,12} \\ 0 & 0 & 0 & E_4 & \Delta_{4,5} & 0 & 0 & 0 & 0 & 0 & 0 & 0 \\ 0 & 0 & 0 & \Delta_{4,5} & E_5 & 0 & 0 & 0 & 0 & 0 & 0 & 0 \\ 0 & 0 & 0 & 0 & 0 & E_6 & 0 & 0 & 0 & 0 & \Delta_{6,11} & 0 \\ 0 & 0 & 0 & 0 & 0 & 0 & E_7 & 0 & 0 & \Delta_{7,10} & 0 & 0 \\ \Delta_{1,8} & 0 & 0 & 0 & 0 & 0 & 0 & E_8 & 0 & 0 & 0 & 0 \\ 0 & \Delta_{2,8} & 0 & 0 & 0 & 0 & 0 & 0 & E_9 & 0 & 0 & 0 \\ 0 & 0 & 0 & 0 & 0 & 0 & \Delta_{7,10} & 0 & 0 & E_{10} & 0 & 0 \\ 0 & 0 & 0 & 0 & 0 & \Delta_{6,11} & 0 & 0 & 0 & 0 & E_{11} & 0 \\ 0 & 0 & \Delta_{3,12} & 0 & 0 & 0 & 0 & 0 & 0 & 0 & 0 & E_{12} \end{pmatrix} \begin{matrix} 0^+ \\ 0^- \\ +1^+ \\ +1^- \\ -1^+ \\ -1^- \\ +2^+ \\ +2^- \\ -2^+ \\ -2^- \\ 3^+ \\ 3^- \end{matrix} \quad (4.12)$$

where

$$\begin{aligned} E_1 &= E_2 = E - 2J, \quad E_3 = E_4 = E_5 = E_6 = E - J, \\ E_7 &= E_8 = E_9 = E_{10} = E + J, \quad E_{11} = E_{12} = E + 2J, \\ \Delta_{1,8} &= -\Delta_E - \Delta_J, \quad \Delta_{2,8} = -\Delta_E - \Delta_J, \quad \Delta_{3,12} = -\Delta_E + \Delta_J, \\ \Delta_{4,5} &= -\Delta_E - 2\Delta_J, \quad \Delta_{6,11} = -\Delta_E + \Delta_J, \quad \Delta_{7,10} = -\Delta_E + 2\Delta_J, \\ E &= \frac{1}{2}(E_\tau + E_n), \quad J = \frac{1}{2}(J_L + J_T), \quad \Delta_E = \frac{1}{2}(E_\tau - E_n), \quad \Delta_J = \frac{1}{2}(J_L - J_T) \end{aligned} \quad (4.13)$$

As seen from the Hamiltonian matrix Eq. (4.12), all states with defined total angular momenta split in coupled pairs. Note that the coupling lifts the degeneracy between the states 4 and 5, 7 and 10 with orbital momenta absolute values 1 and 2 respectively. The degeneracies are defined by the time-reversal symmetry, which yields the angular momentum conservation. Time reversion inverts spins and angular momenta, therefore

pairs of states, which may be converted one into the other by changing signs of spins and orbital momenta, must have the same energy. Spin-orbit coupling does not break the time-reversal symmetry: it lifts the degeneracies, as the resulting split states are invariant under time reversion. On the contrary, time-reversal symmetry may be broken with external magnetic field, acting on polariton spin through the excitonic part.

This Hamiltonian can also be expressed in a form of operator acting on a spinor $[\Psi^+(j)\Psi^-(j)]^T$, where j plays a role of generalized integer coordinate, $j = 1..6$. For this we introduce the diagonal part of the Hamiltonian $\widehat{H}_0 = \widehat{H}(\Delta_E = \Delta_J = 0)$ and conventional operator of angular momentum \widehat{L} on this integer space. The eigenstates of H_0 have defined quantum number l and produce the basis of the Hamiltonian 4.12. Its eigenvalues E_l are

$$E_l = E - 2J \cos\left(\frac{\pi l}{3}\right). \quad (4.14)$$

While \widehat{L} has the same eigenstates as \widehat{H}_0 , while its eigenvalues have a different dependence on l :

$$\langle l|\widehat{L}|l\rangle \sim \frac{\partial E_l}{\partial l} = \frac{2\pi}{3}J \sin\left(\frac{\pi l}{3}\right). \quad (4.15)$$

Then the Hamiltonian 4.12 can be finally rewritten:

$$\widehat{H} = \widehat{H}_0 - \Delta_E \begin{pmatrix} 0 & e^{-2i\varphi_j} \\ e^{2i\varphi_j} & 0 \end{pmatrix} + \frac{\sqrt{3}\Delta_J}{\pi} \frac{1}{J} \left[\widehat{L}, \begin{pmatrix} 0 & e^{-2i\varphi_j} \\ e^{2i\varphi_j} & 0 \end{pmatrix} \right], \quad (4.16)$$

where $\varphi_j = \frac{j\pi}{3}$. Using spin operator $\hat{\mathbf{s}} = \boldsymbol{\sigma}$, where $\boldsymbol{\sigma}$ is the Pauli matrices vector, and conventional field $\boldsymbol{\Omega} = \cos(2\varphi_j)\mathbf{e}_x + \sin(2\varphi_j)\mathbf{e}_y$, we can rewrite the Hamiltonian:

$$\widehat{H} = \widehat{H}_0 - \Delta_E \boldsymbol{\Omega} \mathbf{s} - \frac{\sqrt{3}\Delta_J}{\pi} \frac{1}{J} \left[\boldsymbol{\Omega} \mathbf{s}, \widehat{L} \right] \quad (4.17)$$

Finally, if we express angular momentum operator as $\widehat{L} = [\hat{\mathbf{r}} \times \hat{\mathbf{p}}]$, the Hamiltonian reads

$$\widehat{H} = \widehat{H}_0 - \Delta_E \boldsymbol{\Omega} \mathbf{s} - \frac{\sqrt{3}\Delta_J}{\pi} \frac{1}{J} \left[\hat{\mathbf{A}}, \hat{\mathbf{p}} \right], \quad (4.18)$$

where

$$\begin{aligned} A_x &= \cos\varphi_j (\cos(2\varphi_j)s_x + \sin(2\varphi_j)s_y) \\ A_y &= -\sin\varphi_j (\cos(2\varphi_j)s_x + \sin(2\varphi_j)s_y), \end{aligned} \quad (4.19)$$

and \mathbf{p} has a meaning of operator of phase difference between neighbouring pillars.

4.1.3 Polariton graphene

A honeycomb lattice based on a patterned planar microcavity, similar to the one recently fabricated and studied [87], simulates graphene, a two-dimensional layer of Carbon atoms. The tight-binding approximation, as well as numerical solution of Schroedinger equation with honeycomb potential, were used to calculate the band structure of polariton graphene. The same model, however, can be applied to other physical realizations of

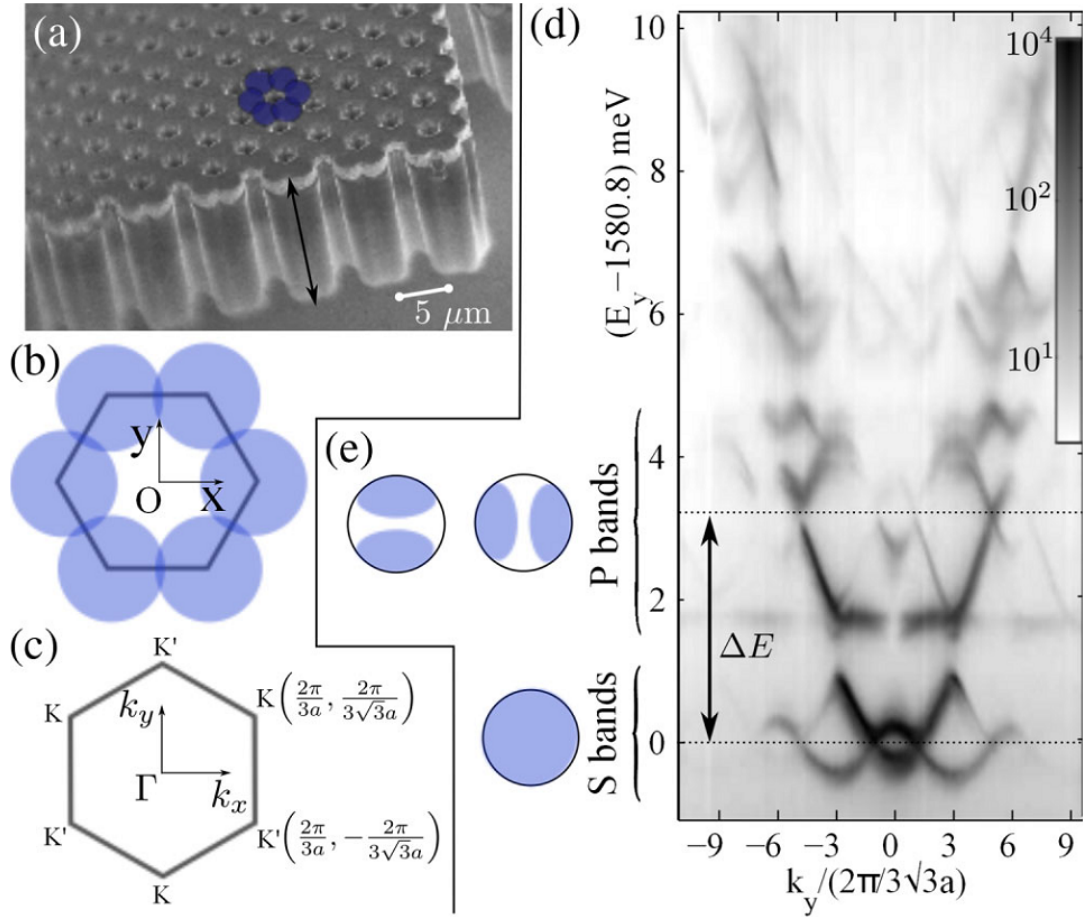


Figure 4.4: (a) Scanning electron microscope image of a corner of the microstructure. One hexagon of pillars is underlined with blue disks. The dark arrows show the growth axis of the cavity. The overlap between pillars is sketched in (b). (c) First Brillouin zone. (d) Measured momentum space energy resolved photoluminescence at $k_x = -2\pi/3a$ [line 0 in Fig. 2(a)], under nonresonant low-power excitation. (e) Sketch of the real space distribution of S and P modes in a single pillar. From Jacqmin et al. (2014) [87]

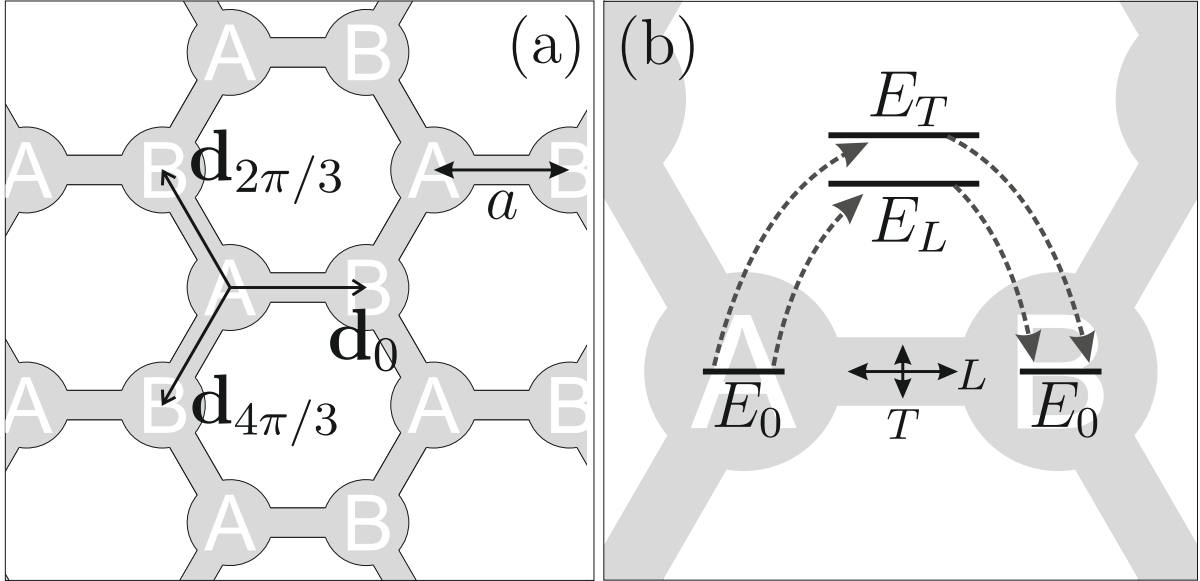


Figure 4.5: (color online) A schematic sketch of the tight-binding model. (a) Photon tunneling between microcavity pillars is described as photon propagation through "waveguide"-like links. (b) Polarization dependence of tunneling probability due to TE-TM energy splitting: L state which is polarized longitudinally to the "waveguide" link is closer in energy to the degenerate pillar-pinned states than the transversely-polarized state T , resulting in higher L -photon tunneling probability through the link.

honeycomb lattices, in optical and non-optical systems. Photons and exciton-polaritons behave in a similar way and our formalism applies to both strong coupling regime and an empty photonic cavity (without active layer).

We take a degenerate basis of $\sigma\pm$ polarized ground polariton states localized on each pillar of the lattice as a zeroth approximation for the tight-binding model and introduce the hopping of photons from a pillar to one of its nearest neighbors as a perturbation. The SOC appears due to the difference in the tunneling coefficients of the tight-binding Hamiltonian for light polarization longitudinal and transverse with respect to the junction between the pillars. This difference is described in Subsection 1 and the Hamiltonian of a cavity pillar pair (4.2) is used to construct the polariton graphene Hamiltonian.

The zeroth approximation of the model is the basis of σ polarized polariton states, localized on one of the pillars $\varphi^\sigma(\mathbf{r} - \mathbf{a}_i(\mathbf{b}_i))$, where $\sigma = \pm 1$ and $\mathbf{a}_i(\mathbf{b}_i)$ is the radius vector of the i th type-A(B) pillar. The general form of polariton wavefunction may be represented as a linear combination of the basis states

$$|\Psi(\mathbf{r})\rangle \equiv \sum_{i,\sigma} [c_{i,\sigma}^A |\varphi^\sigma(\mathbf{r} - \mathbf{a}_i)\rangle + c_{i,\sigma}^B |\varphi^\sigma(\mathbf{r} - \mathbf{b}_i)\rangle] \quad (4.20)$$

We assume a slight difference in the tunneling coefficients between two neighboring pillars for a polariton linearly polarized along and transverse to the axis between them (due to the TE-TM splitting, as discussed above):

$$\langle \varphi^{L(T)}(\mathbf{r} - \mathbf{a}_i) | \hat{H} | \varphi^{L(T)}(\mathbf{r} - \mathbf{a}_i - \delta_j) \rangle = -J_{L(T)}, \quad (4.21)$$

where δ_j vector links a type-A pillar to its j th neighbor, as shown in Figure 4.5. We further put the energy of the degenerate basis states to 0 and define the Hamiltonian non-diagonal matrix elements (see Eq. (4.2)):

$$\begin{aligned} H_j^{\sigma,\sigma} &\equiv \langle \varphi^\sigma(\mathbf{r} - \mathbf{a}_i) | \hat{H} | \varphi^\sigma(\mathbf{r} - \mathbf{a}_i - \delta_j) \rangle = -J, \\ H_j^{+,-} &\equiv \langle \varphi^+(\mathbf{r} - \mathbf{a}_i) | \hat{H} | \varphi^-(\mathbf{r} - \mathbf{a}_i - \delta_j) \rangle = -\delta J e^{ij\frac{2\pi}{3}}, \end{aligned} \quad (4.22)$$

where $J = (J_L + J_T)/2$ and $\delta J = (J_L - J_T)/2$. Note that presence of δJ results in a nonzero probability for a σ polarized polariton to tunnel to a neighboring pillar, simultaneously flipping its polarization. Moreover, the phase gained in such tunneling is different for each of the three tunneling directions.

Consequently multiplying the Schroedinger equation $\hat{H}\Psi = E\Psi$ on $\langle \varphi^\pm(\mathbf{r} - \mathbf{a}_n) |$ and $\langle \varphi^\pm(\mathbf{r} - \mathbf{b}_n) |$ and substituting the general form (4.21) with $c_{i,\sigma}^{A(B)} = c_\sigma^{A(B)}(\mathbf{k})e^{-i\mathbf{k}\mathbf{a}_i(\mathbf{b}_i)}$, we obtain a system of four coupled equations on the coefficients $c_\sigma^{A(B)}(\mathbf{k})$:

$$\sum_{j,\sigma} c_\sigma^{B(A)} e^{-i\mathbf{k}\delta_j} H_j^{+(-),\sigma} = E c_{+(-)}^{A(B)}, \quad (4.23)$$

which is evidently presented in a matrix equation form:

$$\begin{pmatrix} E_k & 0 & f_k J & f_k' \delta J \\ 0 & E_k & f_k'' \delta J & f_k J \\ f_k^* J & f_k'^* \delta J & E_k & 0 \\ f_k'^* \delta J & f_k^* J & 0 & E_k \end{pmatrix} \begin{pmatrix} c_+^A \\ c_-^A \\ c_+^B \\ c_-^B \end{pmatrix} = 0, \quad (4.24)$$

where $f_k = \sum_{j=0}^2 e^{-i\mathbf{k}\delta_j}$, $f_k' = \sum_{j=0}^2 e^{-i\mathbf{k}\delta_j + ij\frac{2\pi}{3}}$ and $f_k'' = \sum_{j=0}^2 e^{-i\mathbf{k}\delta_j - ij\frac{2\pi}{3}}$.

The polariton dispersion is obtained from the block determinant of the matrix M_k in the left-hand part of equation (4.24):

$$\det(M_k) = \det(\hat{E}_k^2 - \hat{F}_k^\dagger \hat{F}_k) = 0, \quad (4.25)$$

where \hat{E}_k and \hat{F}_k are the upper-left and the upper-right 2x2 blocks of M . Equation (4.25) presents a biquadratic equation on E , having a set of solutions:

$$E_k^2 = |f_k|^2 J^2 + \frac{|f_k'|^2 + |f_k''|^2}{2} \delta J^2 \pm \frac{\sqrt{(|f_k'|^2 - |f_k''|^2)^2 \delta J^4 + 4|f_k f_k'^* + f_k^* f_k''|^2 J^2 \delta J^2}}{2}. \quad (4.26)$$

Note that in absence of SOC $\delta J = 0$ and Eq. (4.26) is reduced to conventional equation on graphene dispersion law. The topology of the dispersion if analyzed in the following Subsection.

4.1.4 Trigonal warping and band topological transition

The energy band structure of polariton graphene reflects the general properties of honeycomb carbon layers. The reciprocal lattice also possesses the honeycomb symmetry, and the Brillouin zone may be chosen as a hexagon. Two nonequivalent points of the reciprocal space K and K' are then positioned in the corners of the Brillouin zone. In the

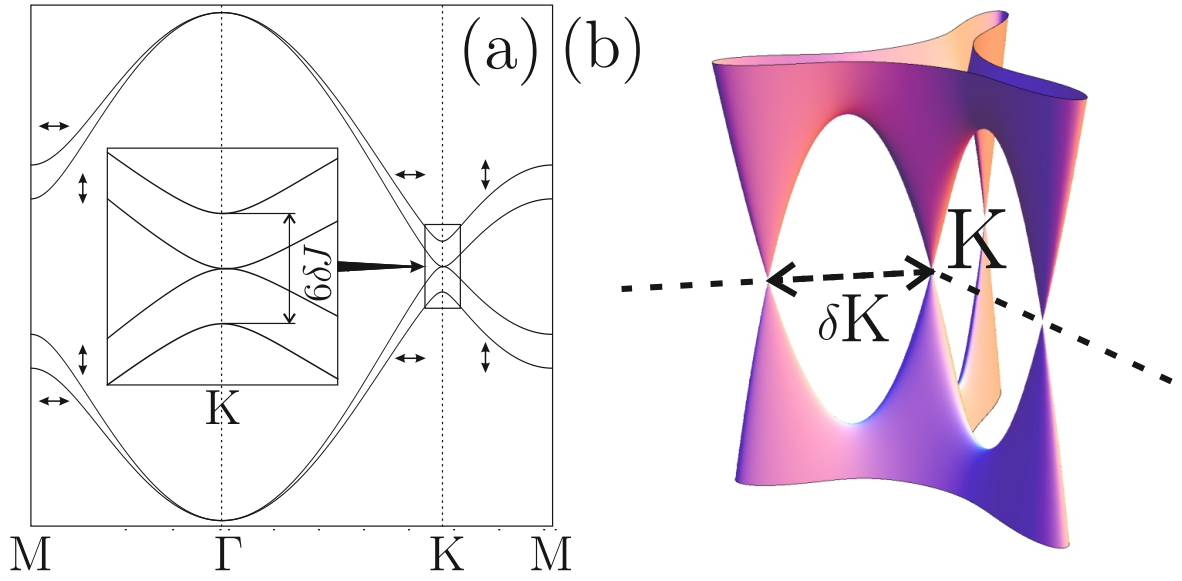


Figure 4.6: (a) Polariton energy dispersion plotted along the principal directions for $\delta J/J = 0.1$. (b) A further close-up on the band intersection (inset of (a)) demonstrating the band structure topology. Each Dirac cone is split in four, one of which stays at the corner of the Brillouin zone, and the other three are move along the Brillouin zone edges with increasing SOC strength $\delta J/J$. From Nalitov et al. (2015) [90]

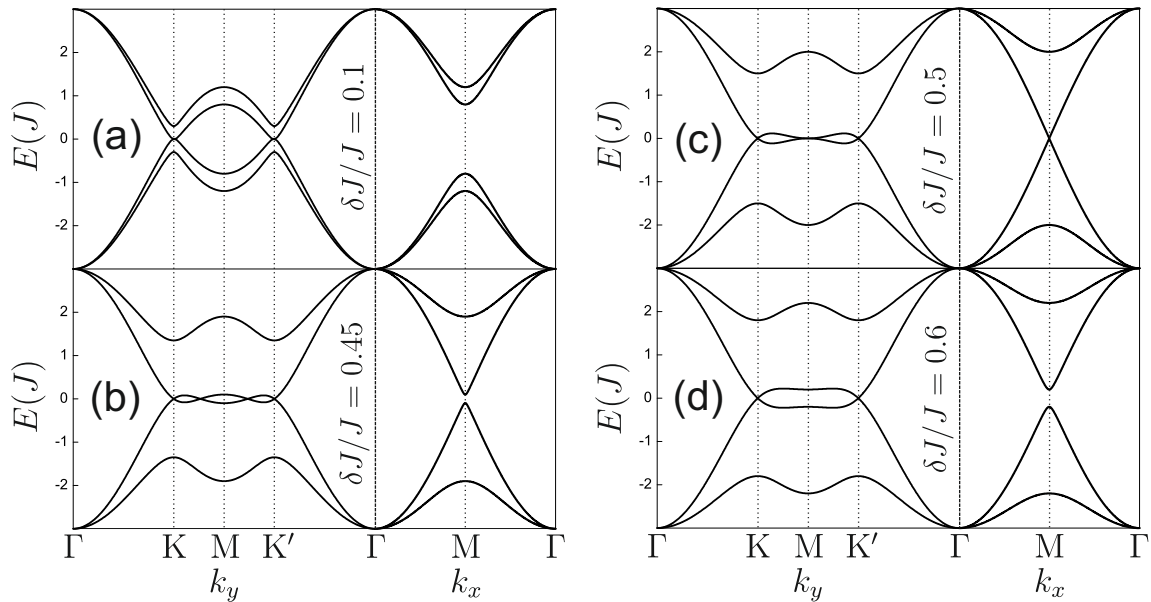


Figure 4.7: Topological transition of the polariton band structure. The energy dispersion is plotted along the principal directions for different values of the relation $\delta J/J$. The topological transition occurs at $\delta J/J = 0.5$.

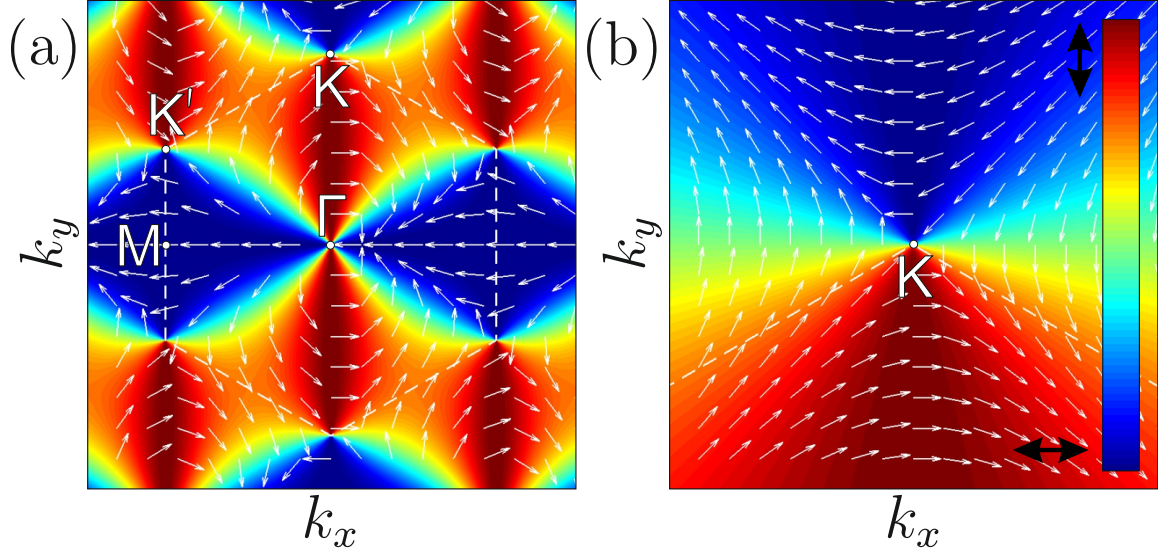


Figure 4.8: The eigenstate pseudospin map of the lowest energy dispersion branch. Pseudospin direction is plotted with white arrows, and its projection on the x axis is additionally plotted with colour. Blue corresponds to negative projection and horizontal linear polarization, red signifies positive sign of projection and vertical linear polarization. (b) panel is a zoom of the whole Brillouin zone pseudospin polarization map, plotted in (a) panel. It demonstrates Dresselhaus SOC field configuration of the effective field due to TE-TM field in the vicinity of the Dirac points, as the eigenstate pseudospin is directed along the effective field. From Nalitov et al. (2015) [90]

absence of effective SOC the upper and lower degenerate in spin branches intersect at K and K' points, forming Dirac cones. The band energy width is $6J$.

SOC, however, changes the topology of the band structures, lifting the spin degeneracy. The SOC strength may be characterized by the ratio $\delta J/J$. In sufficiently weak SOC ($\delta J/J < 0.5$) each Dirac cone is split in four, so that instead of two intersection points lower and upper bands have 8 points of intersection, as seen from Fig. 4.6(b). This effect is known as the trigonal warping and also occurs in bilayer graphene [91] and in monolayer graphene with Rashba SOC [92]. If $\delta J \ll J$, the distance δK between a Dirac point and additional pockets is approximately given by $(\delta J/J)^2 a^{-1}$. These pockets stay on the Brillouin zone edges and move towards the centers of the edges with increasing $\delta J/J$.

When $\delta J = J/2$, a transition of the dispersion topology occurs: the additional Dirac points originating from K and K' meet at the M point and annihilate. The energy dispersion along the principal directions below and above the critical SOC strength is plotted in Fig. 4.7.

4.1.5 Optical spin Hall effect in polariton graphene

The effective Hamiltonian of polariton graphene may be formulated in terms of pseudospin operators $\boldsymbol{\sigma}$ and \mathbf{s} , having the same matrix form of Pauli matrices vector and correspond-

ing to sublattice (A/B) and polarization degrees of freedom. It may be separated into polarization-independent part $H_{\mathbf{k}}^{(0)}$, coupling $\boldsymbol{\sigma}$ with momentum and giving a standard graphene dispersion with two Dirac valleys K and K', and a spin-orbit term $H_{\mathbf{k}}^{\text{SO}}$, coupling \mathbf{s} with $\boldsymbol{\sigma}$ and momentum:

$$H_{\mathbf{k}}^{(0)} = -J\sigma_+ f_{\mathbf{k}} \otimes \hat{1} + H.c., \quad (4.27)$$

$$H_{\mathbf{k}}^{\text{SO}} = -\delta J\sigma_+ \otimes (f_{\mathbf{k}}^+ s_+ + f_{\mathbf{k}}^- s_-) + H.c.. \quad (4.28)$$

where $\sigma_{\pm} = (\sigma_x \pm i\sigma_y)/2$, $s_{\pm} = (s_x \pm is_y)/2$, the \otimes symbol denotes Kronecker product and $\hat{1}$ is the identity operator in the spin subspace. Expanding Eqs. (4.27, 4.28) and keeping the first order in $\mathbf{q} = \mathbf{k} - \mathbf{K}$, we isolate the momentum independent and dependent parts $H_{\mathbf{K}}^{\text{SO}}$ and $H_{\mathbf{q}}^{\text{SO}}$ to finally rewrite all terms in the low-energy approximation

$$H_{\mathbf{q}}^{(0)} = \hbar v_F (\tau_z q_x \sigma_x + q_y \sigma_y), \quad (4.29)$$

$$H_{\mathbf{K}}^{\text{SO}} = \Delta (\tau_z \sigma_y s_y - \sigma_x s_x), \quad (4.30)$$

$$H_{\mathbf{q}}^{\text{SO}} = \frac{\Delta a}{2} [s_x (\tau_z q_y \sigma_y - q_x \sigma_x) - s_y (\tau_z q_x \sigma_y + q_y \sigma_x)], \quad (4.31)$$

where $v_F = 3Ja/(2\hbar)$, $\Delta = 3\delta J/2$ and τ_z equals +1 and -1 for K and K' valleys respectively. Here, the same basis as the the one of Kane and Mele [93] is used in order to allow a direct comparison with their Hamiltonian. This basis is different from the original basis of Wallace [94], which is used in the Eq. (4.36). The passage from Wallace to Kane is obtained by writing $q_x \rightarrow q_y, q_y \rightarrow -q_x$. The term in Eq. (4.30), similar to the Rashba term introduced by Kane and Mele [93, 95], is dominant in the region of reciprocal space where $qa \ll \delta J/J$ and is responsible for the band splitting at K and K'. The interplay between (4.29) and (4.30) produces an effective photon mass $m^* = (2c\hbar^2\delta J)/(3a^2J^2)$ in this region.

Provided $\delta J \ll J$, the term in Eq. (4.30) dominates over that of Eq. (4.31) in the region $\delta J/J \ll qa \ll 1$, but plays a role of a perturbation over the polarization-independent term (4.29), splitting its linearly polarized eigenstates in energy. It may therefore be interpreted as pseudospin interaction with an emergent in-plane effective magnetic field in this region. Considering either positive ($c = +1$) or negative ($c = -1$) energy states, spin-orbit term (4.30) transforms to a symmetry-allowed Dresselhaus-like emergent field

$$H_c^{\text{SO}} = -\Delta c\tau_z (q_x s_x - q_y s_y) / q. \quad (4.32)$$

The SOC effective field Hamiltonian in the highest order in momentum may be there-fore expressed in the minimal coupling form:

$$H_{\mathbf{q}}^{(0)} + H_{\mathbf{K}}^{\text{SO}} = \hbar v_F \left(\tau_z \sigma_x \left[q_x - \frac{\Delta}{\hbar v_F} \tau_z^{-1} s_x \right] + \sigma_y \left[q_x + \frac{\Delta}{\hbar v_F} \tau_z s_y \right] \right). \quad (4.33)$$

The effective field x and y components are not commutative, inheriting this property from the Pauli matrices s_x and s_y . It therefore can be represented as a non-Abelian gauge field. The effective field follows the direction of the lowest branch pseudospin direction map, plotted in Fig. 4.8.

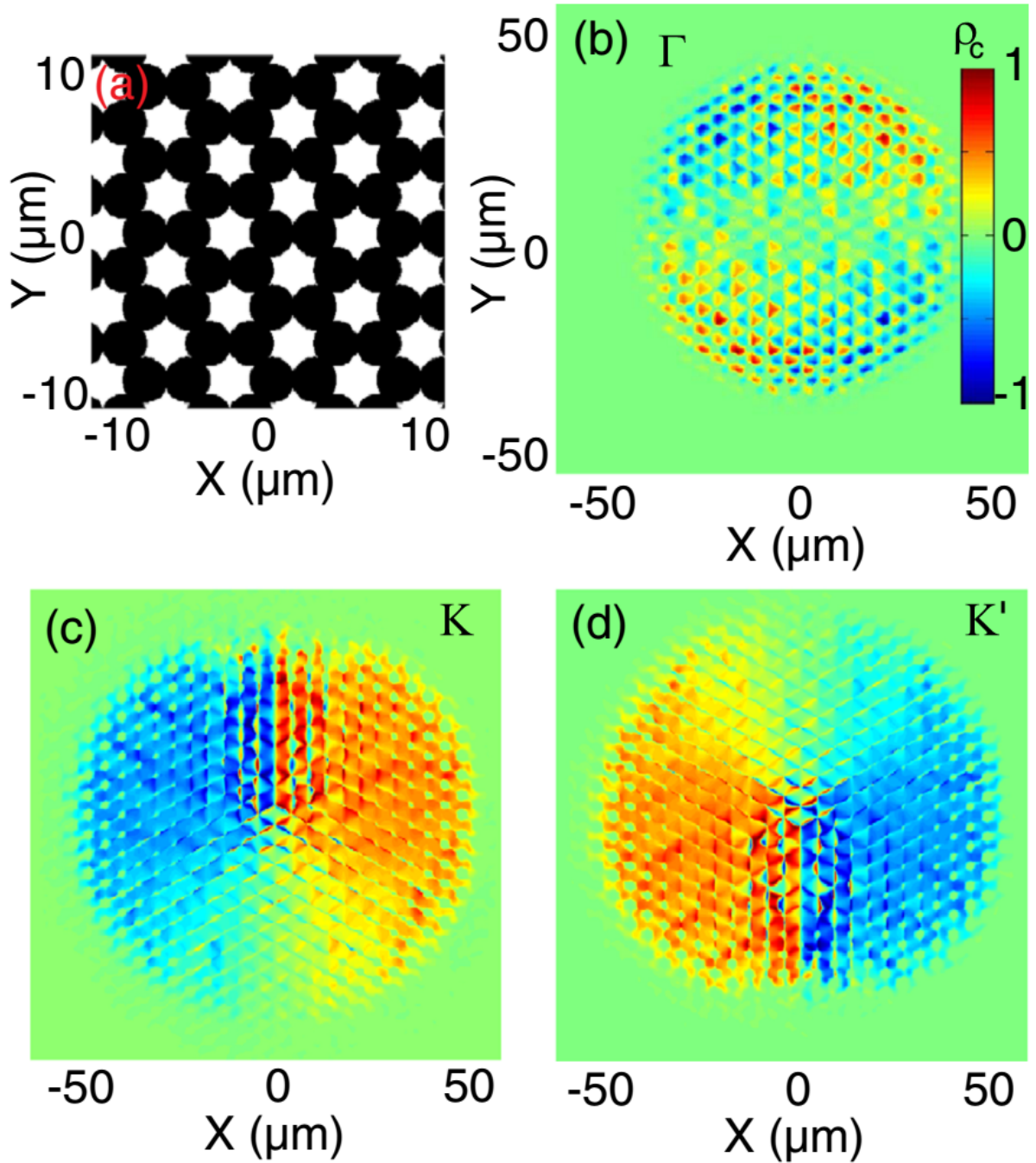


Figure 4.9: optical spin Hall effect (OSHE) modelling in polariton graphene. (a) Potential profile: black regions correspond to negative potential and simulate photon confinement. (b) OSHE modelling with resonant linearly polarized excitation of the Γ point of the lowest energy dispersion branch (the ground state). The circular polarization ρ_c , given with color, has four domains in space, analogously to the conventional OSHE in planar microcavities. (c) and (d) panels demonstrate OSHE simulation with resonant excitation of K and K' points (excitation frequency corresponds to the center of the lowest band). They have two spatial domains of circular polarization sign, revealing gauge nature of the effective spin-orbit interaction field. From Nalitov et al. (2015) [90]

The tight-binding approach may be further checked with direct simulation of the Schroedinger equation with TE-TM splitting and a honeycomb symmetry potential, including the broadening induced by the finite life time. A structure etched out of a planar microcavity, where the graphene atoms are represented by overlapping pillars (Fig. 3a), was considered. The equation of motion for the photonic spinor reads:

$$i\hbar \frac{\partial \psi_{\pm}}{\partial t} = \left[-\frac{\hbar^2}{2m} \Delta + U - \frac{i\hbar}{2\tau} \right] \psi_{\pm} + \beta \left(\frac{\partial}{\partial x} \mp i \frac{\partial}{\partial y} \right)^2 \psi_{\mp} + \sum_j P_{j\pm} e^{-\frac{t^2}{\tau_0^2} - \frac{(\mathbf{r}-\mathbf{r}_j)^2}{\sigma^2} + i(\mathbf{k}\mathbf{r}-\omega t)}. \quad (4.34)$$

where $\psi(r) = \psi_+(r), \psi_-(r)$ are the two circular components of the photon wave function, m is the cavity photon mass, and $\tau = 25$ ps the lifetime. This equation describes the photon dynamics in a planar cavity in the presence of TE-TM splitting of strength $\beta = \hbar^2 (m_l^{-1} - m_t^{-1}) / 4m$, where $m_{l,t}$ are the effective masses of TM and TE polarized particles, respectively, and $m = 2(m_t - m_l) / m_t m_l$ [96]. The following effective masses were taken: $m_t = 5 \times 10^{-5} m_0$, $m_l = 0.95 m_t$, with m_0 representing the free electron mass. The honeycomb lattice is account for via the potential $U(r)$, as shown in Fig. 4.9(a) (24x24 elementary cells). Here, P_0 is the amplitude of the pumping laser (identical for both components, corresponding to horizontal polarization), the pulse duration being $\tau_0 = 1$ ps, and the size of the spot $\sigma = 15 \mu\text{m}$. The pumping is localized in real space and in reciprocal space close to the selected point (Γ , K or K'). We have performed numerical simulation of optical spin Hall effect in photonic graphene using a high-resolution (512x512) representation of a potential, similar to the one already studied in experiments [87]. The nVidia CUDA graphical processor was used to carry out the integration of the 2D spinor Schroedinger equation.

Fig. 4.9(a,b,c) demonstrates the snapshots of the circular polarization degree as a function of coordinates, taken at $t = 30\text{ps}$. Panel b) shows the polarization degree for the excitation at the Γ point, where the field has the typical TE-TM texture, featuring the four polarization domains [25, 26, 97]. Panels c), d) demonstrate the optical spin Hall effect at the K and K' points respectively, where the field has the texture of the Dresselhaus SOC. This is evidenced by two polarization domains in real space [66, 98], being inverted between the K and K' points, as the fields around K and K' have opposite signs

The OSHE texture is a demonstration of the different nature of the effective SOC field at the two Dirac points K and K' . From this numerical experiment, one may clearly see the advantage of photonic systems in comparison to solid state systems, which allow us to excite and analyze any point of the dispersion with much more facility. Another very interesting consequence of this work relies on the possibilities offered i) by the manipulation of the lattice geometry and ii) by the hybrid exciton-photon nature of the polaritons. The same system geometry has been used to create a photonic topological insulator [99]. Combined with SOC, it paves the stage for very broad applications. For example, the mixed nature of exciton-polaritons provides a magnetic response of the system at optical frequencies, which is crucial for realization a photonic topological insulator [100, 101, 102, 103]. Moreover, polariton-polariton interactions, resulting in strong nonlinear optical response, allow for exploration of quantum light with spin-anisotropic interactions [104, 96]. Nonlinear OSHE associated with the transmutation of topological defects and focusing of spin currents has been already described in planar structures [97].

The behavior of soliton states in photonic topological insulators was recently considered [105]. Polaritonic graphene [87] therefore opens very large possibilities for the studies of interacting spinor quantum fluids, in the presence of different types of real and effective magnetic fields which suggest accessibility to various quantum phases.

4.2 Polariton topological insulator

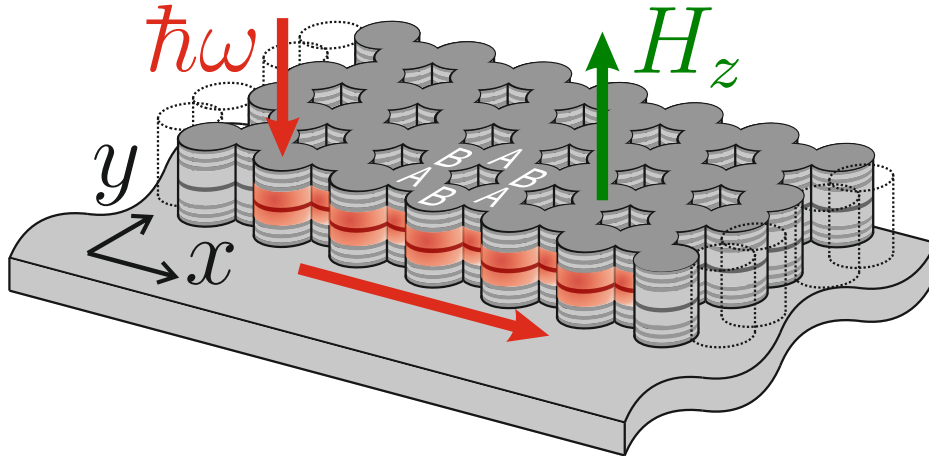


Figure 4.10: Topologically protected light propagation along the edge of a polariton topological insulator. The polariton graphene considered is based on an etched planar microcavity. The cavity is constituted by two Distributed Bragg Reflectors (DBRs) sandwiching a cavity with embedded Quantum Wells (QWs). The energy splitting existing between TE and TM polarized modes provides the photonic SOC. The application of a real magnetic field perpendicular to the x - y plane of the structure opens the non-trivial gap. Edge modes are one way propagative modes which cannot elastically scatter to the bulk states. In a stripe geometry, normally incident light is guided either clockwise or anti-clockwise, depending on the external magnetic field sign.

The history of topological insulators (TI) dates back to the discovery of Quantum Hall Effect (QHE) by Klaus von Klitzing in the year 1980 [106]. In his experiment, a strong magnetic field pinned the conduction band electrons to the Landau levels, opening a band gap in the bulk and thus converting an electron conductor to an insulator. The edge electron states, on the contrary, carried one-way currents, protected from backscattering and responsible for the integer Hall conductance [107]. This is an example of a \mathbb{Z} topological insulator. The classification which allowed to distinguish this phase from a conventional band insulator, is based on the Chern topological invariant [108] – an integer number characterizing the band structure in terms of Berry phase.

A whole new family of TI materials with different sets of topological invariants and symmetries were later proposed and discovered [109]. Graphene has a special place in this family: it allowed the observation of QHE at room temperature [110] and played a role of a model system for QHE without net magnetic flux [111] and the quantum spin Hall effect (QSHE) [93]. The latter is associated with topologically-protected boundary

spin currents and is characterized by a non-zero \mathbb{Z}_2 invariant stemming from the SOC for electrons [95] (without external magnetic field). These spin currents in the \mathbb{Z}_2 TI are formed from two spin components propagating in opposite directions, contrary to the \mathbb{Z} TI, where both spin components propagate in the same direction, the other being forbidden. Although the extremely small SOC has not allowed to observe QSHE in graphene, it was later demonstrated in various 2D and 3D structures [112, 113]. A Floquet TI having a topologically nontrivial gap was realized in 2D heterostructure under a microwave-range electromagnetic irradiation [114].

Many promising implementations of topological phases in bosonic systems were recently proposed in honeycomb photonic gyromagnetic waveguides [100, 115], coupled microcavities [116], coupled cavity rings [117], coupled waveguides with a spatial modulation [99], and photonic waveguides (out of the optical range) based on metamaterials with bi-anisotropic behaviour [118, 119]. Finally, optical QHE due to artificial gauge fields [120] was predicted in microcavity lattices.

The microcavity platform provides natural susceptibility of polaritons to magnetic field due to the excitonic component and the effective SOC due to the photonic part. This chapter is devoted to the demonstration of the \mathbb{Z} topological insulator behaviour of polariton graphene in external magnetic field. The band gap opening is discussed in terms of tight-binding approximation in Subsection 1. Topological invariant analysis of the band structure with gap is conducted in Subsection 2. Polaritonic edge states are directly derived from the tight-binding model in Subsection 3. Finally, a full numerical simulation of edge propagation is described in Subsection 4 within the spin Schrodinger wave equation formalism.

4.2.1 Energy polariton bandgap in external magnetic field

We construct the polaritonic graphene effective Hamiltonian in nearest neighbor approximation. A state of the polariton graphene can be described by a bispinor $\Phi = (\Psi_A^+, \Psi_A^-, \Psi_B^+, \Psi_B^-)^T$, with $\Psi_{A(B)}^\pm$ – the wave functions of the two sublattices and two spin components. We account for the magnetic field via the Zeeman splitting Δ of states, localized at each pillar. It affects the diagonal blocks of the Hamiltonian matrix form (4.24). The effective Hamiltonian in the presence of a real magnetic field applied along the z-direction reads:

$$\mathbf{H}_{\mathbf{k}} = \begin{pmatrix} \Delta\sigma_z & \mathbf{F}_{\mathbf{k}} \\ \mathbf{F}_{\mathbf{k}}^\dagger & \Delta\sigma_z \end{pmatrix}, \quad \Delta = |x|^2 g_X \mu_B H_z / 2, \quad (4.35)$$

where σ_z is the Pauli matrix, x is the excitonic Hopfield coefficient, g_X is the effective g-factor for the 2D exciton, μ_B is the Bohr magneton, and H_z is the applied magnetic field, giving rise to polariton Zeeman splitting Δ .

$$\mathbf{F}_{\mathbf{k}} = - \begin{pmatrix} f_{\mathbf{k}} J & f_{\mathbf{k}}^+ \delta J \\ f_{\mathbf{k}}^- \delta J & f_{\mathbf{k}} J \end{pmatrix}, \quad (4.36)$$

where complex coefficients $f_{\mathbf{k}}, f_{\mathbf{k}}^\pm$ are defined by:

$$f_{\mathbf{k}} = \sum_{j=1}^3 \exp(-i\mathbf{k}\mathbf{d}_{\varphi_j}), \quad f_{\mathbf{k}}^\pm = \sum_{j=1}^3 \exp(-i[\mathbf{k}\mathbf{d}_{\varphi_j} \mp 2\varphi_j]),$$

and $\varphi_j = 2\pi(j - 1)/3$ is the angle between horizontal axis and the direction to the j th nearest neighbor of a type-A pillar. J is the polarisation independent tunneling coefficient, whereas δJ is the SOC-induced polarisation dependent term. Without the magnetic field, the Hamiltonian (4.35) can be exactly diagonalized [90]. The energy dispersions obtained are relatively close to those of bilayer graphene [121], and of a monolayer graphene in presence of Rashba SOC [92]. The polarization texture of the eigenstates is, however, different.

The dispersion close to the \mathbf{K} point is shown in dashed line on Fig. 4.11(a). Under the effect of SOC, the Dirac point transforms into four inverted parabolas. Two parabolas are split off, while the two central ones cross each other. It is instructive to consider the eigenstates exactly at the Dirac points. At the K point, the eigenstates of the two central parabolas are fully projected on Ψ_A^- and Ψ_B^+ respectively, whereas at the K' point they project on Ψ_A^+ and Ψ_B^- respectively. Let us now qualitatively consider the consequence of a finite Zeeman splitting. As sketched on the Fig. 2(b), the degeneracy between the states in the crossing points of two branches (dashed lines) is lifted by 2Δ , and the states split off by the SOC are further shifted. At the $K(K')$ point, the "valence" band is formed from the B(A)-pillars and the "conduction" band from the A(B)-pillars. The reversed order of the band in the basis of the sublattices signifies a topological non-triviality of the gap[109]. In the spin basis, however, the valence and conduction bands are equivalent at K and K' , unlike the \mathbb{Z}_2 -topological insulator [109].

The result of the complete diagonalisation of the Hamiltonian (4.35) is plotted with solid lines in the Fig. 2(a). As expected, it shows an energy gap, saturating to $E_g \sim 3\delta J$ at $|\Delta| \sim \delta J$. Without SOC ($\delta J = 0$), the application of a magnetic field does not open any gap, as it keeps the symmetry between K and K' valleys, while breaking the symmetry between the spin projections on the z axis. The band structure in this latter case is constituted by two graphene dispersions shifted in energy by the polariton Zeeman splitting.

4.2.2 Topological invariant analysis

The topological invariants are integer numbers characterizing the band structure, which cannot be changed with continuous transformations of the bands. Nonzero topological invariants distinguish topologically trivial band insulators from nontrivial ones. In particular, nonzero Chern numbers correspond to a topological insulator of \mathbb{Z} type. Band Chern number may be calculated from the Berry connection over the Brillouin zone [109]:

$$C_m = \frac{1}{2\pi} \iint_{\text{BZ}} \mathbf{B}_{\mathbf{k},m} d^2\mathbf{k}, \quad (4.37)$$

where m is the branch index, and the Berry curvature $\mathbf{B}_{\mathbf{k},m}$ is expressed in the effective Hamiltonian (4.35) and its eigenstates $|\Phi_{\mathbf{k},m}\rangle$ with corresponding energies $E_{\mathbf{k},m}$:

$$\mathbf{B}_{\mathbf{k},m} = i \sum_{l \neq m} \frac{\langle \Phi_{\mathbf{k},m} | \nabla_{\mathbf{k}} H_{\mathbf{k}} | \Phi_{\mathbf{k},l} \rangle \times \langle \Phi_{\mathbf{k},l} | \nabla_{\mathbf{k}} H_{\mathbf{k}} | \Phi_{\mathbf{k},m} \rangle}{(E_{\mathbf{k},m} - E_{\mathbf{k},l})^2}. \quad (4.38)$$

A direct numerical calculation of the Berry curvature for the polariton graphene bands shows that it is nonzero in the vicinity of the Dirac points. The two inner branches, split

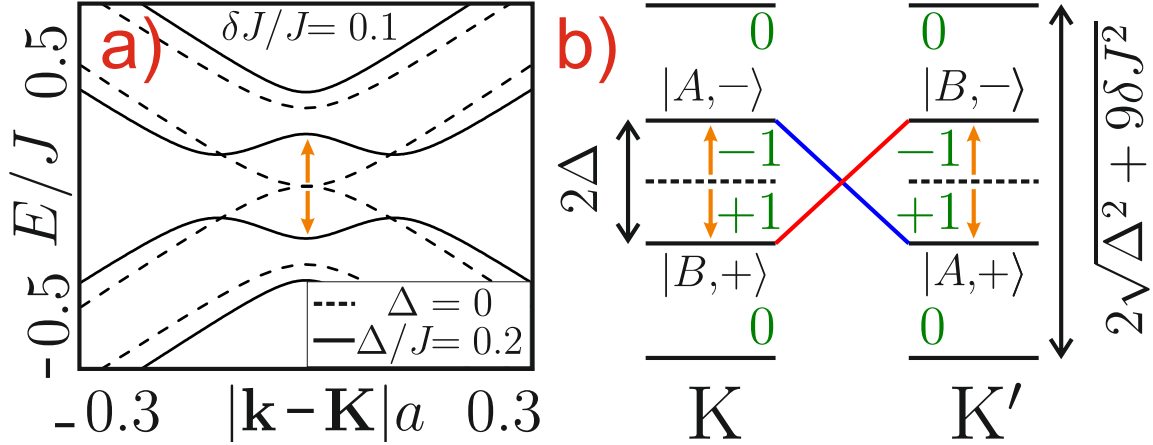


Figure 4.11: Non-trivial bulk band structure of the polariton graphene in an external magnetic field. (a) bulk energy dispersion without (dashed) and with (solid) magnetic field. (b) illustration of degeneracy lifting in K and K' points. Due to coupling between sublattice and polarisation, the states, localized on one sublattice, go up in energy at one point and down in the other. Chern numbers at each point are shown in green. From Nalitov et al. (2015) [103]

by the interplay of the external magnetic field and effective SOC, have non-zero Berry connections around K and K' point, each giving ± 1 contribution to the total band Chern number ± 2 (marked in green in Fig. 4.11(b)). Outer branches, on the contrary, have zero Berry curvature over all reciprocal space. Parameters taken: $\delta J/J = 0.1$, $\Delta/J = 0.01$.

Nonzero Chern numbers demonstrate the topological nontriviality of the polariton graphene band structure in presence of external magnetic field. The bulk-boundary correspondence yields the existence of one-way edge states on an interface between topologically trivial and nontrivial insulators. The energy of states must lie in the energy gap, and their dispersion connects the lower and upper bands. The vacuum itself is a trivial band insulator, therefore, any edge of the polariton graphene, either zigzag or armchair, conducts polaritons in a direction specified by the magnetic field sign.

4.2.3 Topologically protected edge states

To demonstrate the consequence of the bulk-boundary correspondence, one-way edge states, we used the same tight-binding approach to model a quasi-1D stripe of microcavity pillars, consisting of $N = 50$ zig-zag chains. We derive and diagonalize the $4N \times 4N$ Hamiltonian to obtain the band structure. For this, we set a basis of Bloch waves $\Psi_{A/B,n}^{\pm}(k_x)$, where n index numerates stripes, and k_x is the quasi-wavevector in the infinite zig-zag direction. 4×4 diagonal blocks D_{k_x} describe coupling within one stripe and are derived in the same fashion as Hamiltonian (4.35), while the coupling between the stripes is accounted for in subdiagonal and superdiagonal 4×4 blocks $S_{k_x}^{\dagger}$ and S_{k_x} . The whole matrix

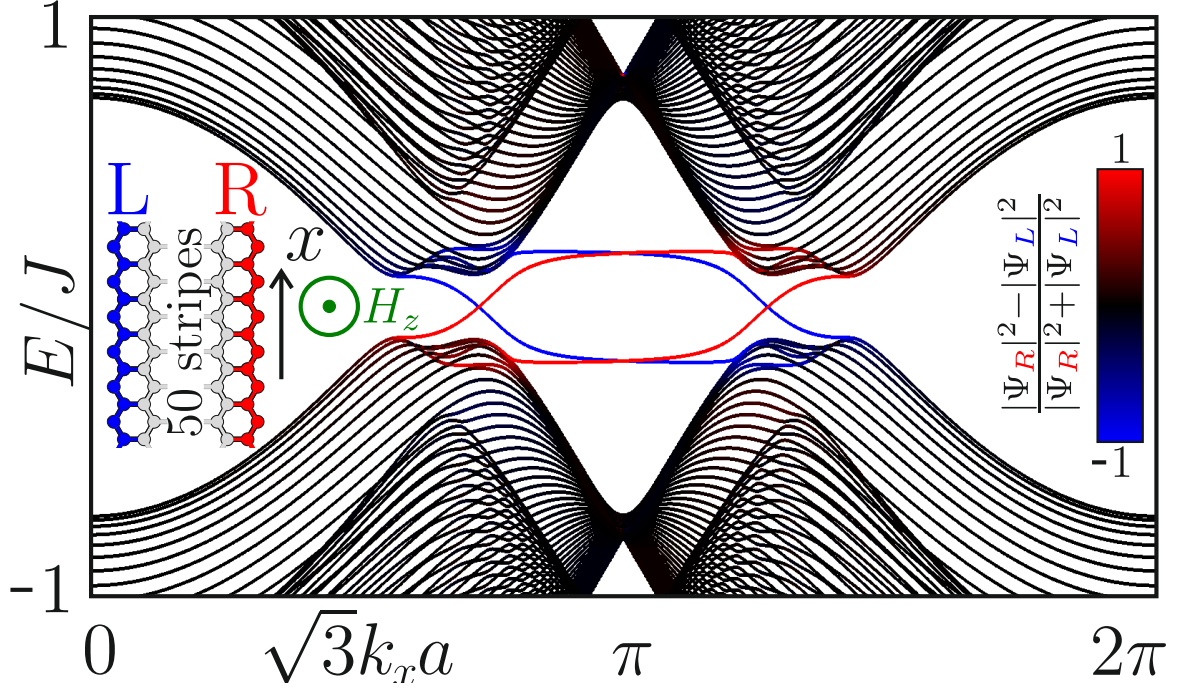


Figure 4.12: Numerical calculation of eigenstates: edge states are marked with colour. Direction of their propagation is given by the sign of the product $H_z g_X$ and is protected from both backscattering and scattering into the bulk. From Nalitov et al. (2014) [103].

reads:

$$H_{k_x} = \underbrace{\begin{pmatrix} D_{k_x} & S_{k_x} & 0 & \dots & 0 & 0 & 0 \\ S_{k_x}^\dagger & D_{k_x} & S_{k_x} & \dots & 0 & 0 & 0 \\ 0 & S_{k_x}^\dagger & D_{k_x} & \dots & 0 & 0 & 0 \\ \vdots & \vdots & \vdots & \ddots & \vdots & \vdots & \vdots \\ 0 & 0 & 0 & \dots & D_{k_x} & S_{k_x} & 0 \\ 0 & 0 & 0 & \dots & S_{k_x}^\dagger & D_{k_x} & S_{k_x} \\ 0 & 0 & 0 & \dots & 0 & S_{k_x}^\dagger & D_{k_x} \end{pmatrix}}_{50 \text{ blocks } 4 \times 4}, \quad (4.39)$$

where

$$D_{k_x} = - \begin{pmatrix} -\Delta & 0 & Jf_{k_x} & \delta Jf_{k_x}^+ \\ 0 & \Delta & \delta Jf_{k_x}^- & Jf_{k_x} \\ Jf_{k_x}^* & (\delta Jf_{k_x}^-)^* & -\Delta & 0 \\ (\delta Jf_{k_x}^+)^* & Jf_{k_x}^* & 0 & \Delta \end{pmatrix}, \quad S_{k_x} = - \begin{pmatrix} 0 & 0 & 0 & 0 \\ 0 & 0 & 0 & 0 \\ J & \delta J & 0 & 0 \\ \delta J & J & 0 & 0 \end{pmatrix}, \quad (4.40)$$

and complex coefficients f_{k_x} and $f_{k_x}^\pm$ are defined by the following:

$$f_{\mathbf{k}} = \sum_{j=1}^2 \exp(-i\mathbf{k}\mathbf{d}_{\varphi_j}), \quad f_{\mathbf{k}}^\pm = \sum_{j=1}^2 \exp(-i[\mathbf{k}\mathbf{d}_{\varphi_j} \mp 2\varphi_j]),$$

Note that here the summation is only conducted over two terms corresponding to two the nearest neighbours within a zigzag chain.

Fig. 2(c) shows the result of the band structure calculation. The degree of localization on edges is calculated from the wave function densities on the very left and the very right zigzag chains $|\Psi_L|^2$ and $|\Psi_R|^2$ (see inset), and is shown with colour, so that the edge states are blue and red. The propagation direction of these edge states is related to the direction of the external magnetic field: the photon edge current is either clockwise or anti-clockwise depending on the signs of H_z and g_X . One should insist on the fact that we deal with a real polariton current and not with a spin current.

The presented results were obtained for the most realistic case of rather small SOC ($\delta J/J = 0.1$). In this case, the dispersion topology in the absence of magnetic field is characterized by the trigonal warping effect, typical for bilayer graphene [121] and monolayer graphene with Rashba SOC [92]. It consists in emergence of three additional Dirac cones in the vicinity of each Brillouin zone corner. However, at a critical strength of the spin-orbit interaction $\delta J = J/2$, a transition occurs in the topology of the dispersion: additional Dirac cones with opposite Chern numbers meet in pairs at the centers of Brillouin zone edges and recombine. This leads to a change of the band Chern number set from $C_m = \pm 2$ to $C_m = \pm 1$.

4.2.4 Edge propagation simulation

In order to demonstrate the feasibility of experimental observations and to confirm the predictions of the tight-binding model, namely, one-way propagation, schematically sketched in Fig. 4.10, a full numerical simulation was conducted, which describes the time evolution of the polariton wavefunction by solving the spinor Schrodinger equation:

$$i\hbar \frac{\partial \psi_{\pm}}{\partial t} = \left[-\frac{\hbar^2}{2m} \Delta + U - \frac{i\hbar}{2\tau} \pm \Delta \right] \psi_{\pm} + \beta \left(\frac{\partial}{\partial x} \mp i \frac{\partial}{\partial y} \right)^2 \psi_{\mp} + \sum_j P_{j\pm} e^{-\frac{t^2}{\tau_0^2} - \frac{(\mathbf{r}-\mathbf{r}_j)^2}{\sigma^2} + i(\mathbf{k}\mathbf{r} - \omega t)}. \quad (4.41)$$

where $\psi(\mathbf{r}, t) = \psi_+(\mathbf{r}, t), \psi_-(\mathbf{r}, t)$ are the two circular components of the wave function, m is the polariton mass, τ the lifetime. Particles are created in three spots by pulsed quasi-resonant pumping. The nVidia CUDA graphical processor was used to carry out the numerical integration of the 2D spinor Schrodinger equation. The high-resolution (1024x1024) honeycomb lattice potential $U(r)$ contains 23x30 elementary cells. The pillar size was 1.3 μm , and the center-to-center distance $d = 2.5 \mu\text{m}$. All energies are measured from the bottom of the polariton branch, which can shift with the magnetic field. Circular excitation allows to be sure that all linearly polarized states are pumped with sufficient efficiency.

Fig. 4.13 demonstrates qualitatively different behaviour with and without the magnetic field (parameters of the simulations are given in the caption). Without the field ($\Delta = 0$), the excitation energy corresponds to propagating states, and the resulting expansion of polaritons is visible on panel a). No gap is opened, and the particles created on the surface by the two corresponding pumps are rapidly expanding into the bulk: after only 20 ps, the intensity is distributed over a significant part of the sample. However, under an applied field giving $\Delta = 0.1$ meV, the excitation energy lies within a gap, which makes the injection in the center ineffective: no particles created by the pump are visible in the center after 100 ps. But the spots on the edges become now resonant with the sur-

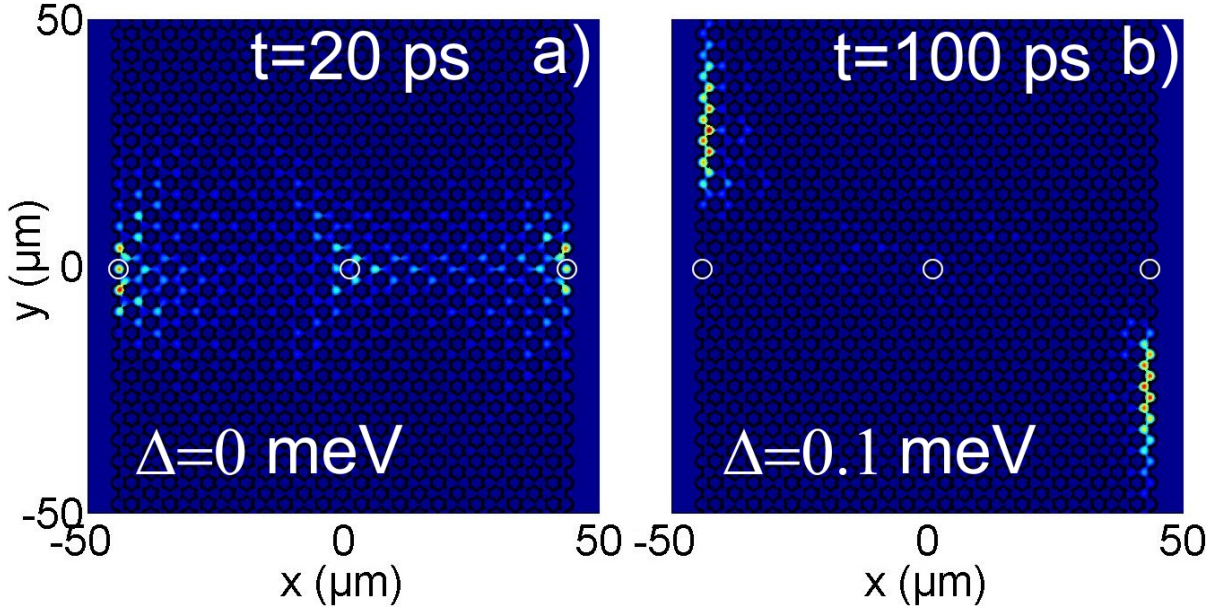


Figure 4.13: Propagation of light in the conducting ($\Delta = 0$) and topological insulator phase ($\Delta \neq 0$) Calculated spatial distribution of emission intensity. a) rapid expansion of the bulk propagative states after 20 ps at $\Delta=0$; b) surface states after 100 ps at $\Delta=0.1$ meV. White circles show the pumping spots located at \mathbf{r}_j , and black line traces the contours of the potential. The parameters are: $\beta = \hbar^2 (m_l^{-1} - m_t^{-1}) / 4m$ where $m_{l,t}$ are the effective masses of TM and TE polarized particles respectively and $m = 2(m_t - m_l) / m_t m_l$; $m_t = 5 \times 10^{-5} m_0$, $m_l = 0.95 m_t$, where m_0 is the free electron mass. $\tau_0 = 35$ ps, $\sigma = 1 \mu\text{m}$, $\omega = 1.6$ meV and lies within the bulk energy gap, $\tau = 25$ ps. Pumping P is circularly polarized. From Nalitov et al. (2014) [103].

face states which have appeared there, and their one-way propagation is visible in panel b): after 100 ps, particles are about $25 \mu\text{m}$ away from the pump spots. Although particles are created with both positive and negative wavevectors along a given edge, they propagate in only one direction, which proves the one-way nature of the surface states. The transverse profile of these states shows an exponential decay with a characteristic length of $(2\kappa)^{-1} = 3.1 \pm 0.1 \mu\text{m}$, corresponding to the analytical estimate of the extinction coefficient $\kappa \approx \sqrt{2mE_g/\hbar^2}$ determined by the size of the gap E_g . Thus, the full numerical simulation confirms the predictions of the tight-binding model on the appearance of the gap in the presence of magnetic field and the formation of one-way surface states.

Various configurations of polaritonic graphene geometry were used to test the topological protection of the edge states. In square geometry states, resonantly excited at one of the edges propagated along the perimeter, turning around the corners. Defect configuration had one cavity pillar missing at one of the edges. In this case one-way edge state went around the defect without backscattering. In general edge states are protected from elastic scattering, although inelastic scattering on phonons may result in populating the the bands. Importantly, finite lifetime of polaritons limits the protection because of energy broadening of the edge states. Finally, one should note that a smooth potential defect of the same order as the bandgap value may transfer polaritons, initially generated at an edge in the bandgap, into the regions of the edge state branches, where they can elastically scatter into the bulk polaritonic band.

All the parameters used in numerical simulations are entirely realistic. Indeed, the experimental realisation of the effect has one important requirement: both δJ and Δ must exceed the broadening, which is of the order of $1/(25 \text{ ps}) \approx 30 \mu\text{eV}$ [87]. The photonic SOC finds its origin in the polarisation splittings of photonic nanostructures. In etched planar cavities, it is induced by the TE-TM splitting [96], but also by strain and other structural effects which enhance the splittings up to $50\text{-}200 \mu\text{eV}$ in 1D ridges [122], or coupled pillar structures [89]. The Zeeman splitting between the spin components of polaritons can be of the order of $100\text{-}200 \mu\text{eV}$ at moderate magnetic fields (about 10 T) [123, 124]. The size of the pillars we consider allows the formation of clearly separated s and p-bands, so the presence of the excited states does not affect the lowest band. Moreover, as shown by our preliminary calculations, the p-band [87] might be even more suitable for the observation of topologically protected surface states due to the increased SOC.

4.3 Conclusion

The final chapter is an focused on our three most recent works on the effects of SOC for light in microcavity pillar superstructures [88, 90, 103]. It starts with the derivation of effective SOC stemming from the TE-TM splitting of microcavity photonic modes. Its application to the case of polariton benzene molecule results in an energy splitting of eigenstates with defined orbital momentum. Interestingly, the split levels conduct quanta of circular spin currents.

In polaritic graphene, a two-dimensional honeycomb structure formed by microcavity pillars, the effective SOC transforms the topology of the polariton band structure. In the vicinity of the band touching points, the derived SOC effective field texture is similar to

that of the Dresselhaus SOC term. Similarly to the latter, it can be incorporated into the Hamiltonian in terms of minimal coupling as an interaction with a non-Abelian gauge field. The effective SOC field was proven to manifest itself in the optical spin Hall effect realized with resonant excitation of the Dirac point. Contrary to the conventional optical spin Hall effect, the spatial texture of the circular spin polarization degree in this case has two sign domains instead of four.

Finally, polariton graphene was demonstrated to become a \mathbb{Z} topological insulator with protected edge states at optical frequencies under an applied external magnetic field. It resembles the QHE behaviour of electrons and photons [116], both based on the appearance of Landau levels. However, its origin is different, being closer to the Haldane proposals [111, 100]. The gap appears in the present case due to the Zeeman splitting of electrically uncharged particles and specific spin orbit coupling acting together similarly to spatially alternating magnetic fields [111, 100]. The difference is underlined by the unique set of band Chern invariants $C_m = \pm 2$ (transforming into $C_m = \pm 1$ above critical SOC strength). From the point of view of symmetry, the topologically nontrivial gap is a manifestation of broken time-reversal and in-plane rotational symmetry by external magnetic field and effective SOC respectively. The interacting nature of polaritons opens interesting possibilities of studying collective bosonic effects [104] in TIs. The spin-anisotropy of these interactions [96] leads to self-induced Zeeman splitting, allowing a self-induced TI for a polarized polariton Bose-Einstein condensate.

List of used acronyms

- OPO - Optical Parametric Oscillator
- IX - (spatially) Indirect Exciton
- DX - (spatially) Direct Exciton
- QW - Quantum Well
- CQWs - Coupled Quantum Wells
- ASDQWs - Asymmetric Double Quantum Wells
- BEC - Bose-Einstein Condensation
- DBR - Distributed Bragg Reflector
- SOC - Spin-Orbit Coupling
- BIA - Bulk-Induced Asymmetry
- SIA - Structure-Induced Asymmetry
- IIA - Interface-Induced Asymmetry
- PL - Photoluminescence
- OSHE - Optical Spin Hall Effect
- QHE - Quantum Hall Effect
- LBS - Localized Bright Spot
- LP - Lower Polariton (branch)
- MP - Middle Polariton (branch)
- UP - Upper Polariton (branch)
- TE - Transverse Electric (mode)
- TM - Transverse Magnetic (mode)

List of publications

1. A. V. Nalitov, D. D. Solnyshkov, G. Malpuech. Polariton Z Topological Insulator. *Phys. Rev. Lett.*, 114, 116401 (2015)
2. A. V. Nalitov, G. Malpuech, H. Terças, and D. D. Solnyshkov. Spin-orbit coupling and optical spin Hall effect in photonic graphene. *Phys. Rev. Lett.*, 114, 026803 (2015)
3. A. V. Nalitov, D. D. Solnyshkov, N. A. Gippius, and G. Malpuech. Voltage control of the spin-dependent interaction constants of dipolaritons and its application to optical parametric oscillators. *Phys. Rev. B*, 90, 235304 (2014)
4. V. G. Sala, D. D. Solnyshkov, I. Carusotto, T. Jacqmin, A. Lemaitre, H. Tercas, A. Nalitov, M. Abbarchi, E. Galopin, I. Sagnes, J. Bloch, G. Malpuech, A. Amo. Engineering spin-orbit coupling for photons and polaritons in microstructures. *Phys. Rev. X*, 5, 011034 (2015)
5. P. Andreakou, S. Cronenberger, D. Scalbert, A. Nalitov, N. A. Gippius, A. V. Kavokin, M. Nawrocki, J. R. Leonard, L. V. Butov, K. L. Campman, A. C. Gossard, M. Vladimirova. Nonlinear optical spectroscopy of indirect excitons in biased coupled quantum wells. *Phys. Rev. B*, 91, 125437 (2015)
6. A. V. Nalitov, M. Vladimirova, A. V. Kavokin, L. V. Butov, and N. A. Gippius. Nonlinear optical probe of indirect excitons. *Phys. Rev. B*, 89, 155309 (2014)
7. J. Cuadra, D. Sarkar, L. Vina, J. M. Hvam, A. Nalitov, D. Solnyshkov, and G. Malpuech. Polarized emission in polariton condensates: Switching in a one-dimensional natural trap versus inversion in two dimensions. *Phys. Rev. B*, 88, 235312 (2013)
8. D. V. Vishnevsky, H. Flayac, A. V. Nalitov, D. D. Solnyshkov, N. A. Gippius, and G. Malpuech. Skyrmion Formation and Optical Spin-Hall Effect in an Expanding Coherent Cloud of Indirect Excitons. *Phys. Rev. Lett.*, 110, 246404 (2013)

Conferences

1. 16th International Conference on Physics of Light-Matter Coupling and Nanostructures, Medellin, Colombia (2015). Invited oral presentation, best young researcher award.
2. International School on the Physics of Indirect Excitons, Erice, Italy (2014). Poster presentation.
3. 15th International Conference on Physics of Light-Matter Coupling and Nanostructures, Montpellier, France (2014). Poster and oral presentations.
4. International Conference on Nanomaterials and Metastructures, Varadero, Cuba (2014). Poster presentation
5. 14th International Conference on Physics of Light-Matter Coupling and Nanostructures, Crete, Greece (2013). Oral presentation.
6. International School on Spin Dynamics in Semiconductor Structures, Tsakhkadzor, Armenia (2013). Oral presentation.
7. The European Workshop on Indirect Excitons, Barcelona, Spain (2012). Oral presentation.

Bibliography

- [1] Gregory H. Wannier. The structure of electronic excitation levels in insulating crystals. *Phys. Rev.*, 52:191–197, Aug 1937.
- [2] N. W. Ashcroft and Mermin. *Solid State Physics*. Saunders, 1976.
- [3] J. M. Luttinger. Quantum theory of cyclotron resonance in semiconductors: General theory. *Phys. Rev.*, 102:1030–1041, May 1956.
- [4] J. Frenkel. On the transformation of light into heat in solids. i. *Phys. Rev.*, 37:17–44, Jan 1931.
- [5] I. Vurgaftman, J. R. Meyer, and L. R. Ram-Mohan. Band parameters for III-V compound semiconductors and their alloys. *Journal of Applied Physics*, 89:5815–5875, June 2001.
- [6] Alexey Kavokin, Jeremy J Baumberg, Guillaume Malpuech, and Fabrice P Laussy. *Microcavities*. Oxford University Press, 2007.
- [7] Lucio Claudio Andreani, Francesco Tassone, and Franco Bassani. Radiative lifetime of free excitons in quantum wells. *Solid State Communications*, 77(9):641 – 645, 1991.
- [8] P. Andreakou, S. V. Poltavtsev, J. R. Leonard, E. V. Calman, M. Remeika, Kuznetsova Y. Y., L. V. Butov, J. Wilkes, M. Hanson, and Gossard A. C. Optically controlled excitonic transistor. *Applied Physics Letters*, 104(091101), 2014.
- [9] L.V. Butov, A. Imamoglu, K.L. Compman, and A.C. Gossard. Coulomb effects in spatially separated electron and hole layers in coupled quantum wells. *JETP*, 92(260), 2001.
- [10] Yu. E. Lozovik and O. L. Berman. Phase transitions in a system of two coupled quantum wells. *JETP Letters*, 64(8):573–579, 1996.
- [11] K. Sivalertporn, L. Mouchliadis, A. L. Ivanov, R. Philp, and E. A. Muljarov. Direct and indirect excitons in semiconductor coupled quantum wells in an applied electric field. *Phys. Rev. B*, 85:045207, Jan 2012.
- [12] G. Dresselhaus. Spin-orbit coupling effects in zinc-blende structures. *Phys. R.*, 100(2), 1955.

- [13] E. Rashba. Properties of semiconductors with an extremum loop. i. cyclotron and comminational resonance in a magnetic field perpendicular to the plane of the loop. *Sov. Phys. Solid State*, 2(1874), 1964.
- [14] Denis V. Bulaev and Daniel Loss. Spin relaxation and decoherence of holes in quantum dots. *Phys. Rev. Lett.*, 95:076805, Aug 2005.
- [15] E.I. Rashba and E.Ya. Sherman. Spin-orbital band splitting in symmetric quantum wells. *Physics Letters A*, 129(3):175 – 179, 1988.
- [16] M. V. Durnev, M. M. Glazov, and E. L. Ivchenko. Spin-orbit splitting of valence subbands in semiconductor nanostructures. *Phys. Rev. B*, 89:075430, Feb 2014.
- [17] A. A. High, J. R. Leonard, A. T. Hammack, M. M. Fogler, L. V. Butov, A. V. Kavokin, K. L. Campman, and A. C. Gossard. Spontaneous coherence in a cold exciton gas. *Nature*, 483(7391):584–588, March 2012.
- [18] L. D. Landau and E. M. Lifshitz. *Statistical Physics*, volume 5. Butterworth-Heinemann, Oxford, 1980.
- [19] L. V. Butov, L. S. Levitov, A. V. Mintsev, B. D. Simons, A. C. Gossard, and D. S. Chemla. Formation mechanism and low-temperature instability of exciton rings. *Phys. Rev. Lett.*, 92:117404, Mar 2004.
- [20] C. N. Yang. Concept of off-diagonal long-range order and the quantum phases of liquid he and of superconductors. *Rev. Mod. Phys.*, 34:694–704, Oct 1962.
- [21] Oliver Penrose and Lars Onsager. Bose-einstein condensation and liquid helium. *Phys. Rev.*, 104:576–584, Nov 1956.
- [22] Sen Yang, A. T. Hammack, M. M. Fogler, L. V. Butov, and A. C. Gossard. Coherence length of cold exciton gases in coupled quantum wells. *Phys. Rev. Lett.*, 97:187402, Oct 2006.
- [23] E.P. Gross. Structure of a quantized vortex in boson systems. *Il Nuovo Cimento Series 10*, 20(3):454–477, 1961.
- [24] L. P. Pitaevskii. Vortex lines in an imperfect bose gas. *Soviet Physics JETP-USSR*, 13(2), 1961.
- [25] Alexey Kavokin, Guillaume Malpuech, and Mikhail Glazov. Optical spin hall effect. *Phys. Rev. Lett.*, 95:136601, Sep 2005.
- [26] C. Leyder, M. Romanelli, J. Ph. Karr, E. Giacobino, T. C. H. Liew, M. M. Glazov, A. V. Kavokin, G. Malpuech, and A. Bramati. Observation of the optical spin hall effect. *Nat Phys*, 3(9):628–631, sep 2007.
- [27] P. G. Savvidis, J. J. Baumberg, R. M. Stevenson, M. S. Skolnick, D. M. Whittaker, and J. S. Roberts. Angle-resonant stimulated polariton amplifier. *Phys. Rev. Lett.*, 84:1547–1550, Feb 2000.

- [28] Peter Cristofolini, Gabriel Christmann, Simeon I. Tsintzos, George Deligeorgis, George Konstantinidis, Zacharias Hatzopoulos, Pavlos G. Savvidis, and Jeremy J. Baumberg. Coupling quantum tunneling with cavity photons. *Science*, 336(6082):704–707, 2012.
- [29] A. V. Nalitov, D. D. Solnyshkov, N. A. Gippius, and G. Malpuech. Voltage control of the spin-dependent interaction constants of dipolaritons and its application to optical parametric oscillators. *Phys. Rev. B*, 90:235304, Dec 2014.
- [30] O. Kyriienko, E. B. Magnusson, and I. A. Shelykh. Spin dynamics of cold exciton condensates. *Phys. Rev. B*, 86:115324, Sep 2012.
- [31] D. A. B. Miller, D. S. Chemla, T. C. Damen, A. C. Gossard, W. Wiegmann, T. H. Wood, and C. A. Burrus. Band-edge electroabsorption in quantum well structures: The quantum-confined stark effect. *Phys. Rev. Lett.*, 53:2173–2176, Nov 1984.
- [32] J. R. Leonard, M. Remeika, M. K. Chu, Y. Y. Kuznetsova, A. A. High, L. V. Butov, J. Wilkes, M. Hanson, and A. C. Gossard. Transport of indirect excitons in a potential energy gradient. *Applied Physics Letters*, 100(23):–, 2012.
- [33] A. A. High, A. T. Hammack, J. R. Leonard, Sen Yang, L. V. Butov, T. Ostatnický, M. Vladimirova, A. V. Kavokin, T. C. H. Liew, K. L. Campman, and A. C. Gossard. Spin currents in a coherent exciton gas. *Phys. Rev. Lett.*, 110:246403, Jun 2013.
- [34] Mikhail I. Dyakonov, editor. *Spin Physics in Semiconductors*. Springer, 2008.
- [35] Monique Combescot, Roland Combescot, Mathieu Alloing, and Francois Dubin. Optical signatures of a fully dark exciton condensate. *EPL (Europhysics Letters)*, 105(4):47011, 2014.
- [36] S. Schmitt-Rink, D. S. Chemla, and D. A. B. Miller. *Advances in Physics*, 38:89, 1989.
- [37] M. Poggio, G. M. Steeves, R. C. Myers, N. P. Stern, A. C. Gossard, and D. D. Awschalom. Spin transfer and coherence in coupled quantum wells. *Phys. Rev. B*, 70:121305, Sep 2004.
- [38] J. R. Leonard, Y. Y. Kuznetsova, Sen Yang, L. V. Butov, T. Ostatnick, A. Kavokin, and A. C. Gossard. Spin transport of excitons. *Nano Letters*, 9(12):4204–4208, 2009. PMID: 19780583.
- [39] M. Z. Maialle, E. A. de Andrada e Silva, and L. J. Sham. Exciton spin dynamics in quantum wells. *Phys. Rev. B*, 47:15776–15788, Jun 1993.
- [40] J. Feldmann, G. Peter, E. O. Göbel, P. Dawson, K. Moore, C. Foxon, and R. J. Elliott. Linewidth dependence of radiative exciton lifetimes in quantum wells. *Phys. Rev. Lett.*, 59:2337–2340, Nov 1987.
- [41] Eiichi Hanamura. Rapid radiative decay and enhanced optical nonlinearity of excitons in a quantum well. *Phys. Rev. B*, 38:1228–1234, Jul 1988.

- [42] A. T. Hammack, L. V. Butov, L. Mouchliadis, A. L. Ivanov, and A. C. Gossard. Kinetics of indirect excitons in an optically induced trap in GaAs quantum wells. *Phys. Rev. B*, 76:193308, Nov 2007.
- [43] A. B. Dzyubenko and A. L. Yablonskii. Intrawell and interwell magnetoexcitons in $\text{In}_x\text{Ga}_{1-x}\text{As}/\text{GaAs}$ coupled double quantum wells. *Phys. Rev. B*, 53:16355–16364, Jun 1996.
- [44] F. Tassone, F. Bassani, and L. C. Andreani. Quantum-well reflectivity and exciton-polariton dispersion. *Phys. Rev. B*, 45:6023–6030, Mar 1992.
- [45] A. V. Nalitov, M. Vladimirova, A. V. Kavokin, L. V. Butov, and N. A. Gippius. Nonlinear optical probe of indirect excitons. *Phys. Rev. B*, 89:155309, Apr 2014.
- [46] L. V. Butov, V. D. Kulakovskii, and A. Forchel. Spin-splitting renormalization in the neutral dense magnetoplasma in $\text{In}_x\text{Ga}_{1-x}\text{As}/\text{InP}$ quantum wells. *Phys. Rev. B*, 48:17933–17937, Dec 1993.
- [47] M.M. Glazov. Coherent spin dynamics of electrons and excitons in nanostructures (a review). *Physics of the Solid State*, 54(1):1–27, 2012.
- [48] H. Hoffmann, G. V. Astakhov, T. Kiessling, W. Ossau, G. Karczewski, T. Wojtowicz, J. Kossut, and L. W. Molenkamp. Optical spin pumping of modulation-doped electrons probed by a two-color Kerr rotation technique. *Phys. Rev. B*, 74:073407, Aug 2006.
- [49] C. Ciuti, V. Savona, C. Piermarocchi, A. Quattropani, and P. Schwendimann. Role of the exchange of carriers in elastic exciton-exciton scattering in quantum wells. *Phys. Rev. B*, 58:7926–7933, Sep 1998.
- [50] S. Ben-Tabou de Leon and B. Laikhtman. Exciton-exciton interactions in quantum wells: Optical properties and energy and spin relaxation. *Phys. Rev. B*, 63:125306, Mar 2001.
- [51] N. A. Gippius, A. L. Yablonskii, A. B. Dzyubenko, S. G. Tikhodeev, L. V. Kulik, V. D. Kulakovskii, and A. Forchel. Excitons in near-surface quantum wells in magnetic fields: Experiment and theory. *Journal of Applied Physics*, 83(10):5410–5417, 1998.
- [52] P. Andreakou, S. Cronenberger, D. Scalbert, A. Nalitov, N. A. Gippius, A. V. Kavokin, M. Nawrocki, J. R. Leonard, L. V. Butov, K. L. Campman, A. C. Gossard, and M. Vladimirova. Nonlinear optical spectroscopy of indirect excitons in coupled quantum wells. *Phys. Rev. B*, 91:125437, Mar 2015.
- [53] L. V. Fokina, I. A. Yugova, D. R. Yakovlev, M. M. Glazov, I. A. Akimov, A. Greilich, D. Reuter, A. D. Wieck, and M. Bayer. Spin dynamics of electrons and holes in $\text{InGaAs}/\text{GaAs}$ quantum wells at millikelvin temperatures. *Phys. Rev. B*, 81:195304, May 2010.

- [54] Lucio Claudio Andreani, Giovanna Panzarini, Alexey V. Kavokin, and Maria R. Vladimirova. Effect of inhomogeneous broadening on optical properties of excitons in quantum wells. *Phys. Rev. B*, 57:4670–4680, Feb 1998.
- [55] M. I. Dyakonov and V.I. Perel'. Spin relaxation of conduction electrons in noncentrosymmetric semiconductors. *Sov. Phys. Solid State*, 13(3023), 1972.
- [56] M. Dyakonov, X. Marie, T. Amand, P. Le Jeune, D. Robart, M. Brousseau, and J. Barrau. Coherent spin dynamics of excitons in quantum wells. *Phys. Rev. B*, 56:10412–10422, Oct 1997.
- [57] I. V. Mashkov, C. Gourdon, P. Lavallard, and D. Yu Roditchev. Exciton quantum beats in type-ii gaas/alas superlattices in longitudinal and in-plane magnetic fields. *Phys. Rev. B*, 55:13761–13770, May 1997.
- [58] D. S. Smirnov and M. M. Glazov. Exciton spin noise in quantum wells. *Phys. Rev. B*, 90:085303, Aug 2014.
- [59] A. Brunetti, M. Vladimirova, D. Scalbert, M. Nawrocki, A. V. Kavokin, I. A. Shelykh, and J. Bloch. Observation of spin beats at the rabi frequency in microcavities. *Phys. Rev. B*, 74:241101, Dec 2006.
- [60] G. Aichmayr, M. Jetter, L. Viña, J. Dickerson, F. Camino, and E. E. Mendez. Electric-field tuning of spin-dependent exciton-exciton interactions in coupled quantum wells. *Phys. Rev. Lett.*, 83:2433–2436, Sep 1999.
- [61] A. V. Kavokin, M. Vladimirova, B. Jouault, T. C. H. Liew, J. R. Leonard, and L. V. Butov. Ballistic spin transport in exciton gases. *Phys. Rev. B*, 88:195309, Nov 2013.
- [62] A. Alexandrou, J. A. Kash, E. E. Mendez, M. Zachau, J. M. Hong, T. Fukuzawa, and Y. Hase. Electric-field effects on exciton lifetimes in symmetric coupled gaas/al_{0.3}ga_{0.7}as double quantum wells. *Phys. Rev. B*, 42:9225–9228, Nov 1990.
- [63] L. V. Butov, A. Imamoglu, A. V. Mintsev, K. L. Campman, and A. C. Gossard. Photoluminescence kinetics of indirect excitons in gaas/al_xga_{1-x}As coupled quantum wells. *Phys. Rev. B*, 59:1625–1628, Jan 1999.
- [64] L. V. Butov, A. L. Ivanov, A. Imamoglu, P. B. Littlewood, A. A. Shashkin, V. T. Dolgopолоv, K. L. Campman, and A. C. Gossard. Stimulated scattering of indirect excitons in coupled quantum wells: Signature of a degenerate bose-gas of excitons. *Phys. Rev. Lett.*, 86:5608–5611, Jun 2001.
- [65] H. Flayac, D. D. Solnyshkov, I. A. Shelykh, and G. Malpuech. Transmutation of skyrmions to half-solitons driven by the nonlinear optical spin hall effect. *Phys. Rev. Lett.*, 110:016404, Jan 2013.
- [66] D. V. Vishnevsky, H. Flayac, A. V. Nalitov, D. D. Solnyshkov, N. A. Gippius, and G. Malpuech. Skyrmion formation and optical spin-hall effect in an expanding coherent cloud of indirect excitons. *Phys. Rev. Lett.*, 110:246404, Jun 2013.

- [67] Masaru Onoda, Shuichi Murakami, and Naoto Nagaosa. Hall effect of light. *Phys. Rev. Lett.*, 93:083901, Aug 2004.
- [68] K. G. Lagoudakis, M. Wouters, M. Richard, A. Baas, I. Carusotto, R. Andre, Le Si Dang, and B. Deveaud-Pledran. Quantized vortices in an exciton-polariton condensate. *Nat Phys*, 4(9):706–710, September 2008.
- [69] R. Hivet, H. Flayac, D. D. Solnyshkov, D. Tanese, T. Boulier, D. Andreoli, E. Giacobino, J. Bloch, A. Bramati, G. Malpuech, and A. Amo. Half-solitons in a polariton quantum fluid behave like magnetic monopoles. *Nat Phys*, 8(10):724–728, October 2012.
- [70] D. N. Krizhanovskii, D. Sanvitto, I. A. Shelykh, M. M. Glazov, G. Malpuech, D. D. Solnyshkov, A. Kavokin, S. Ceccarelli, M. S. Skolnick, and J. S. Roberts. Rotation of the plane of polarization of light in a semiconductor microcavity. *Phys. Rev. B*, 73:073303, Feb 2006.
- [71] K.V. Kavokin, P. Renucci, T. Amand, X. Marie, P. Senellart, J. Bloch, and B. Sermage. Linear polarisation inversion: A signature of coulomb scattering of cavity polaritons with opposite spins. *physica status solidi (c)*, 2(2):763–767, 2005.
- [72] P. Renucci, T. Amand, X. Marie, P. Senellart, J. Bloch, B. Sermage, and K. V. Kavokin. Microcavity polariton spin quantum beats without a magnetic field: A manifestation of coulomb exchange in dense and polarized polariton systems. *Phys. Rev. B*, 72:075317, Aug 2005.
- [73] J. Cuadra, D. Sarkar, L. Viña, J. M. Hvam, A. Nalitov, D. Solnyshkov, and G. Malpuech. Polarized emission in polariton condensates: Switching in a one-dimensional natural trap versus inversion in two dimensions. *Phys. Rev. B*, 88:235312, Dec 2013.
- [74] M. M. Glazov, H. Ouerdane, L. Pilozzi, G. Malpuech, A. V. Kavokin, and A. D’Andrea. Polariton-polariton scattering in microcavities: A microscopic theory. *Phys. Rev. B*, 80:155306, Oct 2009.
- [75] M. M. Glazov, I. A. Shelykh, G. Malpuech, K. V. Kavokin, A. V. Kavokin, and D. D. Solnyshkov. Anisotropic polariton scattering and spin dynamics of cavity polaritons. *Solid State Communications*, 134:137–200, 2005.
- [76] Giovanna Panzarini, Lucio Claudio Andreani, A. Armitage, D. Baxter, M. S. Skolnick, V. N. Astratov, J. S. Roberts, Alexey V. Kavokin, Maria R. Vladimirova, and M. A. Kaliteevski. Exciton-light coupling in single and coupled semiconductor microcavities: Polariton dispersion and polarization splitting. *Phys. Rev. B*, 59:5082–5089, Feb 1999.
- [77] I. Shelykh, G. Malpuech, K. V. Kavokin, A. V. Kavokin, and P. Bigenwald. Spin dynamics of interacting exciton polaritons in microcavities. *Phys. Rev. B*, 70:115301, Sep 2004.

- [78] Huy Thien Cao, T. D. Doan, D. B. Tran Thoai, and H. Haug. Polarization kinetics of semiconductor microcavities investigated with a boltzman approach. *Phys. Rev. B*, 77:075320, Feb 2008.
- [79] M. Vladimirova, S. Cronenberger, D. Scalbert, K. V. Kavokin, A. Miard, A. Lemaître, J. Bloch, D. Solnyshkov, G. Malpuech, and A. V. Kavokin. Polariton-polariton interaction constants in microcavities. *Phys. Rev. B*, 82:075301, Aug 2010.
- [80] Christopher Coulson, Gabriel Christmann, Peter Cristofolini, Cornelius Grossmann, Jeremy J. Baumberg, Simeon I. Tsintzos, George Konstantinidis, Zacharias Hatzopoulos, and Pavlos G. Savvidis. Electrically controlled strong coupling and polariton bistability in double quantum wells. *Phys. Rev. B*, 87:045311, Jan 2013.
- [81] E. Hanamura and H. Haug. Condensation effects of excitons. *Physics Reports*, 33, 1977.
- [82] G. Rochat, C. Ciuti, V. Savona, C. Piermarocchi, A. Quattropani, and P. Schwendimann. Excitonic bloch equations for a two-dimensional system of interacting excitons. *Phys. Rev. B*, 61:13856–13862, May 2000.
- [83] C Ciuti, P Schwendimann, and A Quattropani. Theory of polariton parametric interactions in semiconductor microcavities. *Semiconductor Science and Technology*, 18(10):S279, 2003.
- [84] O. Kyriienko, E. B. Magnusson, and I. A. Shelykh. Spin dynamics of cold exciton condensates. *Phys. Rev. B*, 86:115324, Sep 2012.
- [85] L. D. Landau and E. M. Lifshitz. *Quantum Mechanics: NonRelativistic Theory*, volume 3. Butterworth-Heinemann, Oxford, 1977.
- [86] N. Takemura, S. Trebaol, M. Wouters, M. T. Portella-Oberli, and B. Deveaud. Polaritonic feshbach resonance. *Nat Phys*, 10(7):500–504, jul 2014.
- [87] T. Jacqmin, I. Carusotto, I. Sagnes, M. Abbarchi, D. Solnyshkov, D., G. Malpuech, E. Galopin, A. Lemaitre, J. Bloch, and A. Amo. Direct observation of dirac cones and a flatband in a honeycomb lattice for polaritons. *Phys. Rev. Lett.*, 112:116402, Mar 2014.
- [88] G. Sala, V. D. Solnyshkov, D. I. Carusotto, T. Jacqmin, A. Lemaitre, H. Terças, A. Nalitov, M. Abbarchi, E. Galopin, I. Sagnes, J. Bloch, G. Malpuech, and A. Amo. Spin-orbit coupling for photons and polaritons in microstructures. *Phys. Rev. X*, 5:011034, Mar 2015.
- [89] Marta Galbiati, Lydie Ferrier, Dmitry D. Solnyshkov, Dimitrii Tanese, Esther Wertz, Alberto Amo, Marco Abbarchi, Pascale Senellart, Isabelle Sagnes, Aristide Lemaitre, Elisabeth Galopin, Guillaume Malpuech, and Jacqueline Bloch. Polariton condensation in photonic molecules. *Phys. Rev. Lett.*, 108:126403, Mar 2012.

- [90] V. Nalitov, A. G. Malpuech, H. Terças, and D. Solnyshkov, D. Spin-orbit coupling and the optical spin hall effect in photonic graphene. *Phys. Rev. Lett.*, 114:026803, Jan 2015.
- [91] Edward McCann and Vladimir I. Fal'ko. Landau-level degeneracy and quantum hall effect in a graphite bilayer. *Phys. Rev. Lett.*, 96:086805, Mar 2006.
- [92] P. Rakyta, A. Kormányos, and J. Cserti. Trigonal warping and anisotropic band splitting in monolayer graphene due to rashba spin-orbit coupling. *Phys. Rev. B*, 82:113405, Sep 2010.
- [93] C. L. Kane and E. J. Mele. Quantum spin hall effect in graphene. *Phys. Rev. Lett.*, 95:226801, Nov 2005.
- [94] P. R. Wallace. The band theory of graphite. *Phys. Rev.*, 71:622–634, May 1947.
- [95] C. L. Kane and E. J. Mele. Z₂ topological order and the quantum spin hall effect. *Phys. Rev. Lett.*, 95:146802, Sep 2005.
- [96] I A Shelykh, A V Kavokin, Yuri G Rubo, T C H Liew, and G Malpuech. Polariton polarization-sensitive phenomena in planar semiconductor microcavities. *Semiconductor Science and Technology*, 25(1):013001, 2010.
- [97] H. Flayac, D. D. Solnyshkov, I. A. Shelykh, and G. Malpuech. Transmutation of skyrmions to half-solitons driven by the nonlinear optical spin hall effect. *Phys. Rev. Lett.*, 110:016404, Jan 2013.
- [98] H. Terças, H. Flayac, D. Solnyshkov, D., and G. Malpuech. Non-abelian gauge fields in photonic cavities and photonic superfluids. *Phys. Rev. Lett.*, 112:066402, Feb 2014.
- [99] Mikael C. Rechtsman, Julia M. Zeuner, Yonatan Plotnik, Yaakov Lumer, Daniel Podolsky, Felix Dreisow, Stefan Nolte, Mordechai Segev, and Alexander Szameit. Photonic floquet topological insulators. *Nature*, 496(7444):196–200, apr 2013.
- [100] F. D. M. Haldane and S. Raghu. Possible realization of directional optical waveguides in photonic crystals with broken time-reversal symmetry. *Phys. Rev. Lett.*, 100:013904, Jan 2008.
- [101] Zheng Wang, Yidong Chong, J. D. Joannopoulos, and Marin Soljacic. Observation of unidirectional backscattering-immune topological electromagnetic states. *Nature*, 461(7265):772–775, oct 2009.
- [102] T. Karzig, C.-E. Bardyn, N. Lindner, and G. Refael. Topological polaritons from quantum wells in photonic waveguides or microcavities. *arXiv:1406.4156*, 2014.
- [103] V. Nalitov, A. D. Solnyshkov, D. and G. Malpuech. Polariton \mathbb{Z} topological insulator. *Phys. Rev. Lett.*, 114:116401, Mar 2015.
- [104] Iacopo Carusotto and Cristiano Ciuti. Quantum fluids of light. *Rev. Mod. Phys.*, 85:299–366, Feb 2013.

- [105] Yaakov Lumer, Yonatan Plotnik, Mikael C. Rechtsman, and Mordechai Segev. Self-localized states in photonic topological insulators. *Phys. Rev. Lett.*, 111:243905, Dec 2013.
- [106] K. v. Klitzing, G. Dorda, and M. Pepper. New method for high-accuracy determination of the fine-structure constant based on quantized hall resistance. *Phys. Rev. Lett.*, 45:494–497, Aug 1980.
- [107] D. J. Thouless, M. Kohmoto, M. P. Nightingale, and M. den Nijs. Quantized hall conductance in a two-dimensional periodic potential. *Phys. Rev. Lett.*, 49:405–408, Aug 1982.
- [108] Barry Simon. Holonomy, the quantum adiabatic theorem, and berry’s phase. *Phys. Rev. Lett.*, 51:2167–2170, Dec 1983.
- [109] M. Z. Hasan and C. L. Kane. Colloquium: Topological insulators. *Rev. Mod. Phys.*, 82:3045–3067, Nov 2010.
- [110] K. S. Novoselov, Z. Jiang, Y. Zhang, S. V. Morozov, H. L. Stormer, U. Zeitler, J. C. Maan, G. S. Boebinger, P. Kim, and A. K. Geim. Room-temperature quantum hall effect in graphene. *Science*, 315(5817):1379, 2007.
- [111] F. D. M. Haldane. Model for a quantum hall effect without landau levels: Condensed-matter realization of the ”parity anomaly”. *Phys. Rev. Lett.*, 61:2015–2018, Oct 1988.
- [112] Markus Konig, Steffen Wiedmann, Christoph Brne, Andreas Roth, Hartmut Buhmann, Laurens W. Molenkamp, Xiao-Liang Qi, and Shou-Cheng Zhang. Quantum spin hall insulator state in hgte quantum wells. *Science*, 318(5851):766–770, 2007.
- [113] D. Hsieh, D. Qian, L. Wray, Y. Xia, Y. S. Hor, R. J. Cava, and M. Z. Hasan. A topological dirac insulator in a quantum spin hall phase. *Nature*, 452(7190):970–974, apr 2008.
- [114] Netanel H. Lindner, Gil Refael, and Victor Galitski. Floquet topological insulator in semiconductor quantum wells. *Nat Phys*, 7(6):490–495, jun 2011.
- [115] Zheng Wang, Y. D. Chong, John D. Joannopoulos, and Marin Soljačić. Reflection-free one-way edge modes in a gyromagnetic photonic crystal. *Phys. Rev. Lett.*, 100:013905, Jan 2008.
- [116] R. O. Umucal ilar and I. Carusotto. Fractional quantum hall states of photons in an array of dissipative coupled cavities. *Phys. Rev. Lett.*, 108:206809, May 2012.
- [117] Mohammad Hafezi, Eugene A. Demler, Mikhail D. Lukin, and Jacob M. Taylor. Robust optical delay lines with topological protection. *Nat Phys*, 7(11):907–912, nov 2011.
- [118] Alexander B. Khanikaev, S. Hossein Mousavi, Wang-Kong Tse, Mehdi Kargarian, Allan H. MacDonald, and Gennady Shvets. Photonic topological insulators. *Nat Mater*, 12(3):233–239, mar 2013.

- [119] Wen-Jie Chen, Shao-Ji Jiang, Xiao-Dong Chen, Jian-Wen Dong, and C. T. Chan. Experimental realization of photonic topological insulator in a uniaxial metacrystal waveguide. *arXiv:1401.0367*, 2014.
- [120] Tomoki Ozawa and Iacopo Carusotto. Anomalous and quantum hall effects in lossy photonic lattices. *Phys. Rev. Lett.*, 112:133902, Apr 2014.
- [121] Edward McCann and Mikito Koshino. The electronic properties of bilayer graphene. *Reports on Progress in Physics*, 76(5):056503, 2013.
- [122] G. Dasbach, C. Diederichs, J. Tignon, C. Ciuti, Ph. Roussignol, C. Delalande, M. Bayer, and A. Forchel. Polarization inversion via parametric scattering in quasi-one-dimensional microcavities. *Phys. Rev. B*, 71:161308, Apr 2005.
- [123] J. Fischer, S. Brodbeck, A. V. Chernenko, I. Lederer, A. Rahimi-Iman, M. Amthor, V. D. Kulakovskii, L. Worschech, M. Kamp, M. Durnev, C. Schneider, A. V. Kavokin, and S. Höfling. Anomalies of a nonequilibrium spinor polariton condensate in a magnetic field. *Phys. Rev. Lett.*, 112:093902, Mar 2014.
- [124] C. Sturm, D. Solnyshkov, O. Krebs, A. Lemaitre, I. Sagnes, E. Galopin, A. Amo, G. Malpuech, and J. Bloch. Driven-dissipative confined polariton condensate under magnetic field. *arXiv:1409.5112*, 2014.